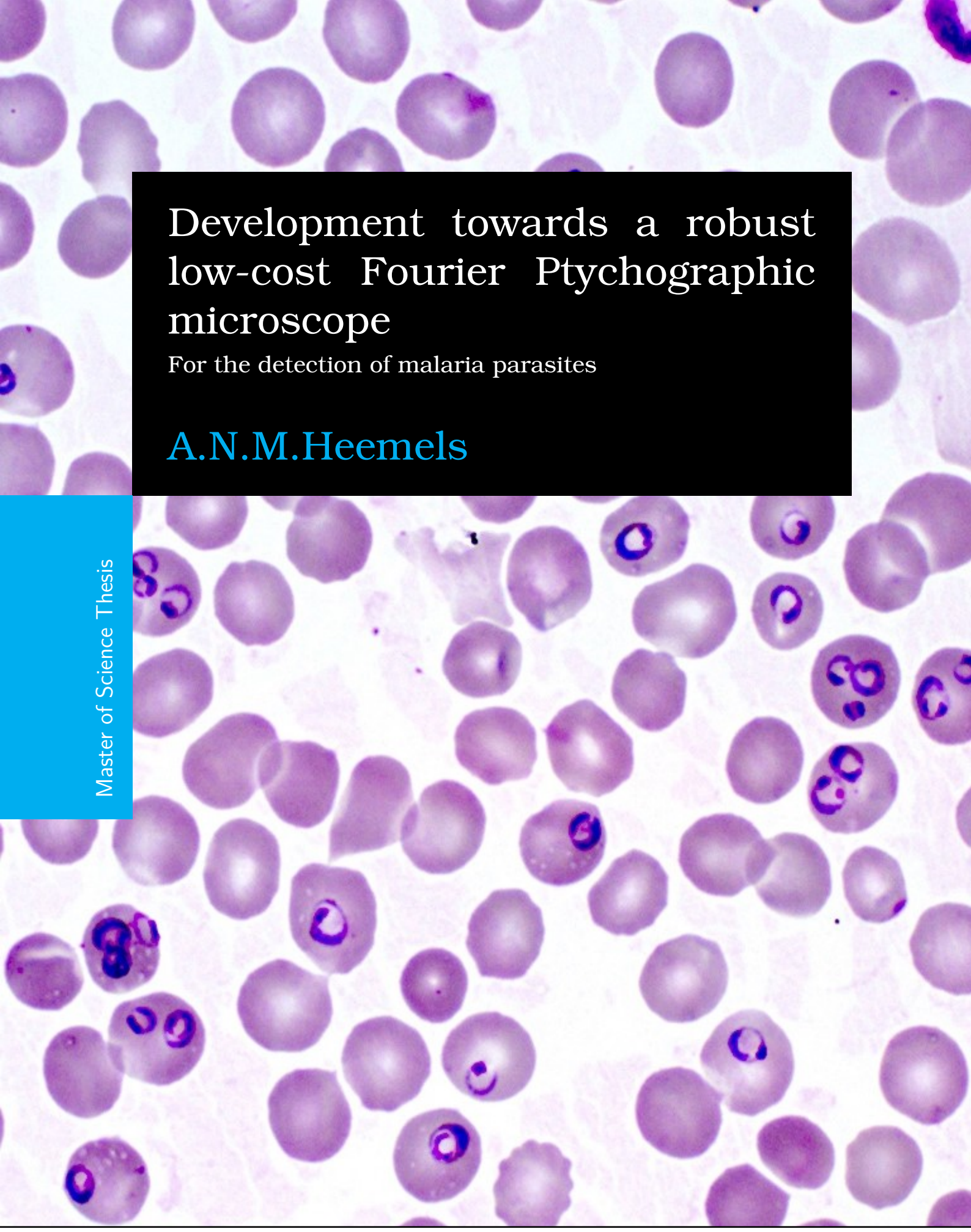

Development towards a robust low-cost Fourier Ptychographic microscope

For the detection of malaria parasites

A.N.M.Heemels

Master of Science Thesis

TU Delft Delft University of Technology

Delft Center for Systems and Control

Development towards a robust low-cost Fourier Ptychographic microscope

For the detection of malaria parasites

Master of Science Thesis

For the degree of Master of Science in Systems and Control at Delft University of Technology

A.N.M.Heemels

August 20, 2019

Faculty of Mechanical, Maritime and Materials Engineering (3mE) · Delft University of Technology

Copyright © Delft Center for Systems and Control (DCSC)
All rights reserved.

Abstract

This thesis discusses developments towards a low-cost Fourier Ptychographic microscope for label free imaging of malaria parasites.
A review of the morphology and life cycle of malaria and the main diagnostic methods for its detection is followed by an introduction to Fourier Ptychography with emphasis on the underlying imaging principles and phase retrieval algorithms which are at the core of the algorithms used.
The practical realization of the Fourier Ptychographic setup with the required resolution has proven to be very challenging due to its susceptibility to errors when operating the system at its theoretical limits.
Insights from in-depth analyses of the effects of quantization noise, intensity drop-off due to angled illumination, and partial coherence are presented. These insights rule in- or out these potential error sources and help identify potential mitigations in the design.
In the final chapters the realization of the setup is described, and the results with real blood smear samples are used to illustrate the interference of the error sources. The thesis concludes with considerations for further research and recommendations for international collaboration.

Table of Contents

List of Figures

List of Tables

"In theory there is no difference between theory and practice.
In practice there is."

— *Albert Einstein*

Chapter 1

Introduction

Malaria is a mosquito borne disease caused by a parasite of the genus plasmodium. An estimated 219 million cases occurred in 2017 causing over 403500 deaths [2]. In areas with high infection rates, over-diagnosis is common as malaria does not exhibit unique symptoms compared to other tropical diseases, rendering clinical diagnosis unreliable[3]. Therefore diagnostic methods such as microscopic peripheral blood smear analysis with Giemsa stained blood samples and Rapid Diagnostic Tests (RDTs) are required to reliably detect parasitic presence. Both methods have their advantages and drawbacks, RDTs for one is the most used technique as it's easy to use but may provide misleading results as cured malaria cases can still be tested positive and low parasitic density may not be detected [4]. In addition it is unable to determine specie and density, requiring its results to be verified by an alternative method [5]. Microscopy has a higher specificity and allows for parasitic specie and density determination, but requires specialized lab equipment and highly trained personnel which are expensive to train and must follow labor intensive protocols [1]. By alleviating this workload and reducing the amount of specialization required for quality diagnosis and making the technology more available, microscopy would be able keep up with the use of RDTs and improve overall malaria diagnosis quality. This may be achieved by increasing the microscopes area of observation (field of view) while retaining the resolution and simplifying the protocol by removing the need for staining.

However, simply increasing the microscopes field of view while keeping the same resolution is impossible for lens based microscopes as they are limited by their space band product (SBP) [6]. Increasing a microscopes SBP is possible but often requires advanced and expensive setups which limit the availability of the technology. One method which does seem promising is Fourier Ptychography [7], which is based on developments in synthetic aperture techniques [8] and phase retrieval algorithms [9, 10] and enables increasing the microscopes SBP by using computational techniques. In addition, Fourier Ptychography provides the sample's phase information, which would theoretically allow the detection of parasites without having to stain the blood sample.

This makes a Fourier Ptychography based microscope very interesting for different groups with varying levels of diagnostic/medical experience and accessible facilities. Earlier research on the acceptance of a smart-phone based microscope [11] with Nigerian medicine vendors, pharmacists, doctors, lab scientists and volunteer health workers [12], provided an extensive overview of what these varying groups of people are looking for in such a device and their reason to use or not to use such a product. Most stakeholders were concerned with the tests being time consuming, the device being too expensive and performing lab steps such as staining the sample and having to image it. Also, all stakeholders were in favor of automated diagnosis, but the more medically trained want the ability to cross-check. A requirement which was especially important for the volunteer health workers is that the device should be robust enough to survive rough transport and humid climate conditions. This multitude of requirements make the design of a Fourier Ptychographic microscope very challenging.

Nevertheless, these requirements should be taken into consideration in the design of the microscope by including appropriate tolerances and robustness criteria such that reconstruction of the objects can be guaranteed. However, little is known about the effects of model, setup mismatches and the accompanying sensitivity of the Fourier Ptychographic system. With partial coherence and quantization noise and intensity drop-off being factors which will be prominent factors in the design of an low-cost system it is of interest to obtain a better understanding of these effects and how they affects the Fourier Ptychographic reconstruction results. Which will help in the development of a such systems.

Chapter 2

Malaria

chapter:malaria) Malaria parasites are hard to detect as they are small, have complex life-cycles and require special methods to even be visualized. In addition, 5 different species are known to infect humans, of which Plasmodium Falciparum (P.Falciparum) is the most lethal. Different species each require a unique treatment, making specie determination a vital part of the diagnosis process. RDTs are limited on this aspect as most test on P.Falciparum presence and also are not reliable in early stages of infection. Therefore, microscopic methods are required to ensure accurate diagnosis. this chapter will provide an overview of the important parts of the parasitic life-cycle and morphological traits which may facilitate optical detection and facilitation, followed by the main diagnostics and alternative optical methods in malaria detection.

2-1 Plasmodium

The parasite responsible for malaria is of the genus plasmodium. It has a 2-stage life cycle, one of which takes place in the mosquito and one in the human host. There are 5 species which are known to infect humans: Plasmodium Falciparum, Plasmodium Vivax, Plasmodium Malariae, Plasmodium Ovale and Plasmodium Knowlesi.

2-1-1 Lifecycle

The human life-cycle of the plasmodium parasite fig. 2-1, starts when a female Anopheles mosquito stings for a blood meal, injecting the parasite's first development stage, sporozoites in to the bloodstream. These quickly make their way to the liver where they form a parasitic vacuole membrane (PVM) and, undergo asexual reproduction or schizogony. Once the PVM has reached the stage of a full-grown liver schizont it releases thousands of merozoites into the blood stream which infect erythrocytes and enter the first blood stage known as the ring stage. During this stage the merozoites either undergo schizogony or gametocytogenesis. During schizogony, the amount of plasma increases and the merozoites eventually enters

the ring stage becoming a trophozoite. The parasite subsequently develops into a schizont, which when fully grown erupts, again releasing merozoites into the blood stream. When undergoing gametocytogenesis, the parasite grows into a gametocyte which is the first stage of the mosquito host cycle [13, 14].

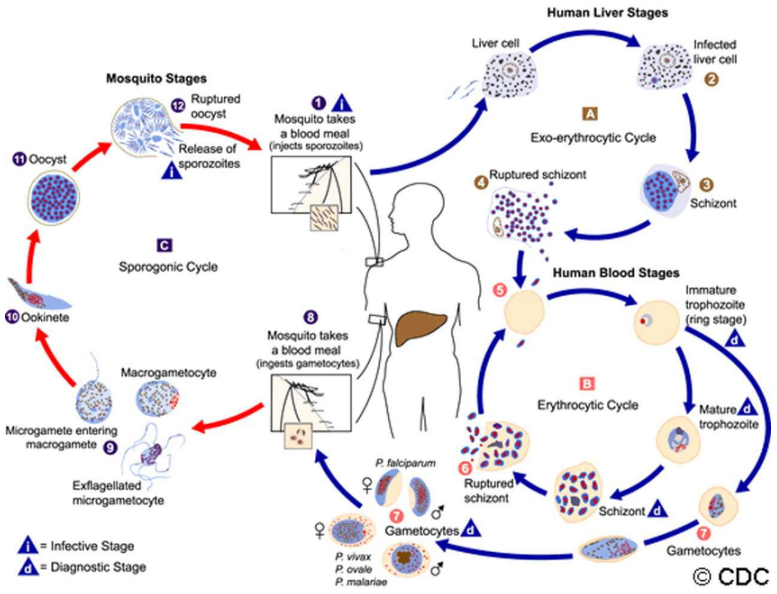

Figure 2-1: Visualization of the malaria lifecycle, Source:https://www.cdc.gov/dpdx/

2-1-2 Morphology

Merozoites are the earliest form of the parasite which can be detected in the blood and they are $1\mu m$ in size and oval shaped. When it invades an erythrocyte and enters the ring stage, it consists of a nucleus with a red chromatin dot and a food vacuole surrounded by cytoplasm (fig. 2-2).

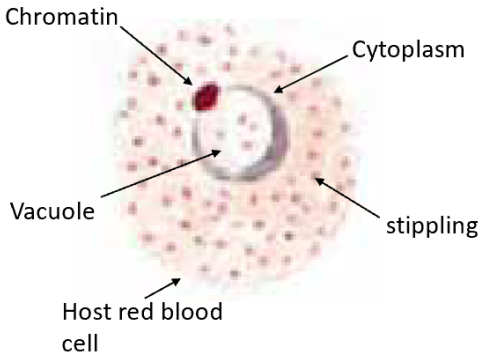

Figure 2-2: Different morphological traits of an erythrocyte infected with the malaria parasite

Table 2-1: Table with different morphological traits of human infecting malaria species and their stages

Stage Parasite	P. falciparum	P. vivax	P. ovale	P. malariae	P. knowlesi
Infected erythrocyte	Normal size, Maurer dots	Enlarged, Schuffener dots	Enlarged, oval and fimbriated	Normal or microcytic, stippling usually not seen	Normal size with single of double chromatin dot with dense cytoplasm
Early trophozoites	Two or more rings with chromatin dot	Single ring with large chromatin dot	Thick compact rings	small, compact ring	Single or double chromatin with dens cytoplasm
Later Trophozoites	sometimes 2 chromatin dots, vacuolated, dark pigment	Amoeboid, central vacuole, light blue cytoplasm, yellowish-brown pigment	Smaller than P. vivax, slightly amoeboid, dark-brown pigment	Band form across cell, large chromatin, deep blue cytoplasm, dark-brown pigment	Cytoplasm slightly amoeboid and irregular, varying pigmentation
Schizonts	8-24 merozoites filling 2/3 of cell	12-24 irregular arranged	8-12 merozoites filling 2/3 of cell	6-12 merozoites in daisy formation	Up to 16 merozoites with grape like structure
Gametocytes	Banana shaped, diffuse chromatin, single nucleus	Oval shaped which almost fills whole erythrocyte, single nucleus	oval shaped, fills 3/4 of host cell, similar to P. vivax but smaller	round, fills host from 1/2 - 3/4, similar to P. vivax but smaller	Round, fills whole host

During this stage, the food vacuole size and the amount of the malarial pigment hemozoin increase as hemoglobin is digested [15]. Hemozoin alters the host's color depending on the type of infecting Plasmodium species [16]. During later stages, the host erythrocyte can become enlarged, with deformations along its edges accompanied by pigment dots. The combination of these morphological changes is used to determine the species in the ring stage. For example, the combination of enlarged cells, distorted edges and pink Schuffner dots is distinct for P.Vivax, while enlarged, round erythrocytes with mauve James dots correspond to P.Ovale [1].

Noticeable features of a Schizont are the many chromatin dots belonging to the contained merozoites. The number of merozoites together with their particular arrangement is typical for specific species.

Gametocytes of the P. Falciparum can be easily recognized by their elongated banana shape. Gametocytes of other species are predominately round and characterized by how much of the host cell they fill up [16].

An extensive overview and sketches of the morphological characteristics of the various Plasmodium species and their stages can be found in table 2-1 and table 2-2. Even trained pathologists are prone to misclassifications due to morphological similarities between species. One specie which is especially hard to detect is P.Knowlesi, its trophozoite stage resembles P.Falciparum while later stages show more resemblance with P.Malariae and therefore the specie is often confused with cross infection of P. Falciparum and P.Malariae [17, 18].

Table 2-2: Sketches of the different stages of Plasmodium Falciparum, Vivax, Malariae and Ovale. Sketches are form the "Basic Malaria Microscopy Manual, Part 1 [1]"

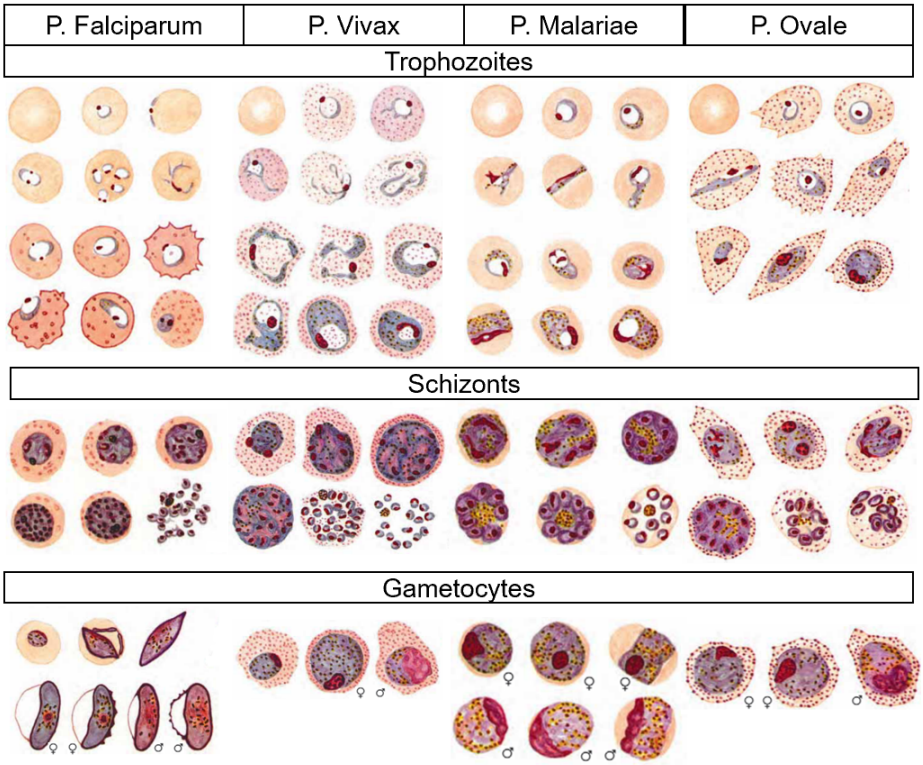

2-2 Diagnostic Methods

Clinical diagnosis of malaria based on a patients symptoms is very challenging as there is no combinations of symptoms that reliably distinguish malaria from other diseases, resulting in low specificity [3]. Therefore other diagnostic methods based on detecting parasitic presence in the patients blood which can ensure high specificity and sensitivity [1] are necessary. The most commonly used diagnostic methods are peripheral blood analysis using light microscopy and Rapid Diagnostic Tests (RDT).

2-2-1 Rapid Diagnostic Tests

RDT is the most popular diagnostic tool among health workers. In 2017 over 245 million RDTs were distributed and they covered 75% of all malaria test conducted [2]. This popularity can be attributed to RDTs being relatively inexpensive ($0.65 - $1), easy to use and only taking around 10-15 minutes to conduct [5]. They work by applying blood on a membrane containing malaria antibodies to detect specific antigens produced by malaria parasites. Most RDTs test for histadein-rich protein 2 (HRP2) or parasite-specific lactate dehydrogenase (pLDH) and are specific for P. Falciparum. There are tests which are able to detect other species, some of which in addition are able to detect cross infection[4]. However, RDT results may be misleading as false positive test results can be caused by detection of the malarial antigen while the infecting parasite is no longer present [4].
On the other hand, negative results do not always exclude parasitic presence as there may be insufficient parasites for accurate detection (100 parasites/μl required for most tests [5]), the RDT may have been affected by poor transport or storage conditions or, it was designed to detect a different specie than the one present. Recent studies have also indicated that false negatives may occur due to mutation of the parasite which does not produce the HRP2/3 protein [19]. Therefore, it is important to verify results using different diagnostic methods.

2-2-2 Light Microscopy

Peripheral blood smear analysis using light microscopy is the second most-used diagnostic technique [2]. The protocol consists of preparing both a thick- and a thin blood smear, with Giemsa staining which adds contrast between erythrocytes and parasites. First, parasite density is determined by analyzing the thick blood smear, for which 100 fields of view must be analyzed before the sample can be classified as malaria free [1]. Next, the species of the parasite is determined by analyzing the thin blood smear, which requires over 800 fields of view before the slide is diagnosed as malaria free. This process is very time-consuming, taking up to 1 hour per test, and its quality is heavily dependent on the microscopist's expertise. An average microscopist is able to detect >50 parasites/μl while experts can detect up to 5 parasite/μl [5]. In addition, there are many factors which limit the availability of microscopy as diagnostic method, such as lack of basic lab facilities, absence of training programs, poor equipment maintenance, lack of quality control and the decrease of skills due to overuse of RDT [20].

[1] *Sensitivity*: percentage of infected people who have been correctly diagnosed. $Sens = \frac{\#True\ positives}{\#positives}$
Specificity: percentage non-infected people classified as not being infected. $Spec = \frac{\#True\ negatives}{\#negatives}$

2-2-3 Other Optical Methods

As standard peripheral blood smear analysis is time-consuming, other optical methods have been developed which allow for a more efficient diagnostic process.

Fluorescence Microscopy

Fluorescence microscopy makes use of the fluorescence of the sample or of an added fluorophore. When a sample with fluorescent properties is illuminated with a specific wavelength, it will re-emit light with a shorter wavelength. This light can be filtered from the illuminating light, allowing for the visualization of specific proteins. In malaria diagnosis, quantitative buffy coat (QBC) stains the parasite's DNA using acridine orange, which increases visibility of the nucleus and cytoplasm [5]. It is compatible with both thick and thin blood smear and facilitates a much faster diagnosis because artifacts normally present in Giemsa staining are not imaged [21]. The downsides are reliance on of specialized instrumentation, poor ability to detect parasitic density, and poor species specificity [5].

Polarization Microscopy

Polarization microscopy illuminates the sample with polarized light. When objects with birefringent properties are present in the sample, these will interact with the illuminating light and create contrast between the birefringent object and the rest of the sample. The malarial pigment hemozoin has such birefringent properties, allowing for an increase in image contrast which simplifies the detection process [22, 23].

Dark field Microscopy

Dark field microscopy visualizes the light scattered by the sample and blocks the light originating from the source. Hemozoin strongly scatters light, allowing for detection of malaria without the need for staining [24]. A combination of Dark field and polarization microscopy has been proposed using hemozoins birefringent and scattering properties [15]. However, this methods does not allow for clear distinction between light scattered by hemozoin and that scattered by small particles in the sample [21].

Quantitative Phase imaging

Quantitative phase imaging techniques provide a map of optical phase shifts induced by the sample. Phase is not measured by standard imaging sensors but can be obtained by using interference of the diffracted light with a reference source (quantitative phase spectroscopy, holography) or by means of reconstruction using phase retrieval techniques with measurement diversity in either wavelength, illumination angle or defocus (Ptychography or Tomography). Quantitative phase imaging allows for unstained detection of malaria by looking for quantitative phase anomalies in erythrocytes caused by the malaria parasite [25, 26].

Chapter 3

Fourier Ptychography

Standard lens based microscopes are limited their Space Bandwidth Product (SBP) [27], defined by the product of the field of view and the range of observable frequencies (denoted by the systems Numerical aperture and diffraction limit). As the product is constant, an increase in one requires the other to decrease. Further SBP increases of a lens-based microscope can be achieved by increasing the field of view of the system by scanning the sample. Alternatively the numerical aperture can be increased using confocal scanning or nanoscopic methods such as STED, PALM and STORM [28]. One can also get around the numerical aperture limit imposed on the imaging system by employing lens-less methods such as Shadow-imaging and inline holography [29]. Furthermore, increasing the SBP can also be done computationally for example with synthetic aperture methods which use image diversity to create high resolution images corresponding to a numerical aperture larger than that of the system [7, 29, 8, 30]. Most of these methods require moving components with micrometer accuracy, which is not optimal for the envisioned operating conditions. However, Fourier Ptychography [7] is a synthetic aperture method that does not require moving components and with a robust design could be used in harsher-environments. To understand the workings of Fourier Ptychography, first its overall functioning will be discussed, followed by the theory of the underlying phase retrieval algorithms. Finally, relevant developments in Fourier Ptychography will be discussed.

3-1 Theory

The Fourier Ptychographic setup is similar to a standard light microscope, with the only difference being the light source fig. 3-1.

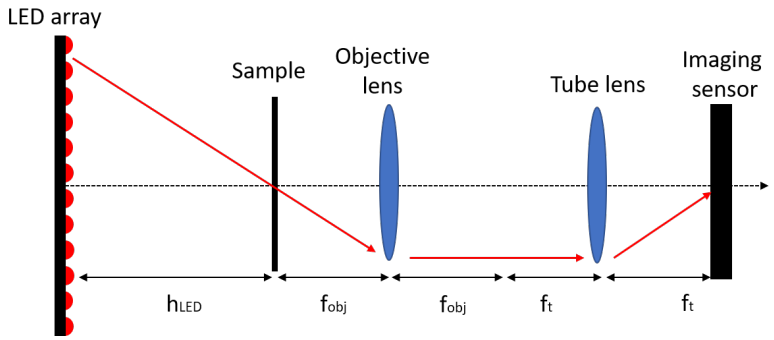

Figure 3-1: Schematic of Basic Fourier Ptychographic Setup

Fourier Ptychography makes use of an LED-array, allowing the sample to be illuminated from different angles, with each angle corresponding to a unique set of spectral information. When the sample is illuminated, the incident light is scattered in all direction, which can be visualized as a cone fig. 3-2. Large details in the sample will scatter the light close to the direction of illumination, small details will scatter the light to the edges of the cone. Under normal incident illumination, depicted in fig. 3-2a, mainly the information of the large details will be collected by the objective lens of the microscope. Under angled illumination, the orientation of the cone changes following the illumination angle fig. 3-2b. In this case, the light entering the objective corresponds to the small details of the sample. In mathematical terms: varying the illumination angle facilitates the sampling of a different area in the samples spectral (Fourier) domain, with the size of the sampling area determined by the numerical aperture (NA) of the objective lens figs. 3-2c and 3-2d. The image corresponding to the i-th LED illumination I_i can then be expressed as [31]:

$$I_i(x,y) = |\mathcal{F}^{-1}(\mathcal{O}(k_x - k_{x,i}, k_y - k_{y,i})\mathcal{P}(k_x,k_y))|^2 \tag{3-1}$$

With $\mathcal{F}$ the Fourier transform operator, $\mathcal{F}^{-1}$ the inverse operator, $\mathcal{O}(k_x,k_y)$ is the Fourier transform of the samples transmission function $O(x,y)$, $(x,y) \in \mathbb{R}^2$ coordinates in the samples spatial domain and $(k_x,k_y) \in \mathbb{R}^2$ coordinates in the samples spectral domain. The pupil function the objective lens $\mathcal{P}(k_x,k_y)$ corresponding to wave length λ is defined as:

$$\mathcal{P}(k_x,k_y) = \begin{cases} 1, & \text{if } k_x^2 + k_y^2 \leq NA_{obj}\frac{2\pi}{\lambda} \\ 0, & \text{if } k_x^2 + k_y^2 > NA_{obj}\frac{2\pi}{\lambda} \end{cases} \tag{3-2}$$

A full derivation of eq. (3-1) can be found in appendix A-1. Stitching the unique low resolution spectra together, a high resolution spectrum can be constructed which corresponds to a large NA. However, the spectrum obtained only contains the samples amplitude information while still misses the essential phase information [32]. This is obtained by using the Fourier Ptychographic phase retrieval technique described in section 3-3. Once the spectral amplitude and phase are known, the inverse Fourier transform can be applied to obtain the objects full complex field. The resolution of this field corresponds to a numerical aperture depending on the NA of the objective lens NA_{obj} and the largest sample illumination angle NA_{ill}fig. 3-3.

$$NA_{final} = NA_{obj} + NA_{ill} \tag{3-3}$$

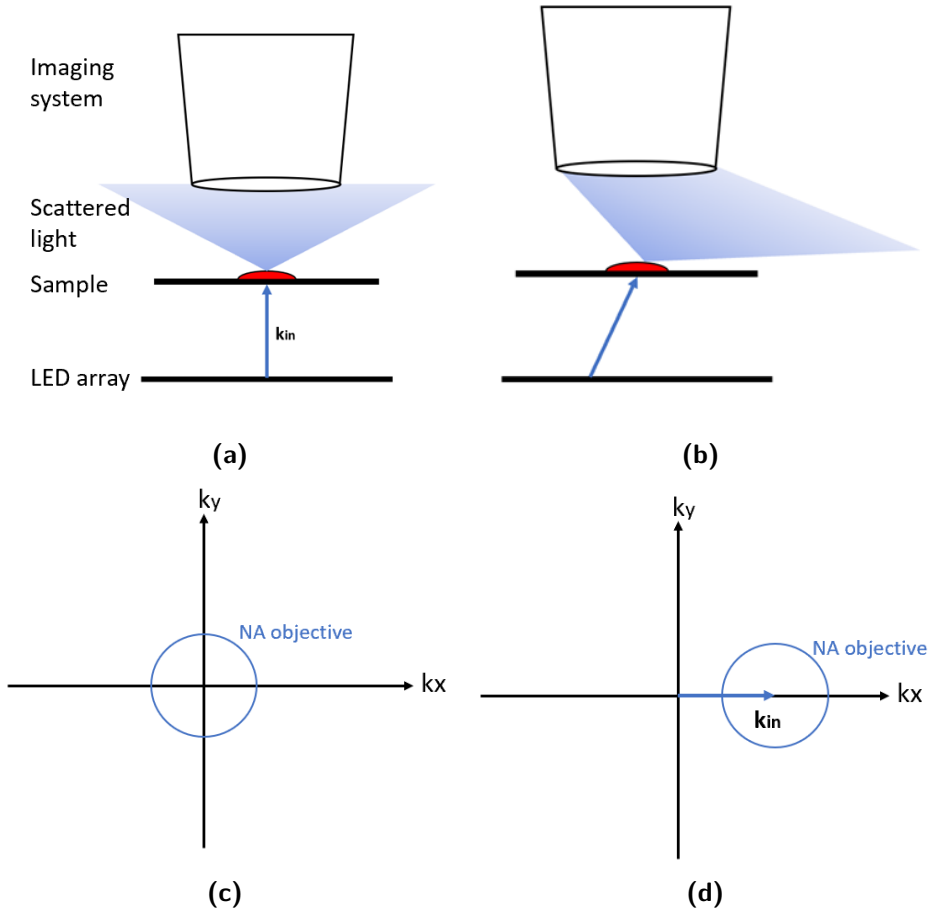

Figure 3-2: (a)Visualization of scattering by the sample under normal incident light (b) Visualization of scattering by the sample under angled incident light (c) Fourier Spectrum corresponding to normal incidence (d) Fourier Spectrum corresponding to angled incidence

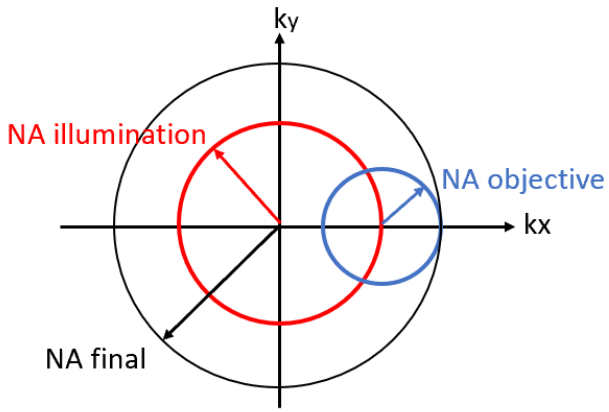

Figure 3-3: The final Synthetic Numerical Aperture of the reconstructed image is sum of the NA of the objective and the largest illumination angle.

3-2 Phase Retrieval

In order to synthesize the full complex field of the object, its phase information is required. Although there are ways to measure phase using interferometry or wave front sensors, these require intricate and expensive setups. A less expensive solution is computational reconstruction of the phase by means of phase retrieval algorithms. These make use of intensity measurements $I(x, y)$ and system a priori information (e.g. Pupil of the optical system). The mathematical problem of phase retrieval can then be formulated as finding a complex field $X(x, y)$ which satisfies:

$$\begin{aligned} \text{find} \quad & X(x,y) \\ s.t. \quad & |X(x,y)|^2 = I(x,y) \end{aligned}$$

Which is equivalent to minimizing the square error between measured and estimated amplitude:

$$\min_X \quad E(x,y) = \sum_{x,y} (I(x,y) - |X(x,y)|^2)^2 \tag{3-4}$$

3-2-1 Alternating Projection

Alternating projection algorithms solve the phase retrieval problem by iterating between distinct data sets based on the available data and a priori system information. The Error Reduction algorithm (also known as, Gerchberg-Saxton algorithm [33]) is widely used due to its simplicity and intuitive approach to the problem. It defines two sets. The first set $\mathbb{P}$ contains all complex fields with spectra that fall within the systems pupil eq. (3-2). The second set $\mathbb{A}$ contains all fields with amplitudes corresponding to the measured image $I(x, y)$. An initial guess of the complex field $X_0 = I(x, y) \exp(j\mathbf{1})$ is then projected onto the two

data sets using respective projection operators. Projection of the estimate onto $\mathbb{P}$ is done by multiplying the estimates spectrum with the pupil function, donated by the operator $\mathbf{P}_{\mathbb{P}}$:

$$\mathbf{P}_{\mathbb{P}} = \mathcal{F}^{-1}\mathcal{P}\mathcal{F}(X_k) \tag{3-5}$$

Projection on to $\mathbb{A}$ is done by replacing the complex fields amplitude with the measured image, denoted by operator $\mathbf{P}_{\mathbb{A}}$:

$$\mathbf{P}_{\mathbb{A}} = \frac{X_k}{|X_k|}\sqrt{I} \tag{3-6}$$

However, set $\mathbf{P}_{\mathbb{A}}$ in non-convex, resulting in this being a non-convex optimization for which no optimal solution can be guaranteed as the algorithm can get stuck in local minima [34]. Other alternating projection algorithms [9, 34] attempt to improve the convergence properties of the algorithm by modifying the sets between which is projected. Tracking the algorithms convergence at iteration k can be done using the relative error metric:

$$\mathcal{E}(k) = \frac{||X_k - X_{k-1}||_2^2}{||X_{k-1}||_2^2} \tag{3-7}$$

When $\mathcal{E}$ falls below a predefined value ϵ the algorithm does not make enough progress and exits the loop. It is also possible to use other error metrics.

Algorithm 1: Error-Reduction, Gerchberg-Saxton algorithm

Data: Intensity image: $I(x, y)$, pupil projection $\mathbf{P}_{\mathbb{P}}$ (eq. (3-5)) and amplitude projection $\mathbf{P}_{\mathbb{A}}$ (eq. (3-6))
Result: Reconstructed complex-field X
Initialization of complex field $X_0 = I(x, y)\exp(j\mathbf{1})$, $\mathbf{1}$ = matrix of ones, same size as $I(x, y)$
while $\mathcal{E}(k) \geq \epsilon$ **do**
  $k \longleftarrow k + 1$
  $X_{k+1} = \mathbf{P}_{\mathbb{A}}(\mathbf{P}_{\mathbb{P}}(X_k))$

3-2-2 Gradient Descent

For discussion of gradient descent based phase retrieval algorithms it is convenient to discretize eq. (3-4). The estimate of the high-resolution complex field $X(x, y)$ is vectorized into vector $\mathbf{x} \in \mathbb{C}^{n^2}$. A down-sampling operator $\mathbf{D} \in \mathbb{R}^{m^2 \times n^2}$ is defined to resize the high resolution spectrum into the size of the lower dimensional image. The pupil function $\mathbf{P} \in \mathbb{R}^{m^2 \times m^2}$ is applied as a low pass filter over the down-sampled spectrum. Finally, the Fourier transform and its inverse are defined $\mathbf{F}, \mathbf{F^{-1}} \in \mathbb{C}^{m^2 \times m^2}$. Image formation of $\mathbf{b} \in \mathbb{R}^{m^2}$ is then formulated as:

$$\mathbf{b} = |\mathbf{F^{-1}PDFx}|^2 \tag{3-8}$$

Setting $\mathbf{A} = \mathbf{F^{-1}PDF}$, $\mathbf{A}$ is the image formation operator and eq. (3-8) can be rewritten:

$$\mathbf{b} = |\mathbf{Ax}|^2 = (\mathbf{Ax})^* \cdot \mathbf{Ax} \tag{3-9}$$

The cost function which is minimized during phase retrieval then becomes:

$$E(\mathbf{x}) = ||(\mathbf{Ax})^* \cdot \mathbf{Ax} - \mathbf{b}||_F^2 \tag{3-10}$$

$||\cdot||_F$ is the Frobenius norm, calculated as $||\mathbf{Z}||_F = \sqrt{\sum_{i,j} \mathbf{Z}_{i,j}^2}$. $E(x)$ is optimized by iteratively updating $\mathbf{x}$ using a gradient descent approach witch step size α and $\nabla E(\mathbf{x})$ the gradient of the objective:

$$\mathbf{x}_{k+1} = \mathbf{x}_k - \alpha \nabla E(\mathbf{x}) \tag{3-11}$$

$E(\mathbf{x})$ is a non-holomorphic function (real valued function with complex variables) and as a result its derivative with respect to the complex variables is not defined. This can be circumvented by using Writinger derivatives [35] to define the gradient of $E(\mathbf{x})$. In this case, $E(\mathbf{x})$ is defined as the gradient with respect to the complex conjugate of the complex variable $\nabla E(\mathbf{x}) = 2\nabla_{x^*} E(\mathbf{x})$ [36]:

$$\nabla_{\mathbf{x}^*} E(\mathbf{x}) = \mathbf{A}^H((|\mathbf{Ax}|^{\circ 2} - \mathbf{b}) \cdot \mathbf{Ax}) \tag{3-12}$$

$$= -\mathbf{A}^H(\mathbf{b} \circ \frac{\mathbf{Ax}}{|\mathbf{Ax}|} - \mathbf{Ax}) \tag{3-13}$$

With $(\cdot)^{\circ(\cdot)}$ the Hadaman power and $(\cdot) \circ (\cdot)$ Hadaman multiplication.

Notice that $\mathbf{b} \circ \frac{\mathbf{Ax}}{|\mathbf{Ax}|}$ of is the same as eq. (3-6) in the Gerchberg-Saxton algorithm and $\mathbf{Ax}$

Algorithm 2: Phase Retrieval using gradient descent method

Data: Image formation operator $\mathbf{A}$, measurement $\mathbf{b}$ and initial guess of high-resolution sample $\mathbf{x}_0$ and step size α
Result: Reconstructed high-resolution spectrum $\mathbf{x}$
Initialization of $\mathbf{x}_0$ is up-sampled image $\mathbf{b}$
while $\mathcal{E}(k) \geq \epsilon$ **do**
  $k \longleftarrow k + 1$
  $\mathbf{x}_{k+1} = \mathbf{x}_k - \alpha \nabla E(\mathbf{x})$

corresponds to the pupil projection step eq. (3-5). By rewriting eq. (3-11) one can show that for a unit step size $\alpha = 1$, eq. (3-11) is the same as the Alternating projections update step, which shows that the two algorithms are basically the same [9].
To increase convergence speed and stability of a gradient based method the Hessian $\mathcal{H}$ containing the second order derivatives of the cost function can be used. The new step update then becomes:

$$\mathbf{x}_{k+1} = \mathbf{x}_k - \alpha \mathcal{H}^{-1} \nabla E(\mathbf{x}_k) \tag{3-14}$$

Because the Hessian can be singular and calculating the Hessian scales quadratically with size of the image, approximation of the Hessian such as Davidon-Fletcher-Powell and Broyden-Fletcher-Goldfarb-Shannon is preferred to ensure stability and computational efficiency [37, 38].

3-3 Fourier Ptychographic Phase retrieval algorithm

The Fourier Ptychographic phase retrieval algorithm is an extension of the phase retrieval methods discussed in section 3-2. Instead of using a single image, the objects complex field

$\mathbf{x} \in \mathbb{C}^{n^2}$ is reconstructed using low-resolution images $\mathbf{b}_i \in \mathbb{R}^{m^2}$, with $n > m$, and i denoting the LED-number used $i = 1, ..., N_{im}$.
In an alternating projection approach an iteration consists of looping through all N_{im} images, extracting the spectral region corresponding to the i^{th} LED and using eqs. (3-5) and (3-6) to update the extracted spectral region. This is done until the error metric eq. (3-7) falls below the predefined value ϵ.
For Gradient based methods, there are two approaches to the update step. The first, is similar to the AP approach and iterates through all images while calculating their corresponding gradient and applying an update step. This is the so called sequential method. The second,

Algorithm 3: Fourier Ptychographic Engine, Sequential method

Data: Image formation operator $\mathbf{A}_i$ for each LED used in optimization,N_{im} measurements $\mathbf{b}_i$ and initial guesse of high resolution sample $\mathbf{x}_0$ and step size α
Result: Reconstructed complex field $G(x, y)$ with $\mathcal{G}(k_x, k_y) = \mathcal{F}(G)(k_x, k_y)$
Initialization of $\mathbf{x}_0$ is up-sampled image $\mathbf{b}_c$, with c the center LED of the array

while $\mathcal{E}(k) \geq \epsilon$ **do**
  $k \longleftarrow k + 1$
  for $i = 1$ **to** N_{im} **do**
    $\mathbf{x}_{k,i+1} = \mathbf{x}_{k,i} - \alpha \nabla E_i(\mathbf{x}_{k,i})$
  $\mathbf{x}_{k+1} = \mathbf{x}_{k,N_{im}+1}$

calculates the gradient corresponding to each image and sums these together to get a global gradient which is used in the update step. This approach is the global method Algorithm 4. There is a trade off between sequential and global methods. In general, global methods are more robust against noise and model mismatches but have longer computational time. Sequential methods are less robust but computationally easier [37].

Algorithm 4: Fourier Ptychographic Engine, Global method

Data: Image formation operator $\mathbf{A}_i$ for each LED used in optimization,N_{im} measurements $\mathbf{b}_i$ and initial guesse of high resolution sample $\mathbf{x}_0$ and step size α
Result: Reconstructed complex field $G(x, y)$ with $\mathcal{G}(k_x, k_y) = \mathcal{F}(G)(k_x, k_y)$
Initialization of $\mathbf{x}_0$ is up-sampled image $\mathbf{b}_c$, with c the center LED of the array

while $\mathcal{E}(k) \geq \epsilon$ **do**
  $k \longleftarrow k + 1$
  for $i = 1$ **to** N_{im} **do**
    $\nabla E_i(\mathbf{x}_k) = \nabla E(\mathbf{x}_{k,i})$
  $\nabla E(\mathbf{x}_k) = \sum_{i=1}^{N_{im}} \nabla E_i(\mathbf{x}_k)$
  $\mathbf{x}_{k+1} = \mathbf{x}_k - \alpha \nabla E(\mathbf{x}_k)$

3-4 Pupil Recovery

To increase the the robustness of the Fourier Ptychograpahic algorithm, it is often combined with a pupil recovery algorithm [39, 40] which reconstructs the pupil aberrations together with the objects complex field. This is done right after each object update step. The pupil is then updated according to the following expression:

$$\mathcal{P}_{k+1}(\mathbf{k}) = \mathcal{P}_k(\mathbf{k}) + \frac{|X_k|X_k^*(\Phi_k - X_k\mathcal{P}_k)}{\max(|X_k|)(|X_k|^2 + \delta_1)} \tag{3-15}$$

The object is updated as followed:

$$X_{k+1} = X_k + \frac{|\mathcal{P}_k|\mathcal{P}_k^*(\Phi_k X_k\mathcal{P}_k)}{\max(|\mathcal{P}_k|)(|\mathcal{P}_k)|^2 + \delta_2} \tag{3-16}$$

The algorithm then works as followed:

Algorithm 5: Fourier Ptychographic Engine, Sequential method

Data: Image formation operator $\mathbf{A}_i$ for each LED used in optimization,N_{im} measurements $\mathbf{b}_i$ and initial guesse of high resolution sample $\mathbf{x}_0$ and step size α
Result: Reconstructed complex field $G(x, y)$ with $\mathcal{G}(k_x, k_y) = \mathcal{F}(G)(k_x, k_y)$
Initialization of $\mathbf{x}_0$ is up-sampled image $\mathbf{b}_c$, with c the center LED of the array

while $\mathcal{E}(k) \geq \epsilon$ **do**
  $k \longleftarrow k + 1$
  for $i = 1$ **to** N_{im} **do**
    $X_{k,i+1}$ updated according to eq. (3-16)
    $\mathcal{P}_{k,i+1}$ updated according to eq. (3-15)
  $X_{k+1} = X_{k,N_{im}+1}$

3-5 Sampling in Fourier Ptychography

Sampling plays an important role in a Fourier Ptychography, there are two sampling criteria: in the spatial and frequency domain. Both play a major role in final reconstruction quality and robustness of the algorithm.

3-5-1 Sampling in Spatial Domain

The Nyquist-Shannon sampling theorem dictates that band limited signals with maximum frequency f_B can be perfectly reconstructed if the sampling frequency is at least twice the bandwidth $f_s > 2f_B$. For lens based imaging systems the images bandwidth is limited by the numerical aperture of the objective lens and the wavelength $f_B = \frac{\mathrm{NA}_{obj}}{\lambda}$. The sampling frequency of the system is determined by the imaging sensor and depends on the pixel pitch

Δx_{sens} and magnification of the optical system M_{sys}, $f_s = \frac{M_{sys}}{\Delta x_{sens}}$. To guarantee perfect reconstruction the following relation must hold:

$$\frac{M_{sys}}{\Delta x_{sens}} > \frac{2NA_{obj}}{\lambda} \tag{3-17}$$

Solutions for pixel aliasing make use of the spatial data redundancy of Fourier Ptychography. By using sub-sampling [41] or up-sampling [42] of images, the imaging sensor size can be altered computationally.

3-5-2 Sampling in Frequency domain

In section 3-1 it was discussed that each LED produces an image corresponding to a unique region in the samples spectral domain fig. 3-2. If a sampling scheme is chosen such that these regions don't overlap fig. 3-4a, the Fourier Ptychography algorithms in section 3-3 reduce to a standard phase retrieval problem. If sampling regions overlap fig. 3-4b, the likelihood of convergence increases. The amount of overlap between two regions, required for successful reconstruction is experimentally found to be around 60% [41, 42].

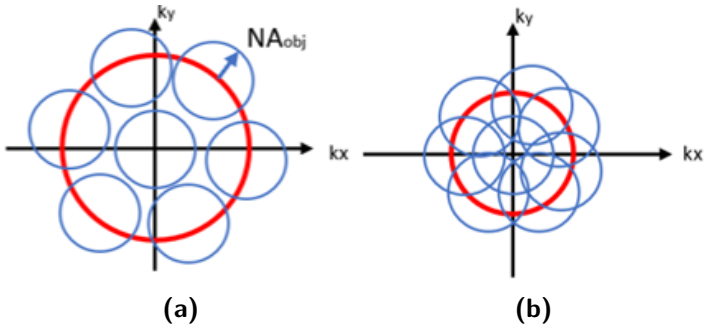

Figure 3-4: (a) sampling such that there is no overlap between neighboring sampled spectra (b) sampling such that there is overlap between neighboring spectra

Chapter 4

Sensitivity of the Fourier Ptychographic System

Fourier Ptychography is a very promising technique for low cost point-of-care devices as it can construct large field of view, high resolution images while also retrieving the phase information of the sample under observation. However, practical implementation poses some challenges, as the theory doesn't take into account factors such as image quantization, LED array misalignment, partial coherence of the light source and many more. These practical limitations result in discrepancies between the theory and practice causing challenges in the development and implementation of physical setups.
Many of these challenges have been addressed, such as calibrating the incident LED angles [43, 44], retrieving aberrations induced by the optical system [45, 39] and reducing the effect of partial coherence of the light source [46, 47]. However, how these factors exactly affect the reconstruction quality have received little attention. Therefore, to better understand the sensitivity of Fourier Ptychography, an in depth look at quantization by limited dynamic range , drop-off of intensity of angled illumination and partial coherence of the source is of critical importance. In this chapter, the practical influence of the factors are analyzed by first introducing the required extensions to the image formation model to facilitate the sensitivity analysis of the different factors, followed by an analysis of their impact on reconstructions with only bright field images and reconstructions extended with dark field images. Finally, potential practical solutions are proposed to deal with these issues.

4-1 Simulation Setup

Simulations make use of 3 sets of two, 16-bit gray-scale images, making up the amplitude and phase of the simulated object fig. 4-1. This is done in order to compare global trends in convergence behavior and exclude image dependent behavior and will allow comparison of the different image sets [1].

[1] All images were obtained from http://imagecompression.info/test_images/

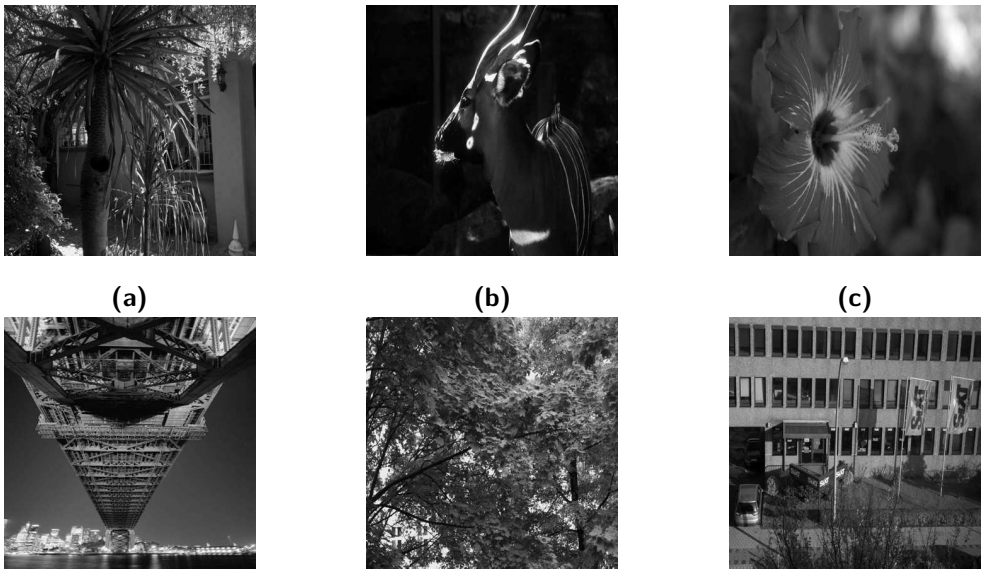

Figure 4-1: Image Sets used in simulations: (a & d) Amplitude and phase of image set 1; (b & e) Amplitude and phase of image set 2; (c & f) Amplitude and phase of image set 3

The number of iterations for each simulation is set to 20 using the original proposed Fourier Ptychographic algorithm [7], based on Gerchberg-Saxton [9]. Simulation make use of 81 bright field images and are expanded to 441 when dark field images are added. Both will make use of a sampling sequence that starts at the center and spirals outwards fig. 4-2.

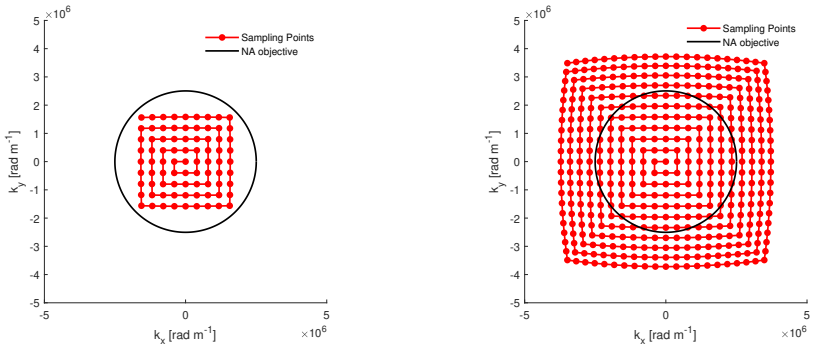

Figure 4-2: (a) Sampling sequence for 81 bright field images; (b) Sampling sequence for 441 images, combination of bright and dark field

It was decided to utilize multiple error metrics to allow, amplitude, phase and spectral errors between reconstruction $\tilde{X}_k$ at iteration k to be compared with the original object X. Both amplitude and phase use the Normalized root mean square error metric:

$$\mathcal{E}_{amp}(k) = \frac{|||\tilde{X}_k| - |X|||_2^2}{||X||_2^2} \tag{4-1}$$

$$\mathcal{E}_{phase}(k) = \frac{||\sphericalangle(\tilde{X}_k) - \sphericalangle(X)||_2^2}{||\sphericalangle(X)||_2^2} \tag{4-2}$$

The spectrum is tracked using an off set invariant metric [48]:

$$\mathcal{E}_{spec}(k) = \frac{||\mathcal{F}(X) - \alpha\mathcal{F}(\tilde{X}_k)||_2^2}{||\mathcal{F}(X)||_2^2} \tag{4-3}$$

$$\alpha = \frac{\mathcal{F}(X)\mathcal{F}(\tilde{X}_k)^*}{|\mathcal{F}(\tilde{X}_k)|^2} \tag{4-4}$$

The parameters used in the simulation were chosen, to resemble the physical setup in the lab, an overview of the most important parameters is found in table 4-1. Any changes in simulation parameters are explicitly mentioned.

Table 4-1: List of important parameters of physical Setup, used in simulations

System parameters	
Numerical aperture objective	0.25
Effective focal length	18 mm
Focal length tube lens	100 mm
Image size	100 x 100 pixels
Pixel size	3.45μm
Array size	32 x 32 LEDs
Pitch LEDs	4 mm
Array sample distance	100 mm
Radius Light emitting area LED	0.5mm
Mean emitting wavelength	633nm

4-2 Quantization

Most imaging-based applications assume that the image obtained is the intensity of the incoming optical signal. This is an idealization as usually this signal is converted into an image through multiple steps fig. 4-3.

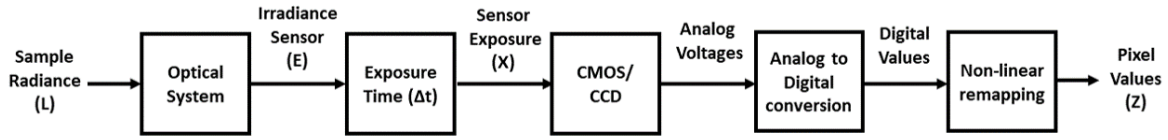

Figure 4-3: Process of the imaging sensor of converting a radiance map into pixel values

When the sample is illuminated by the LED array, it will have a radiance distribution which passes through the optical system and is focused onto the imaging sensor which determines the number of incident photons per unit time step or irradiance E. The irradiance and exposure time Δt of the camera, determine the amount of photons that enter the imaging sensor, also referred to as the sensor's exposure X. This is then converted into analog voltages which are then digitized. This digitization step determines the characteristics of the final image. The digitization process is determined by the camera's characteristic function $f(\cdot)$, which maps digital values onto pixel values Z, and the gamma-characteristic γ, a metric that describes the linearity of the cameras characteristic function. Together they sort the radiance value into bins based on the cameras dynamic range/bit-depth b. This mapping of radiance values to pixel values introduces quantization noise which is caused by the radiance values being sorted into 2^b available bins of the camera.

4-2-1 Model modification: including quantization/camera bit-depth

To analyze the effect of quantization noise, a simple linear response camera is modeled by the characteristic function eq. (4-5).

$$Z_{i,b,\gamma} = f(X_i) = \frac{\left\lfloor 2^b X_i^{1/\gamma} \right\rfloor}{2^b} \tag{4-5}$$

This allows for simulation of an image with dynamic range b and an exposure X_i of the i-th LED illumination, which is bounded between 0 and 1. Simulating some bright field images using eq. (4-5), demonstrates the issues with low dynamic range cameras. The low dynamic range cameras limits the amount of details present in the images figs. 4-4b and 4-4c. This problem is even more evident when acquiring darkfield images, as these have substantially fewer photons enter the imaging sensor, which limits the number of bit levels that can be obtained. This is clearly seen in fig. 4-5, where even at a bit-depth of 6 no signal can be detected fig. 4-5a. It is clear that the dynamic range determines how much detail can be observed. How this affects reconstructions generated by the Fourier Ptychographic algorithm needs to be characterized. Therefore, first an analysis using only bright field images will be conducted to provide some initial insights on how limited dynamic range and quantization noise affect the results. This will be followed by adding the darkfield images and formulating some solutions for dealing with this issue.

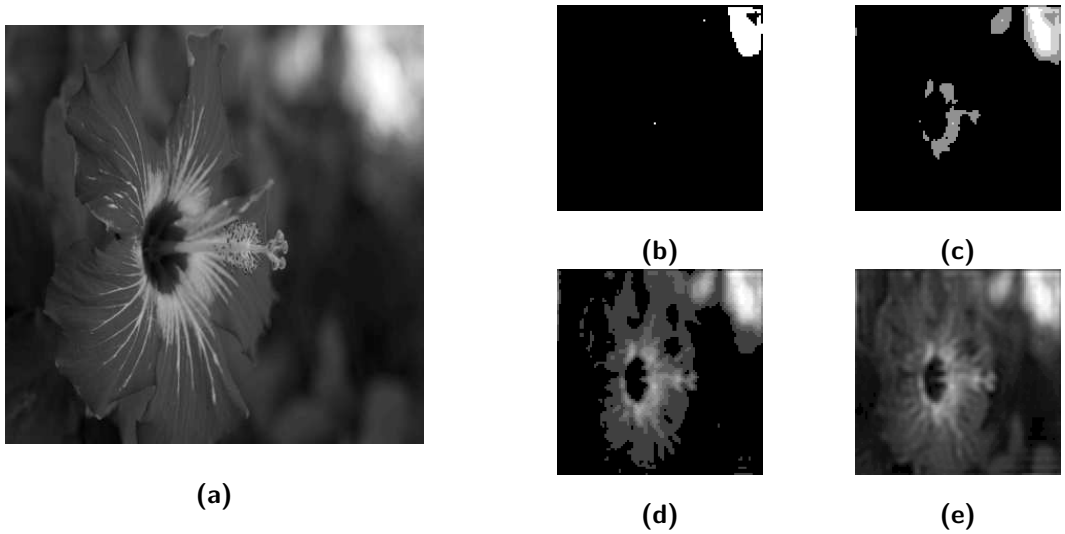

Figure 4-4: (a) original amplitude image; (b) Simulated 1-bit image; (c) simulated 2-bit image; (d) simulated 4-bit image; (e) simulated 8-bit image

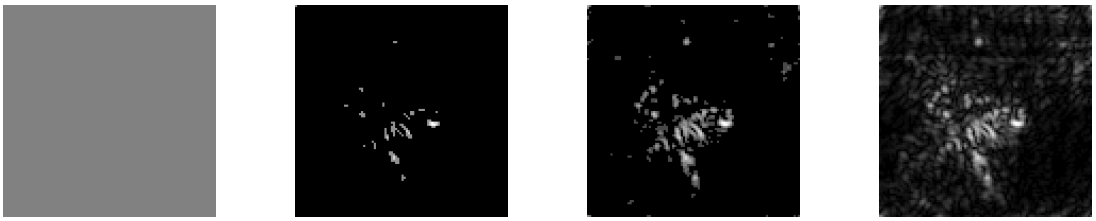

Figure 4-5: Darkfield image with varying bit-depths: (a) 6-bit image, (b) 8-bit image, (c) 10-bit image, (d) 16-bit image

4-2-2 Bright field simulations

To get a grasp on how Fourier Ptychography is affected by quantization noise, several simulations are done for bit-depths varying from 1-16. As one would expect, all errors decrease as the bit-depth of the camera is increased fig. 4-6, with both amplitude and spectrum reaching a stable level around a bit-depth of 10 as shown in figs. 4-6a and 4-6c. The error in the phase however, only stabilizes after a bit-depth of 12 fig. 4-6b. When looking at the reconstruction results of image set 3 for a bit-depth of 4, 6, and 8 fig. 4-7, an interesting observation is made. The areas where the amplitude can be reconstructed are the exact same in which the phase can be reconstructed. There is a clear link between information present in the available images and the area's that can be reconstructed. Figs. 4-7(c,f and i) show the areas of which the imaging sensor was able to receive data. Areas containing no information are marked in blue. These areas correspond to the dark areas in the amplitude and the unreconstructed areas in the phase. This demonstrates that when a high bit-depth camera is used, no severe deteriorating effects will take place. The areas on which information can be obtained will be properly reconstructed in the amplitude and phase. This will have implication for object which have large varying degrees of transmittance, as the high transmitting areas will

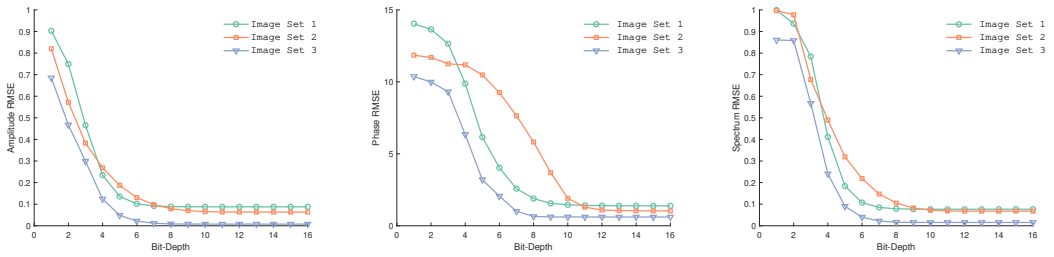

Figure 4-6: Final reconstruction errors for Bright field images with bit-depths varying from 1-16: (a) amplitude errors; (b) phase errors; (c) spectrum errors

be easily reconstructed while low transmitting areas require longer exposure time or higher dynamic range camera.

This demonstrates that to successfully reconstruct the amplitude and phase using only bright field images, information on every part of the object is required in the measured images.

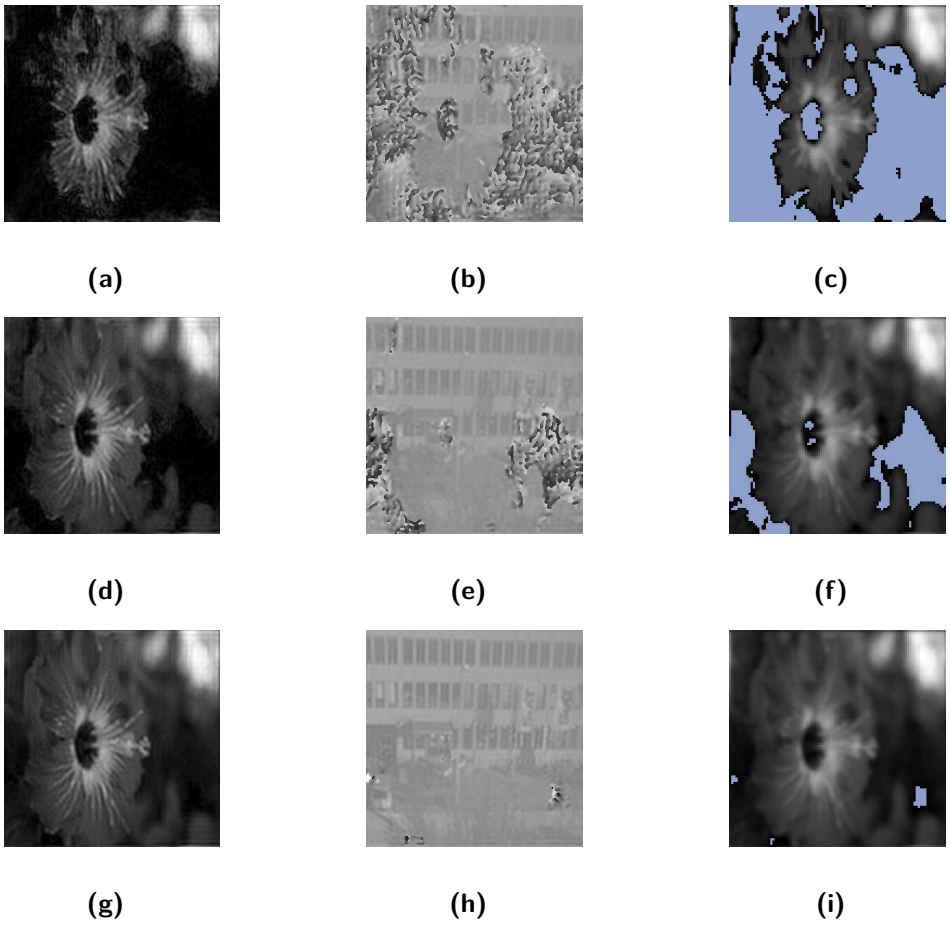

Figure 4-7: Reconstruction results for varying bit-depths and image areas with no information. The areas marked blue indicated that those areas did not contain any information over the 81 obtained images. (a) 4-bit amplitude; (b) 4-bit phase; (c) Information distribution 4-bit; (d) 6-bit amplitude; (e) 6-bit Phase; (f) Information distribution 6-bit; (g) 8-bit amplitude; (h) 8-bit phase; (i) Information distribution 8-bit

4-2-3 Including dark field images

The simulation experiment described in section 4-2-2 was repeated with darkfield images. Obtained results in figs. 4-8a and 4-8c shows that a minimum bit-depth of 12 is required for amplitude and spectrum to reach a stable error level. According to fig. 4-8b, the phase errors converge at around a bit-depth of 10.

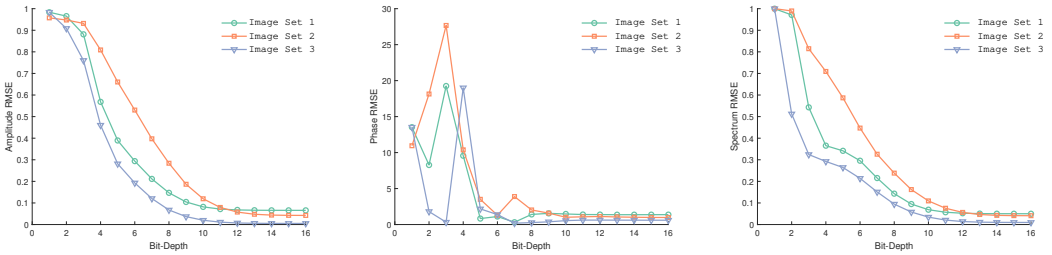

Figure 4-8: Final convergence values for bit-depths ranging from 1-16 for 441 images. (a) Amplitude errors; (b) Phase errors; (c) Spectrum errors

From the reconstruction results shown in fig. 4-9 using 8-,10- and 12-bit, it is clearly evident that that low-bit depth reconstructions suffer from sever blur which reduces the information content of the reconstructed images. This is most likely caused by the inconsistency between neighboring spectra related to the sparsity in the darkfield image. This is illustrated in fig. 4-9a. As the sparsity within the darkfield image decreases, the neighboring spectra will become more consistent, improving the final reconstruction results.

To confirm the darkfield images are responsible for deterioration of the reconstruction, each image update step within the Fourier Ptychographic algorithm is tracked for 2 iterations fig. 4-10a. The RMSE spectrum plot (fig. 4-10a) shows that the inclusion of darkfield images of bit-depth 6 & 8 increases the error significantly while darkfield images simulated by a 10 & 12 bit sensor contribute to convergence. Since the 6- and 8-bit signals have sparse images, they will not contribute to convergence. To solve this problem of sparsity, a way must be found to determine whether the images are sparse or not. By examining the average exposure values (product of exposure time and irradiance) incident on the imaging sensor, it seems that once the average exposure value is above the lowest bit-threshold, the darkfield image starts contributing towards convergence fig. 4-10b.

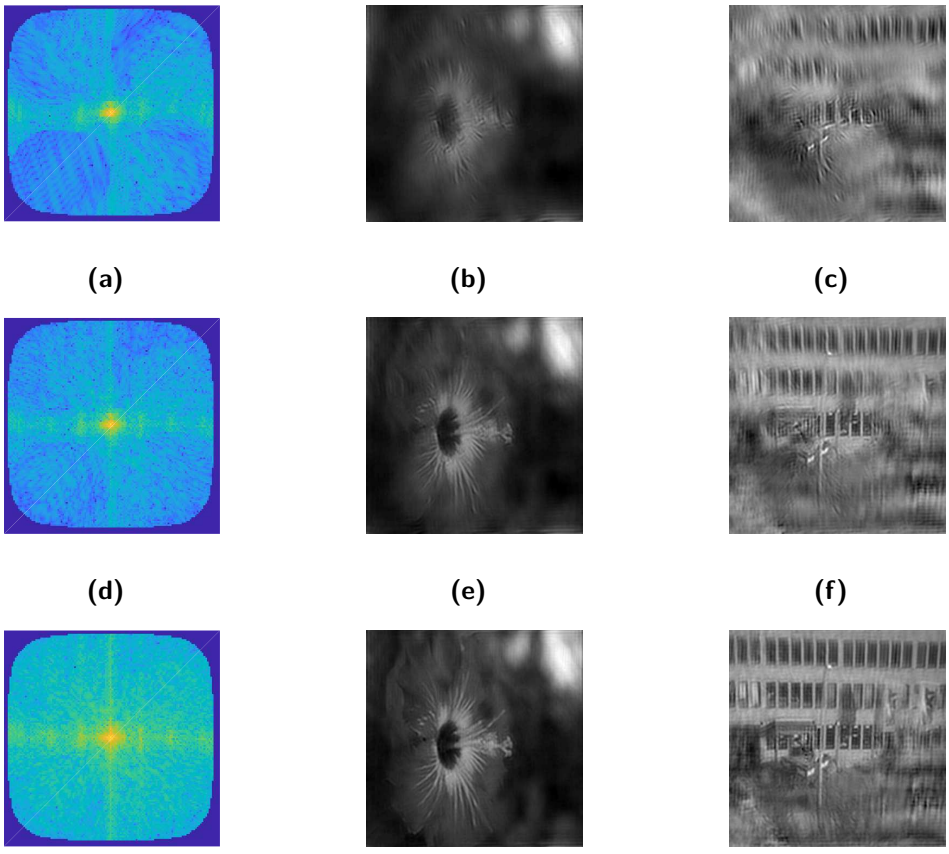

Figure 4-9: Reconstructions for different bit-depths. Notice the spectra of the 8- and 10-bit reconstruction suffering from inconsistency between neighboring spectra: (a) Reconstructed spectrum using 8-bit images; (b) Amplitude of 8-bit reconstruction; (c) Phase of 8-bit reconstruction; (d) Reconstructed spectrum using 10-bit images; (e) Amplitude of 10-bit reconstruction; (f) Phase of 10-bit reconstruction; (g) Reconstructed spectrum using 12-bit images; (h) Amplitude of 12-bit reconstruction; (i) Phase of 12-bit reconstruction

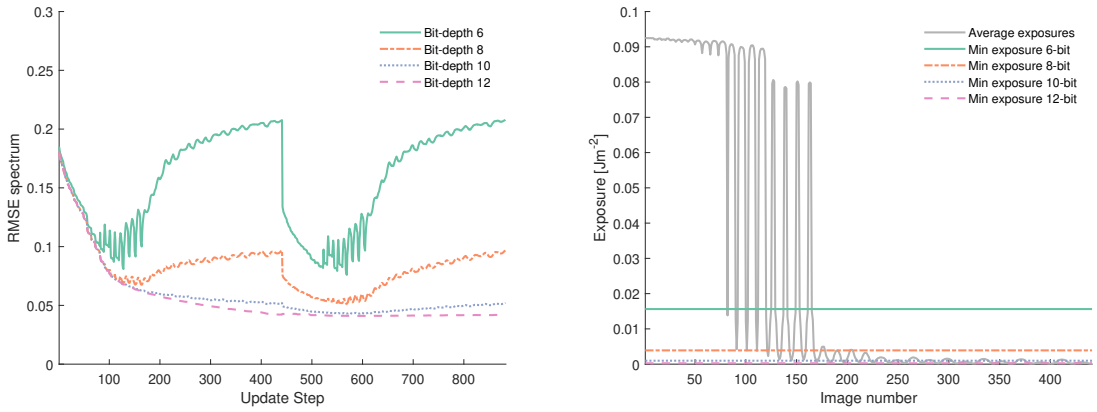

(a) **(b)**

Figure 4-10: (a) Spectrum error at each image update step for bit-depths 6,8,10 and 12; (b) Average incident exposure values of the different images, plotted against the minimum threshold values of 6,8,10,12-bit imaging sensors

4-2-4 Solutions

The most obvious and straightforward solution to overcome quantization noise is to increase the camera's bit-depth. Other solutions consist of increasing the bit-depth computationally using several image processing methods such as HDR-imaging [49] or multi spectral methods [50].
However, based on the insights gained in section 4-2-3, a simple solution is proposed to overcome the limited bit-depth of the camera. Increasing the exposure time for darkfield images allows the average exposure captured by the sensor to exceed the minimum detectable radiance level. This will increase the spatial information in the images and consequently reduce the inconsistency between neighboring spectral components. By increasing the exposure time, the total energy in the darkfield images is increased, causing mismatches between relative energy levels between bright and dark field images. When these images are then used for reconstruction, artifacts are introduced figs. 4-11b and 4-11e. To solve this, the darkfield images obtained with an exposure time ς times longer than the exposure time of the bright field images, are re-scaled by $1/\varsigma$ to fix the energy consistency between bright and dark field images. If these images are then used, the reconstruction results will improve figs. 4-11c and 4-11f.

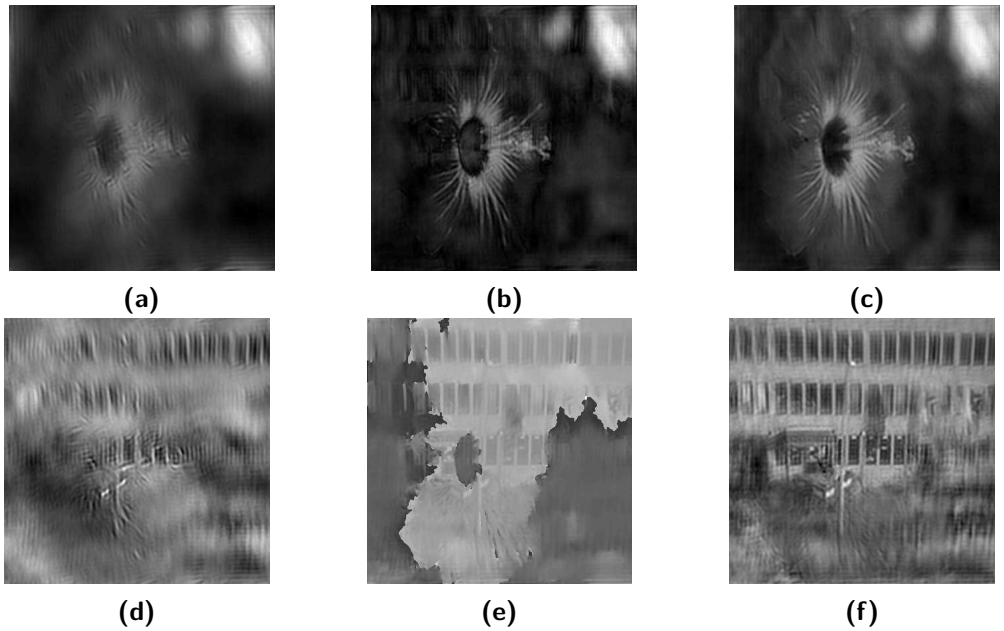

Figure 4-11: Reconstruction results different bright and darkfield exposure time: (a) amplitude reconstruction of 8-bit without exposure difference; (d) phase reconstruction of 8-bit without exposure difference; (b) amplitude reconstruction for 8-bit with exposure time difference but no rescaling; (e) phase reconstruction for 8-bit with exposure time difference but no rescaling;(c) amplitude reconstruction for 8-bit with exposure time difference and with rescaling;(f) phase reconstruction for 8-bit with exposure time difference and with rescaling

4-3 Intensity drop-off

Until now it has been assumed that the intensity of the incoming light has been uniform for all LEDs. In practice this is not the case, as the intensity of the light is decreased by the following factors:

1. irradiance of a surface decreases with squared distance to the light source, causing intensity drop-off $\sim \cos^2 \alpha$

2. Decrease of the object window due to an increased angle, causing an intensity drop-off of $\sim \cos \alpha$.

3. Labertian source intensity drops $\sim \cos \alpha$

Consideration of these factors will cause the intensity on the detector to drop off by a factor of $\cos^4 \alpha_i$ [51], with α_i the incident illumination angle of the i-th LED.

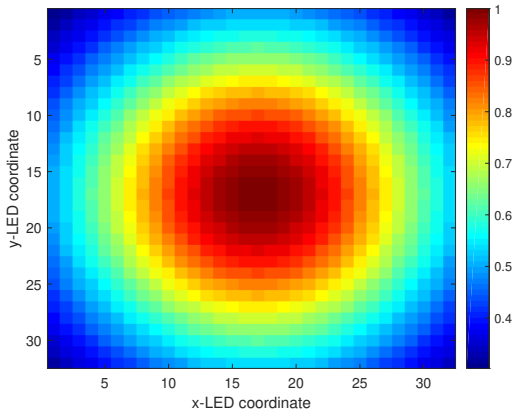

Figure 4-12: Drop off values corresponding to the different LED in the array

4-3-1 Model modification: intensity drop-off of angled illumination

To include the intensity drop-off into the image formation model, an extension is made to eq. (4-5). As the irradiance at the sensor plane decreases by a factor $\cos^4 \alpha_i$, with α_i, the incidence angle of the i-th LED on the sample plane, eq. (4-5) can be rewritten as:

$$Z_{i,b,\gamma} = \frac{\left\lfloor 2^b (E_i \cos^4 \alpha_i \Delta t)^{1/\gamma} \right\rfloor}{2^b} = \frac{\left\lfloor 2^b (X_i \cos^4 \alpha_i)^{1/\gamma} \right\rfloor}{2^b} \tag{4-6}$$

For simulation we will again assume linear response of the camera, by setting $\gamma = 1$ and on the common camera bit-depths: 8,10,12,14 and 16.

4-3-2 Bright field simulations

The final convergence values of simulations using the bright field images, with and without the assumption of intensity drop off, were determined. A constant offset in amplitude error is observed for all of the image sets fig. 4-13a, as well as an error in 8-bit reconstructions for all metrics figs. 4-13a to 4-13c. Comparing the reconstruction results for image set 3, with-

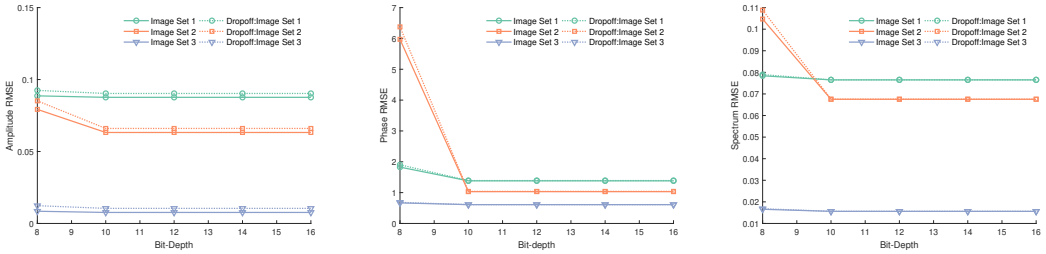

Figure 4-13: Final drop-off convergence errors for 81 images and all 3 image sets compared to the errors with no drop-off effects : (a) Final amplitude convergence values; (b) Final phase convergence values;(c) Final spectrum convergence values

and without intensity drop-off, no aberrations can be observed which indicate an error in amplitude and only a small difference is seen between the two phase reconstructions. Bright

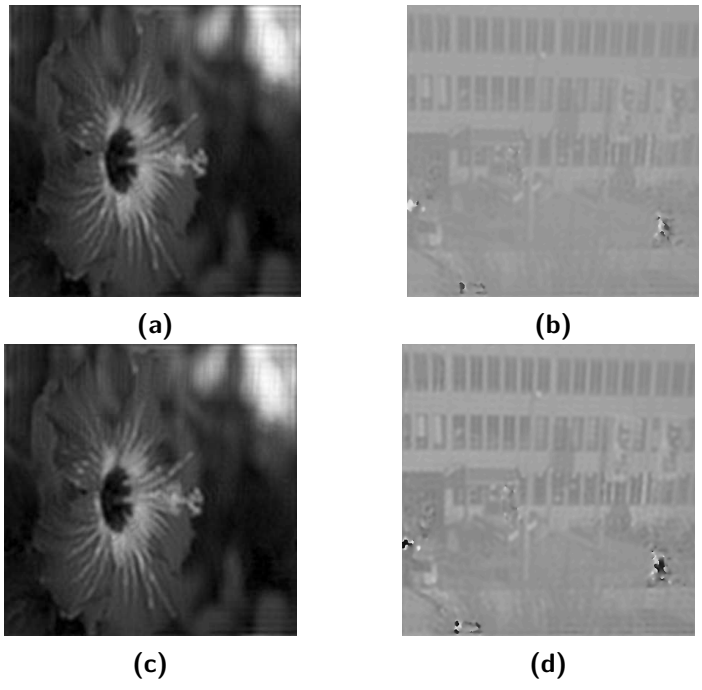

Figure 4-14: 8-bit reconstructions for bright field images: (a) amplitude reconstruction without drop-off; (b) phase reconstruction without drop-off; (c) amplitude reconstruction with drop-off; (d) phase reconstruction with drop-off

field reconstruction therefore appears to be almost unaffected by the effects of intensity drop-off. This is due to the naturally high irradiance values accompanied and low drop-off values.

4-3-3 Including darkfield images

Darkfield images suffer more from intensity drop-off (up to 50%) as they have much lower irradiance values than bright field images and higher incidence angles. When quantization is not considered, the total error induced by intensity drop-off is negligible. Including quantization amplifies the issues discussed in section 4-2-3. Fig. 4-15 compares the errors for the drop-off cases to the non-drop off cases. It is clear, that intensity drop-off increases the error for all metrics. These error increases are caused by the imaging sensor capturing less informa-

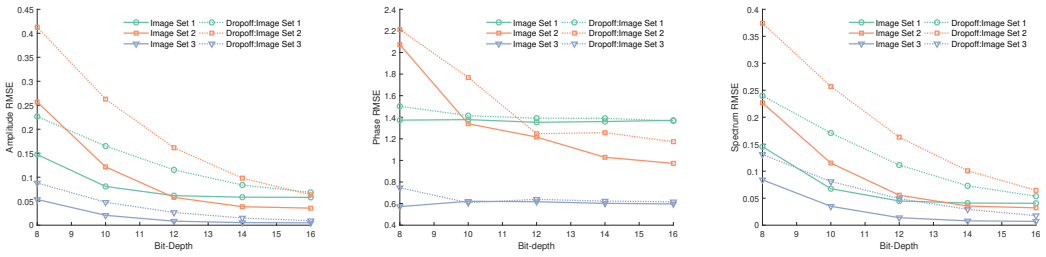

Figure 4-15: Final drop-off convergence errors for 441 images and all 3 image sets compared to the errors with no drop-off effects : (a) Final amplitude convergence values; (b) Final phase convergence values; (c) Final spectrum convergence values

tion due to the decrease in intensity/irradiance which increases the sparsity of the darkfield images and causes mismatches between neighboring high-frequency spectra 4-16. This results in an increased blur in the amplitude and phase compared to the no drop-off cases. This is emphasized in fig. 4-17, in which it is observed that the bright field images in both cases contribute to convergence. When darkfield images are included at around image update step 83, the error increases. However, a larger jump in error is introduced by the images suffing from intensity drop-off.

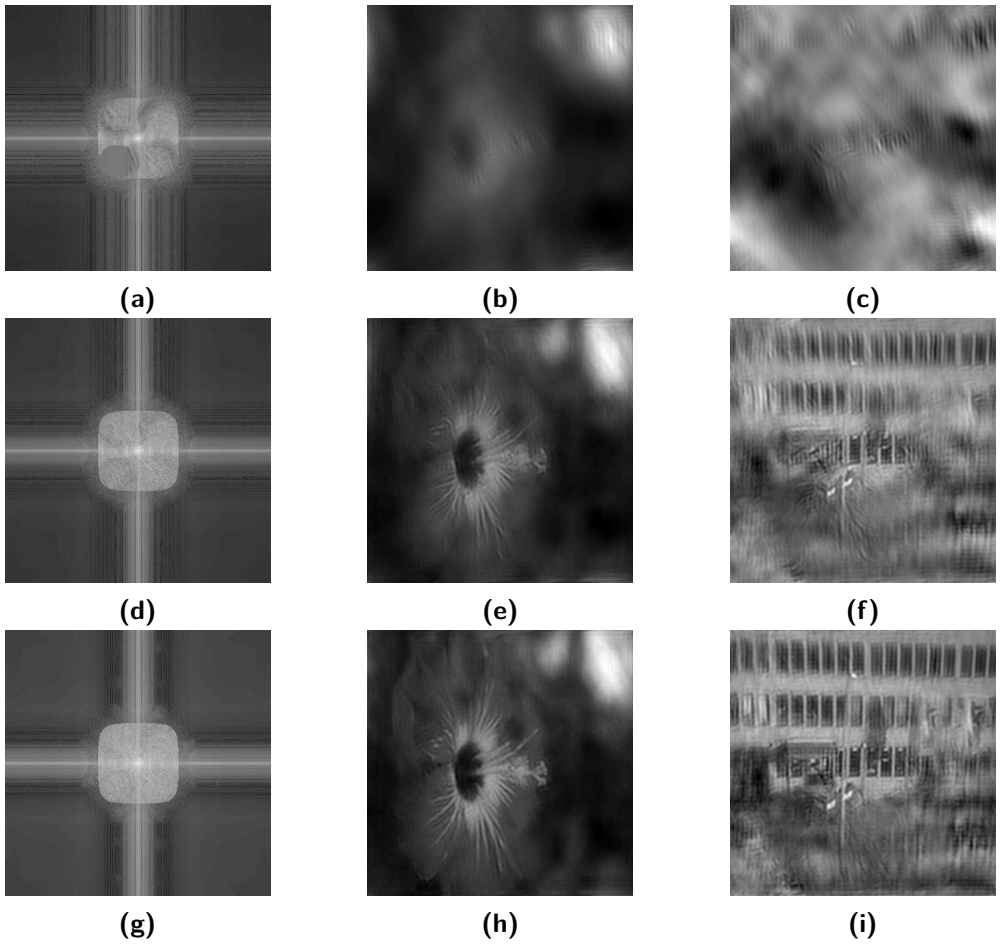

Figure 4-16: Spectrum, amplitude and phase reconstructions with dark field images for different bit depths effect by drop-off:(a) 8-bit spectrum; (b) 8-bit amplitude; (c) 8-bit phase; (d) 10-bit spectrum; (e) 10-bit amplitude; (f) 10-bit phase; (g) 12-bit spectrum; (h) 12-bit amplitude; (i) 12-bit phase

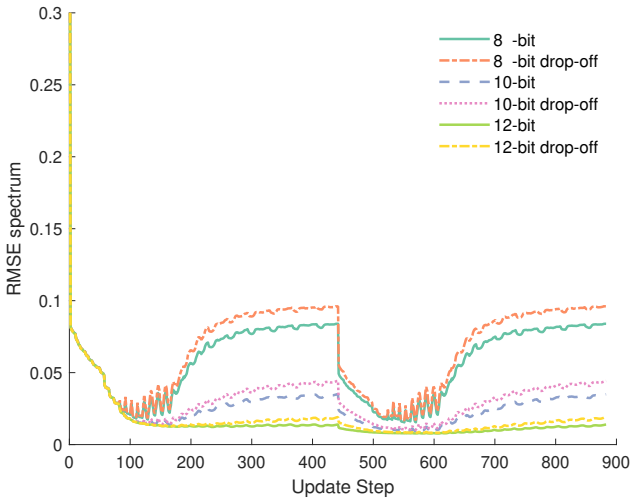

Figure 4-17: Comparison of spectrum errors for each image update step for difference bit depths and with- and without intensity drop-off

4-3-4 Solution

This problem can easily be solved considering this drop-off in intensity during image acquisition. Since the drop-off increase radially with respect to the central LED, a compensation factor κ can be determined for each LED:

$$\kappa_i = \frac{1}{\cos^4(\alpha_i)} \tag{4-7}$$

By increasing the acquisition time of the i-th LED with its respective weighting. The effects of intensity drop-off are mitigated by increased exposure time. Using this as basis, other solutions from section 4-2-4 can be applied to further compensate for the effects of quantization.

4-4 Partial Coherence

Fourier Ptychography is based on the assumption of coherent imaging, which allows images to be expressed as a convolution of the object and the impulse response of the optical system [52]. This assumption does not fully apply when imaging with LEDs in which case it is best described by an extended quasi-monochromatic source. This implies that image formation is better described using a partial coherent model rather than the coherent one. It is possible to circumvent this issue as incoherent sources gain coherence through propagation [53], allowing a domain to be determined at any distance from the source that can assumed to be coherent using the Van Cittert Zernike Theorem [54]. This theorem links the radius of the coherent patch R_{coh} to the radius of the extended light source ρ_s, its mean wavelength $\bar{\lambda}$ and distance between sample and light source h_s.

$$R_{coh} = \frac{0.16\bar{\lambda}h_s}{\rho_s} \tag{4-8}$$

The size of this coherent patch is shown in fig. 4-18, for different distance between LED-array and sample, and for the three emitting wavelengths of the array.

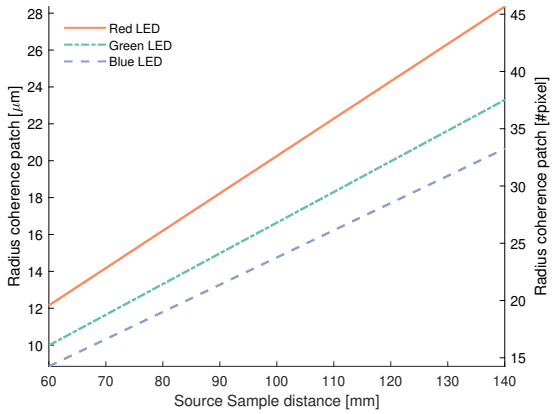

Figure 4-18: Size of the coherent patch size, for increasing distance between LED-array and sample, expressed in dimensions in sample plane and number of in imaging plane.

As the distance from source to sample increases, so does the size of the coherent patch. Therefore, if the reconstructed image size stays within the coherent patch, fully coherent reconstruction can be done.
However, Fourier Ptychography is mostly used for low NA system, which in general have low magnifications and sensors with resolutions of thousands by thousands of pixels. Reconstructing a full field of view would therefore required hundreds of patches to be reconstructed, which is very time consuming and hence inefficient. Therefore, quantification of the impact of partial coherence will help determine whether reconstruction with image sizes exceeding the coherent patch can be done without any major degradation in reconstruction quality. This will be done by adapting the image formation model to allow generation of partial coherent images. The effects of extended source and emitting bandwidths will be investigated, and potential solutions for dealing with the effects of partial coherence will be proposed.

4-4-1 Modifications of the Model

Under partial coherent assumptions, the mutual intensity function in the sample plane $J_0(\mathbf{x}_0, \mathbf{x}'_0)$ and the system transmission function $K(\mathbf{x}_0, \mathbf{x}_1)$ are used to determine the field in the imaging plane J_1.

$$J_1(\mathbf{x}_1, \mathbf{x}_1) = I(\mathbf{x}_1) = \iint_{-\infty}^{+\infty} J_0(\mathbf{x}_0, \mathbf{x}'_0) K(\mathbf{x}_0, \mathbf{x}_1) K^*(\mathbf{x}'_0, \mathbf{x}'_1) d\mathbf{x}_0 d\mathbf{x}'_0 \tag{4-9}$$

The mutual intensity function describes the correlation between two points in a field. In the sample plane these points can be described as $U(\mathbf{x}_0)$ and $U(\mathbf{x}'_0)$, with:

$$U(\mathbf{x}) = o(\mathbf{x}) e^{j(\mathbf{k}_i \cdot \mathbf{x})} \tag{4-10}$$

Allowing the mutual intensity in the sample plane to be written as:

$$J(\mathbf{x}_0, \mathbf{x}'_0) = \langle U(\mathbf{x}_0) U^*(\mathbf{x}'_0) \rangle = \langle o(\mathbf{x}_0) e^{j(\mathbf{k}_i \cdot \mathbf{x}_0)} o^*(\mathbf{x}'_0) e^{-j(\mathbf{k}_i \cdot \mathbf{x}'_0)} \rangle \tag{4-11}$$

This expression can be simplified by decomposing the partially coherent field into mutual coherent modes [55, 56]. Which allows the mutual intensity to be adapted to:

$$J(\mathbf{x}_0, \mathbf{x}'_0) = \sum_{m,l} o(\mathbf{x}_0) e^{j(\mathbf{k}_{i,m,l} \cdot \mathbf{x}_0)} (o(\mathbf{x}'_0) e^{j(\mathbf{k}_{i,m,l} \cdot \mathbf{x}'_0)})^* \tag{4-12}$$

The source can be decomposed into spatial and spectral modes. Decomposition of the source into spatial modes can be done by dividing the partial coherent source into a collection of coherent point sources fig. 4-19a. Spectral modes are determined by representing the source as a collection of point sources emitting at different wavelengths within the bandwidth of the quasi-monochromatic source fig. 4-19b. Combining the two gives all modes related to the quasi-monochromatic source fig. 4-19c. For future use, let m denote the modes corresponding to the extended source and l the different wavelengths in the source's bandwidth.

Under the assumption that imaging is restricted to the isoplanatic region of the system, we can rewrite the systems transmission function as

$$K(\mathbf{x}_0, \mathbf{x}_1) = K(\mathbf{x}_0 - \mathbf{x}_1) \tag{4-13}$$

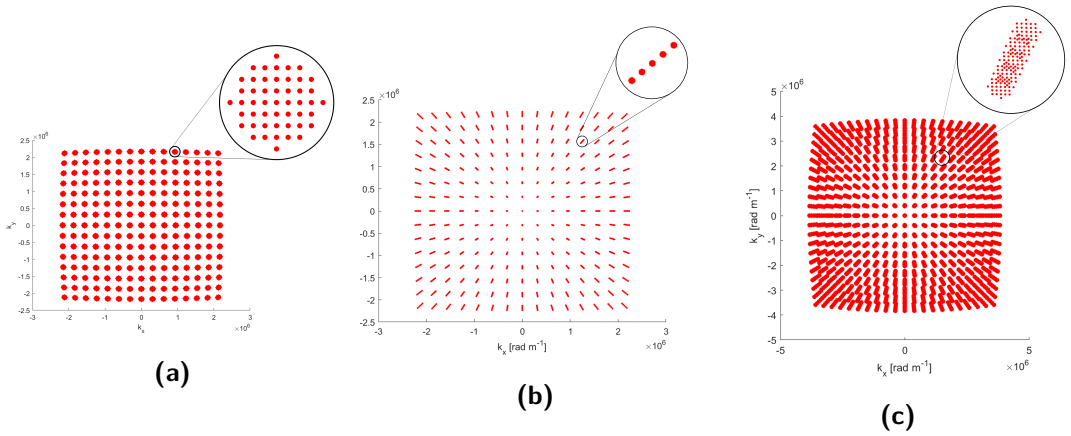

Figure 4-19: (a) Decomposition into spatial modes;(b) Decomposition into spectral modes; (c) decomposition into both spatial and spectral modes

By substituting eqs. (4-12) and (4-13) back into equation eq. (4-9) we get:

$$\begin{aligned} I_i(\mathbf{x}_1) &= \iint_{-\infty}^{+\infty} \sum_{m,l} o(\mathbf{x}_0) e^{j(\mathbf{k}_{i,m,l}\cdot\mathbf{x}_0)} (o(\mathbf{x}_0') e^{j(\mathbf{k}_{i,m,l}\cdot\mathbf{x}_0')})^* K(\mathbf{x}_0 - \mathbf{x}_1) K^*(\mathbf{x}_0' - \mathbf{x}_1) d\mathbf{x}_0 d\mathbf{x}_0' \\ &= \sum_{m,l} \iint_{-\infty}^{+\infty} o(\mathbf{x}_0) e^{j(\mathbf{k}_{i,m,l}\cdot\mathbf{x}_0)} K(\mathbf{x}_0 - \mathbf{x}_1) d\mathbf{x}_0 \iint_{-\infty}^{+\infty} \left(o(\mathbf{x}_0') e^{j(\mathbf{k}_{i,m,l}\cdot\mathbf{x}_0')} K(\mathbf{x}_0' - \mathbf{x}_1)\right)^* d\mathbf{x}_0' \end{aligned} \tag{4-14}$$

eq. (4-14) corresponds to a multiplication of two convolutions, each corresponding to a coherent system response. This can then finally be written as summation of coherent modes:

$$I_i = \sum_{l}^{L} \sum_{m}^{M} |I_{i,m,l}(\mathbf{r})|^2 \tag{4-15}$$

According to eq. (4-15), partial coherent imaging can be seen as an incoherent summation of the images produced by the coherent modes making up the partial coherent source. To implement this in simulations, each LED is divided into M coherent sources which are bound to the light emitting surface, and the band of emitted wavelengths of the LED $[\bar{\lambda}-\Delta\lambda, \bar{\lambda}+\Delta\lambda]$ is divided in L coherent monochromatic point sources. The partial coherent image is obtained by making coherent images for all $M \times L$ modes, which are then added together to give the partial coherent image.

4-5 Effects of partial coherence

To gain insights into incoherence effects of the spatial modes and spectral modes will be discussed separately.

4-5-1 Spatial modes

To get an idea how the reconstruction quality is affected by decomposing the source into spatial modes, the radius of the light source is gradually increased, such that the assumed coherent area in the sample plane decreases. In fig. 4-20 the radius of the coherent patch is plotted against the radius of the light source.

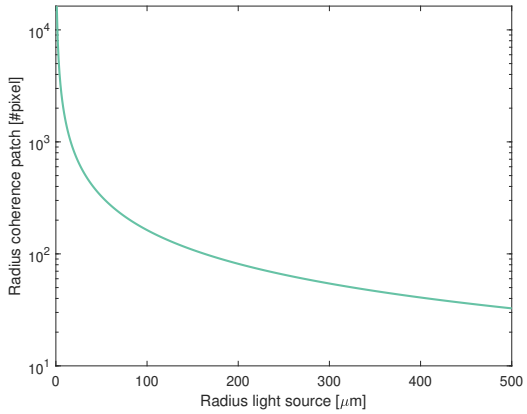

Figure 4-20: Radius of the coherent patch plotted against the radius of the light source size for system parameters described in table 4-1

For simulations the image size is taken to be 100×100 pixels. As long as the corresponding radius of the light source is smaller than $330\mu m$, the effects of partial coherence on Fourier Ptychographic should stay minimal as the reconstruction is coherent according to eq. (4-8).

Bright field simulations

Final reconstruction errors fig. 4-21 show that the effects of spatial modes are negligible as long as the reconstructed area fall withing the coherent patch size. Once the coherence threshold is passed, all metrics show an increase in error as the radius of the light source increases.

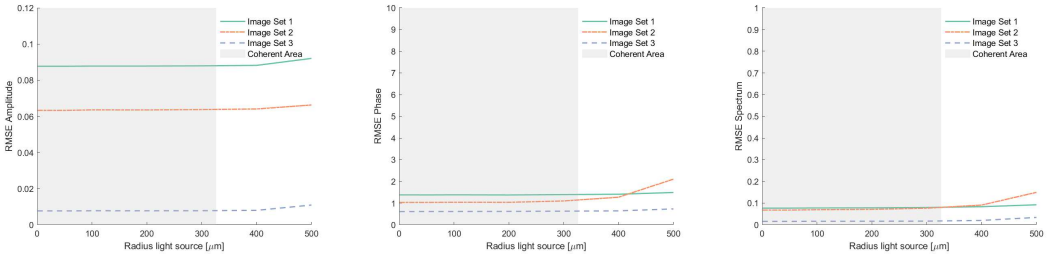

Figure 4-21: Final convergence errors for 81 images and all 3 image sets with the radii of the source varying form 0-500μm: (a) Final amplitude convergence values; (b) Final phase convergence values; (c) Final spectrum convergence values

Taking a closer look at the resulting amplitude and phase of image set 2 for a radius of $1\mu m$ and $500\mu m$, only the phase seems to suffer from wavy artifacts.

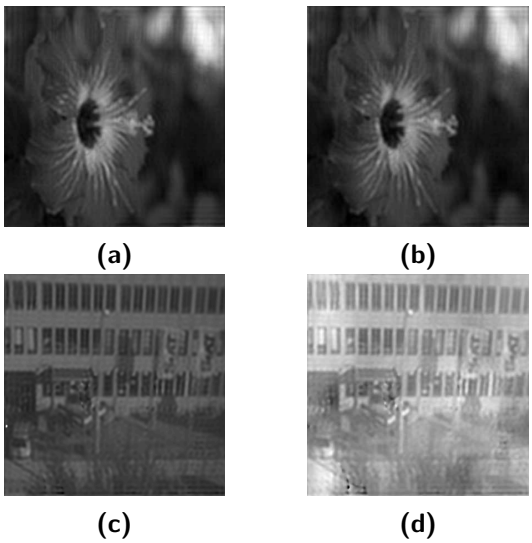

Figure 4-22: (a) Reconstructed amplitude for source radius 1μm;(b) Reconstructed phase for source radius 1μm;(c) Reconstructed amplitude for source radius 500μm;(d) Reconstructed phase for source radius 500μm

These results show that if the reconstruction size is smaller than the coherent patch size, the theory of coherence can be applied. Once this size is exceeded, reconstruction quality will start to deteriorate due to partial coherence.

Including dark field images

Including darkfield images shows that the 3 errors increase linearly with the size of the source, even within the area of coherence fig. 4-23. The reconstruction results for image set 3 fig. 4-24, shows that for larger bandwidths the phase information leaks into the amplitude.

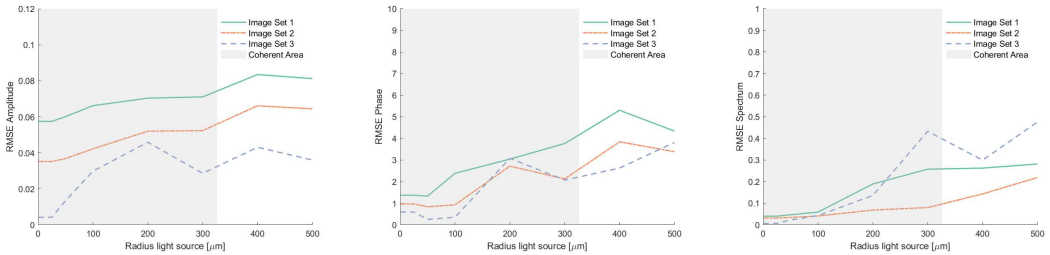

Figure 4-23: Final convergence errors for 441 images and all 3 image sets with the radii of the source varying form 0-500μm: (a) Final amplitude convergence values; (b) Final phase convergence values;(c) Final spectrum convergence values

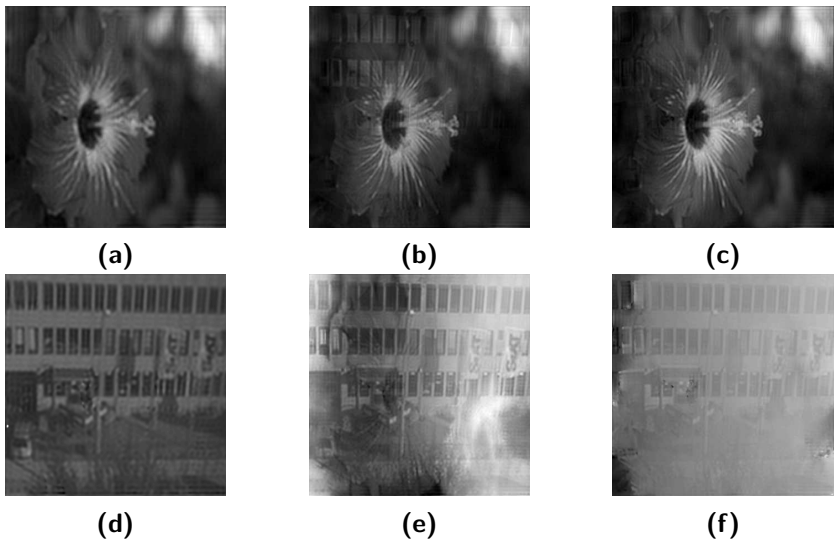

Figure 4-24: (a) Reconstructed amplitude with 441 images and source radius 1μm;(d) Reconstructed phase with 441 images and source radius 1μm;(b) Reconstructed amplitude with 441 images and source radius 300μm;(e) Reconstructed phase with 441 images and source radius 300μm; (c) Reconstructed amplitude with 441 images and source radius 500μm;(f) Reconstructed phase with 441 images and source radius 500μm

To identify the causes of this increase in error, the spectral error is tracked for each image update step for source radii of 100nm, 250nm and 500nm fig. 4-25a.
At image update step 82, the error for source radius 250μm and 500μm increases, while the radius of 100μm increases around update step 125. At update step 166, the dark field images contribute decreasing the error again. The LED sampling points contributing to the negative effect on the reconstruction are shown in fig. 4-25b in blue.

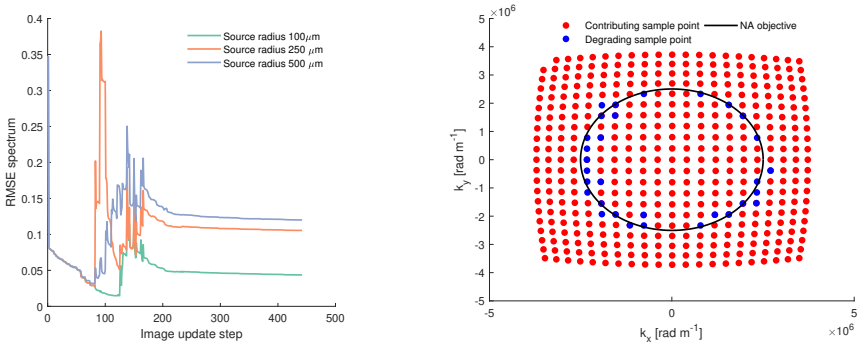

(a) (b)

Figure 4-25: (a) Spectral error for each image update step in the Fourier Ptychographic reconstruction; (b) Visualization of all sampling points which negatively impact the reconstruction

The LEDs with a negative impact on the reconstruction are located on the boundary of the objective numerical aperture, suggesting that LEDs in this location are most sensitive to the effects of the spatial modes.
This increase is caused by spatial modes of the LEDs being both in- and outside the NA boundary, causing the images corresponding to those LEDs to be a summation of both bright- and dark field images. As the size of the source increases, so does the spread of its spatial modes in the objects spectral domain, hence changing the ratio of modes which are located in- and outside the NA boundary. Because the two types of images have different energy contents, this causes a decrease/increase in the total energy of the composite image. To verify this, the energy content of all images for the 3 source sizes are investigated. fig. 4-26a, shows that the energy levels for the 3 source sizes remain the same until image 83 is added. Here mismatches in energy start to occur which are emphasized in fig. 4-26b and **??**.

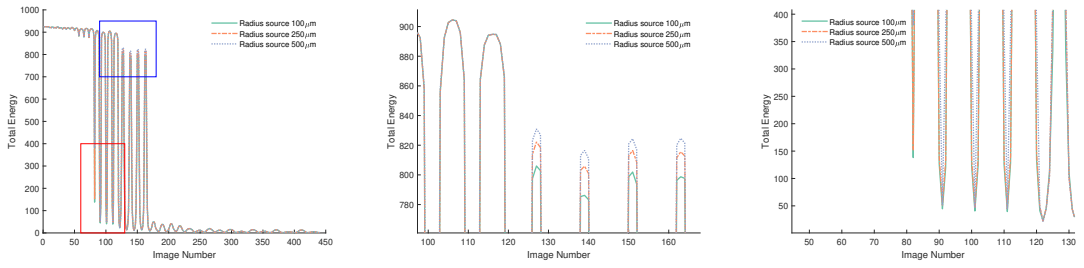

(a) (b) (c)

Figure 4-26: (a) Total energy of each all images for source of radius 100μm, 300μm and 500μm; (b) Magnification of blue box of energy of all images for various source radii sizes;(c) Magnification of red box of energy of all images for various source radii sizes

These deteriorating effects can be mitigated by simply removing the sampling points around the numerical aperture boundary fig. 4-27b.

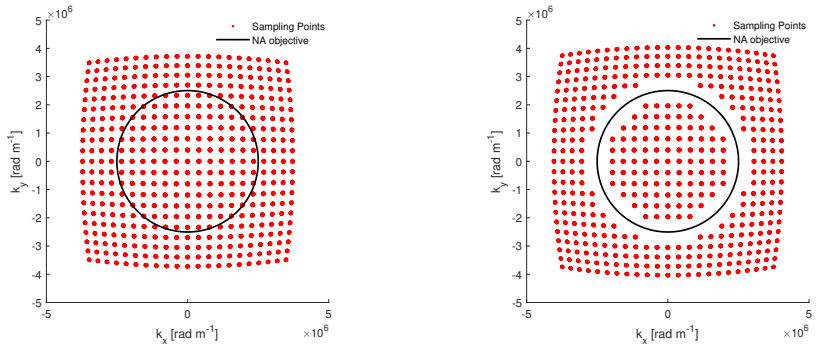

Figure 4-27: Different sampling scenarios: (a) Sampling scenario under coherent assumption, all points represent 1 sampling point; (b) Sampling scenario with spatial modes, each sampling point corresponds to a collection of spatial modes, notice some point are both in and out of the NA circle;(c) Sampling scenario with spatial modes, with LEDs close to the NA circle left out, avoiding spatial modes falling both in and outside of the NA circle

When repeating the simulation with this new sampling sequence, the errors for all 3 metrics fig. 4-29 show the same behavior as in fig. 4-22 with errors only increasing when the dimensions of reconstruction exceed the coherent patch size fig. 4-28.

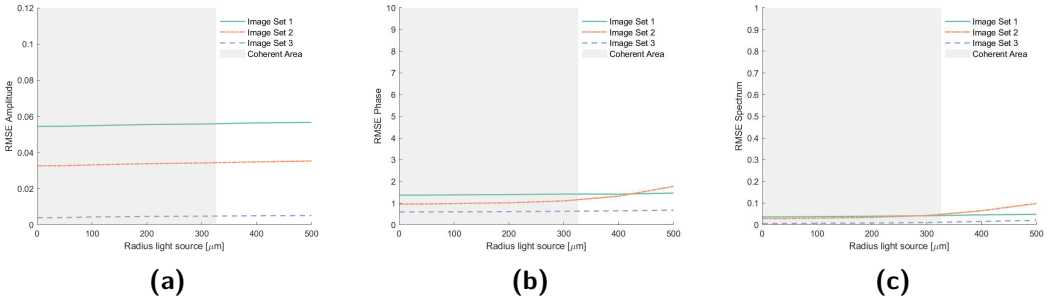

Figure 4-28: Final convergence errors for 441 images excluding LED close to the NA of the objective for and all 3 image sets and source size varying form 1-100nm: (a) Final amplitude convergence values; (b) Final phase convergence values;(c) Final spectrum convergence values

4-5-2 Spectral Modes

To investigate the effect of the spectral modes, the source is assumed a point source with a bandwidth $\Delta\lambda$ which is varied from 0 - 100nm.

Bright field simulations

When reconstructing with bandwidths varying from 1-100nm, no major increases in error are observed fig. 4-29. Only a slight increase is seen around a bandwidth of 20nm which extends out to 60nm before stabilizing again.

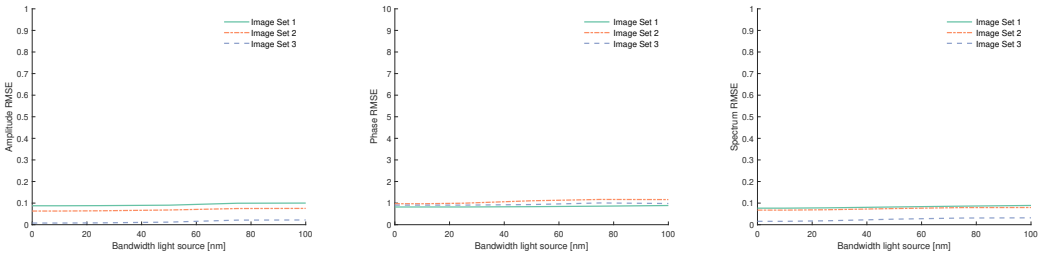

Figure 4-29: Final convergence errors for 81 images and all 3 image sets for bandwidths varying form 1-100nm: (a) Final amplitude convergence values; (b) Final phase convergence values;(c) Final spectrum convergence values

The reconstruction results confirm this observation, as both amplitude and phase reconstructions for bandwidths of 10nm, 50nm and 100nm, visually show no signs of artifacts fig. 4-30f.

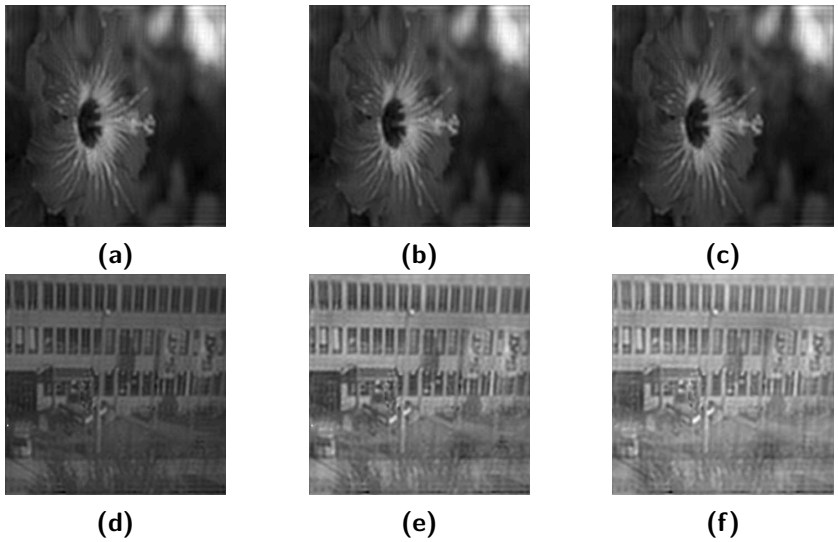

Figure 4-30: (a) Amplitude reconstruction for 10nm bandwidth; (d) Phase reconstruction for 10nm bandwidth;(b) Amplitude reconstruction for 50nm bandwidth; (e) Phase reconstruction for 50nm bandwidth;(c) Amplitude reconstruction for 100nm bandwidth; (f) Phase reconstruction for 100nm bandwidth;

Through these observations it can thus be concluded that reconstruction limited to bright field images are robust against large bandwidths. This robustness could be attributed to low illumination angled LED having a small spread spectral modes fig. 4-31. This causes the partial coherent image to be a summation of only bright field images hence avoiding energy mismatches as discussed in section 4-5-1.

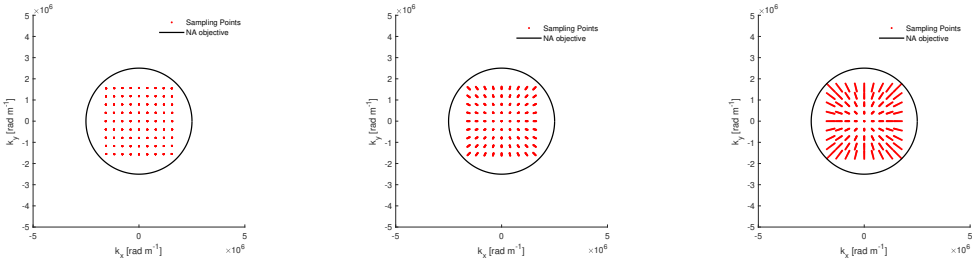

Figure 4-31: Spread of spectral modes for 81 LEDs and varying bandwidths: (a) spread for a bandwidth of 0nm; (b) spread for a bandwidth of 25nm; (c) spread for a bandwith of 75nm;

Including darkfield images

Including darkfield images causes the amplitude errors to increase linearly with bandwidth fig. 4-32a, whereas the phase an spectral errors show massive jumps in error at low bandwidths figs. 4-32b and 4-32c.

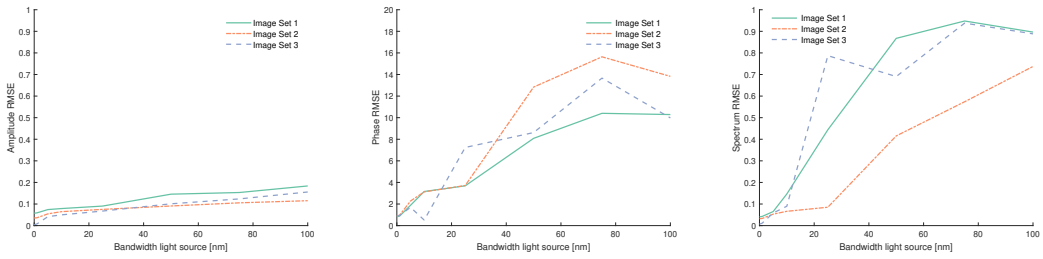

Figure 4-32: Final convergence errors for 441 images and all 3 image sets for bandwidths varying form 1-100nm: (a) Final amplitude convergence values; (b) Final phase convergence values;(c) Final spectrum convergence values

Upon visual inspection, the results for a bandwidth of 1nm show no artifacts figs. 4-33a and 4-33e. At larger bandwidths wavy artifacts in both amplitude and phase reconstructions can be observed which appear to increase in frequency with increasing bandwidth fig. 4-33.

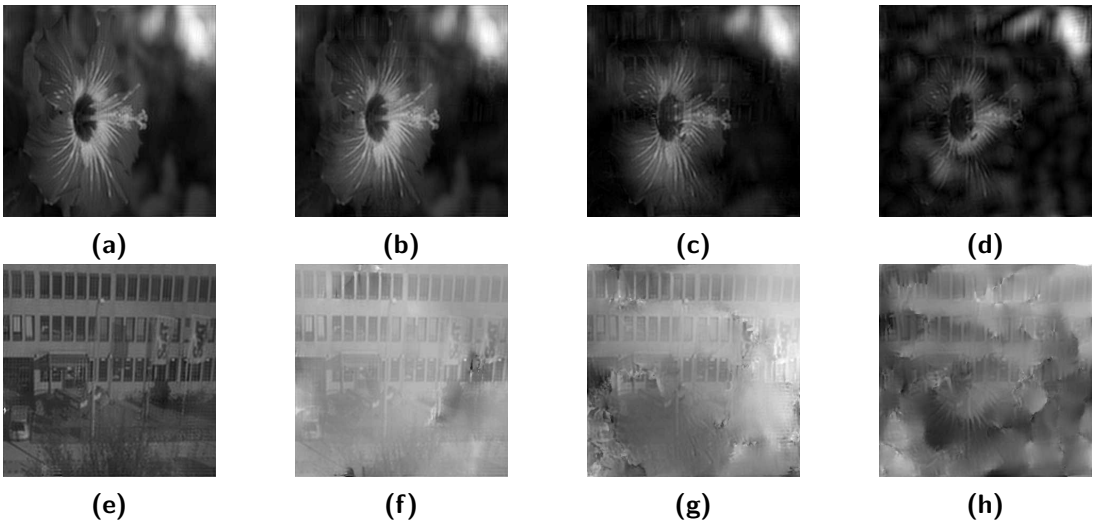

Figure 4-33: Amplitude and Phase reconstruction results for various bandwidths: (a) Amplitude for bandwidth of 1nm;(e) Phase for bandwidth of 1nm; (b) Amplitude for bandwidth of 10nm;(f) Phase for bandwidth of 10nm; (c) Amplitude for bandwidth of 50nm;(g) Phase for bandwidth of 50nm; (d) Amplitude for bandwidth of 100nm;(h) Phase for bandwidth of 100nm;

To identify the cause of this degradation. The error is tracked for 1 iteration for each image update step. Large increases in errors occur at the point LEDs close to the objectives NA are included fig. 4-34. Fig. 4-35 shows that an increase in bandwidth causes a radial increase in the spread of the spectral modes in the objects spectrum, causing LEDs close to object NA to have modes which generate both bright and dark field images. Therefore, the deteriorating effects observed in fig. 4-33 are caused by the same phenomenon observed for the spatial modes.

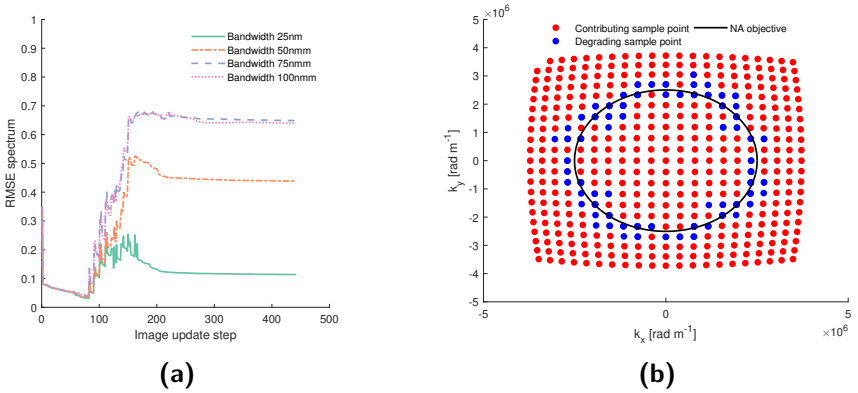

Figure 4-34: (a) Error after each image update in the Fourier Ptychographic reconstruction for bandwidth of 25,50,75 and 100nm;(b) All LEDs with deteriorating contribution

Removing these LEDs such as shown in fig. 4-27a, decreases the reconstruction errors dra-

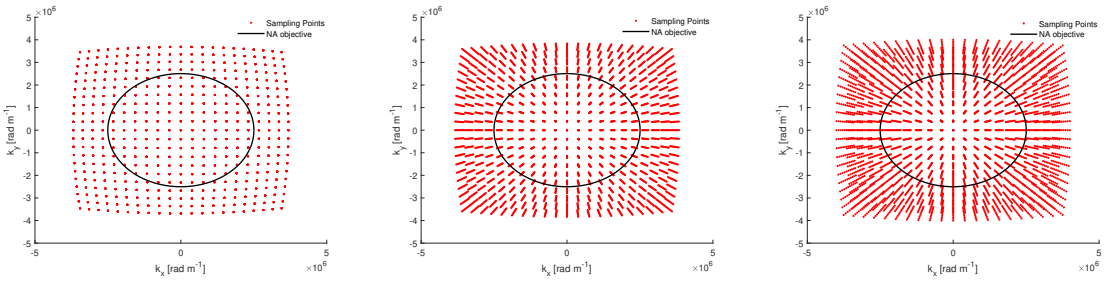

Figure 4-35: Spread of spectral modes for: (a) $\Delta\lambda = 0$nm; (b)$\Delta\lambda = 25$nm;(c) $\Delta\lambda = 50$nm

matically fig. 4-36. The error does increase for increasing bandwidths, which is in line with the reconstruction results fig. 4-37, which show that as the bandwidth increases, artifacts will be increasingly introduced into the phase reconstruction.

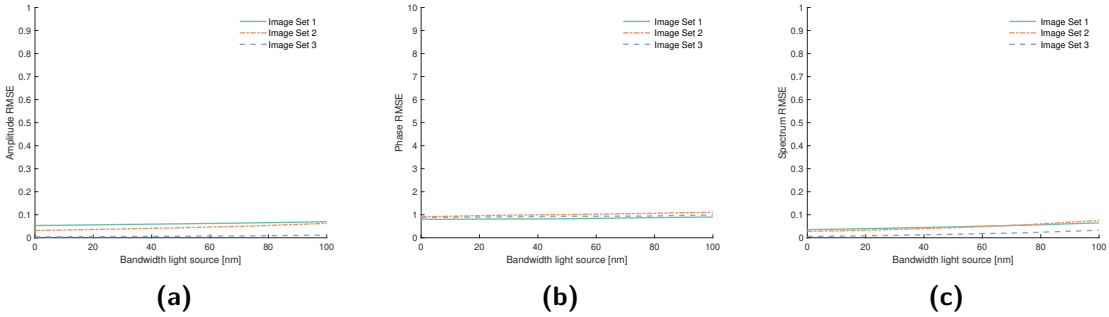

Figure 4-36: Final convergence errors for 441 images and all 3 image sets for bandwidths varying form 1-100nm: (a) Final amplitude convergence values; (b) Final phase convergence values;(c) Final spectrum convergence values

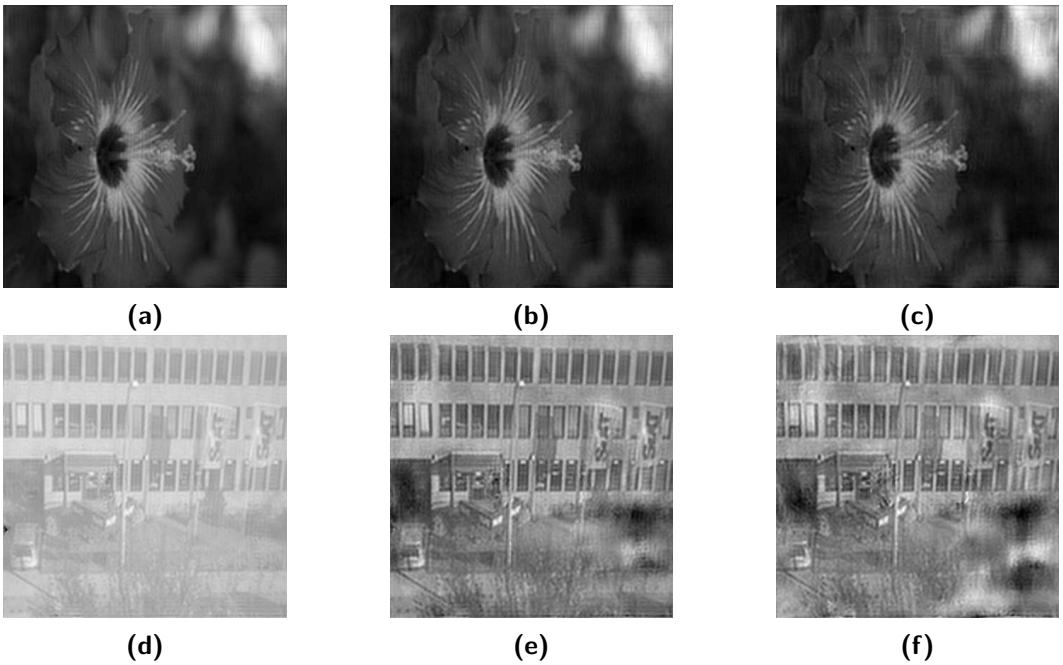

Figure 4-37: Amplitude and Phase reconstruction results for various bandwidths: (a) Amplitude for bandwidth of 10nm;(d) Phase for bandwidth of 10nm; (b) Amplitude for bandwidth of 50nm;(e) Phase for bandwidth of 50nm; (c) Amplitude for bandwidth of 100nm;(f) Phase for bandwidth of 100nm;

4-5-3 Solutions

With the above simulation it was demonstrated that when partial coherence is considered, the algorithm becomes very sensitive to the inclusion of LEDs with illumination angles close to the numerical aperture of the objective lens, and when these corresponding images of these LEDs are excluded from the reconstruction, the performance is greatly improved.
Therefore, if all LEDs are excluded which have partial-coherent modes in both in- and outside the numerical aperture, the method's robustness can be greatly improved. It is possible to formulate a closed form expression of an exclusion band $\mathcal{B}$, depending on the spread of the spatial coherent r_ρ modes:

$$r_\rho = k_0 \frac{\rho_s}{\sqrt{\rho_s^2 + h_{LED}^2}} \tag{4-16}$$

And the spread of the spectral coherent modes r_λ

$$r_\lambda = \Delta_\lambda \nabla_\lambda \tag{4-17}$$

With $\nabla_{\lambda,i}$ being the gradient of sampling point in the objects spectrum of th i-th LED, which is denoted by:

$$\begin{aligned} \nabla_{\lambda,i} &= \frac{\partial \mathbf{k}_i}{\partial \lambda} \\ &= -\frac{1}{\lambda}\mathbf{k}_i \\ &= -\frac{k}{2\pi}\mathbf{k}_i \end{aligned} \tag{4-18}$$

The size of the final bound is then:

$$\mathcal{B} = k_0 \mathrm{NA}_{obj} \pm \max(r_\lambda \nabla_\lambda + r_\rho) \tag{4-19}$$

This bound can be further extended to consider possible LED-array misalignments which also have an influence on the positions of the sampling points of the LEDs. By including uncertainty in translations δ_x and δ_y, uncertainty in LED array-sample distance δ_z and in tip ϕ and tilt ψ of the array and all respective gradients, of which the derivations can be found in Appendix X. The more robust version of the bound hence becomes:

$$\mathcal{B}_r = k_0 \mathrm{NA}_{obj} \pm \max(\Delta_\lambda \nabla_\lambda + \nabla_x \delta_x + \nabla_y \delta_y + \nabla_z \delta_z + \nabla_\psi \psi + \nabla_\phi \phi + r_\rho) \tag{4-20}$$

Chapter 5

Experimental Setup

This section described the system, its components and the image preprocessing algorithms as well as the design process which have lead to the system's current state.

5-1 Current system design

5-1-1 Components Setup

The setup fig. 5-1 comprises a main computer which uses MATLAB to control the LED array to set the illumination light color and the LED position and the camera's exposure time and image acquisition trigger. A schematic of the various components and communication routes is shown in fig. 5-2.

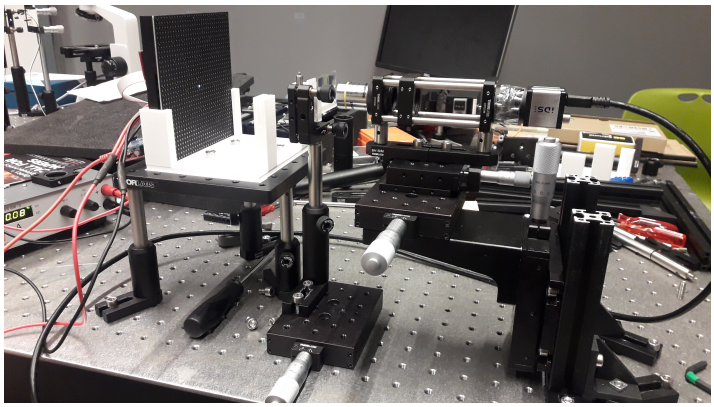

Figure 5-1: Microscope Setup in the lab

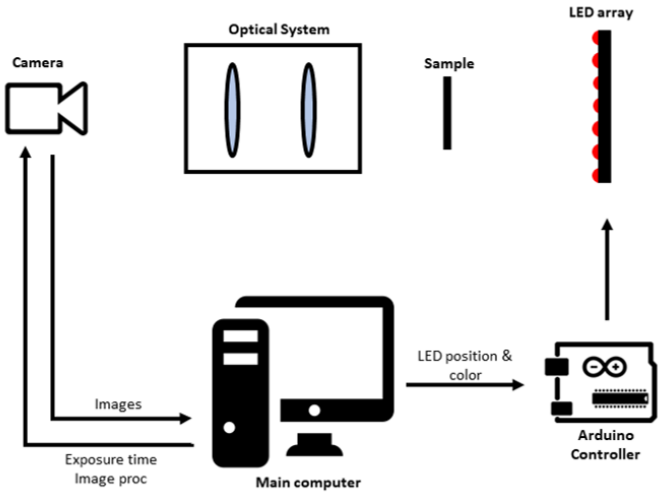

Figure 5-2: Schematic of the various components used in the setup and the data transfer between them.

Camera: IDS UI3070CP-rev2

Images were made using the UI3070CP-rev2, a monochromatic CMOS sensor with a resolution of 2056×1542, a pixel size of $3.45\mu m$ and 8, 10 and 12 bit imaging support. It was controlled through MATLAB, to set the exposure time ($0-1000$ms), sensor gain, black offset, pixel clock, FPS and bit-depth.

Light source: RGB LED array

An Adafruit 32 x 32 RGB LED array with a pitch of 4mm for the LEDs. It is controlled by sending the coordinate of the LED on the array together with the preferred RGB code for the illumination light.

The spectral properties of the LED array were determined using the AvaSpec-ULS3648 spectrometer fig. 5-3 and table 5-1. This setup was used to determined the boundary for which to exclude sampling LEDs.

Table 5-1: Spectral Properties of the Adafruit 32×32 LED array.

	Center Wavelength ($\bar{\lambda}$) [nm]	Minimum Wavelength λ_{min} [nm]	Maximum Wavelength λ_{max} [nm]
Red LED	627.4	580	665
Green LED	522.3	465	595
Blue LED	461.4	420	535

To minimize effects of rotational misalignments of the LED array, a special mount was designed and 3D printed fig. 5-4.

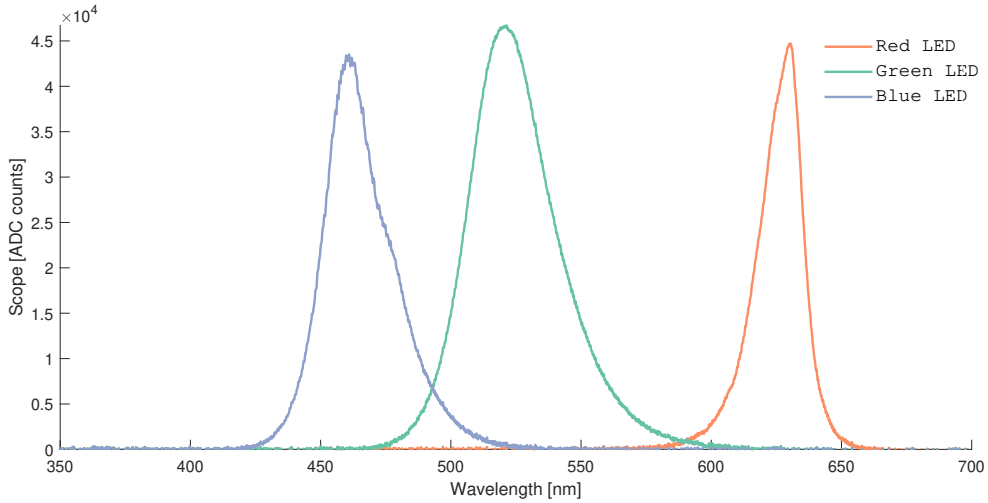

Figure 5-3: spectral content of RGB LEDs of the array

Optical system

The optical system is built around an infinity corrected Olympus 10X Olympus Plan Achromat Objective with a numerical aperture of 0.25, a working distance of 10.6 mm, and an effective focal length of 1mm. An 18mm convex tube lens focuses the image onto the imaging sensor. The optical system is mounted on a pillar with 3 translating stages, providing 3 degrees of freedom for alignment and focusing. The sample is also positioned on a translating stage to facilitate analysis of different fields of view.
During earlier phases of the project it was quite challenging to accurately bring the complete sample in focus due to excessive mechanical play in the mount. A dedicated sample mount was therefore designed and 3D printed and attached to a kinematic mount, to provide full tip and tilt control of the sample fig. 5-5.

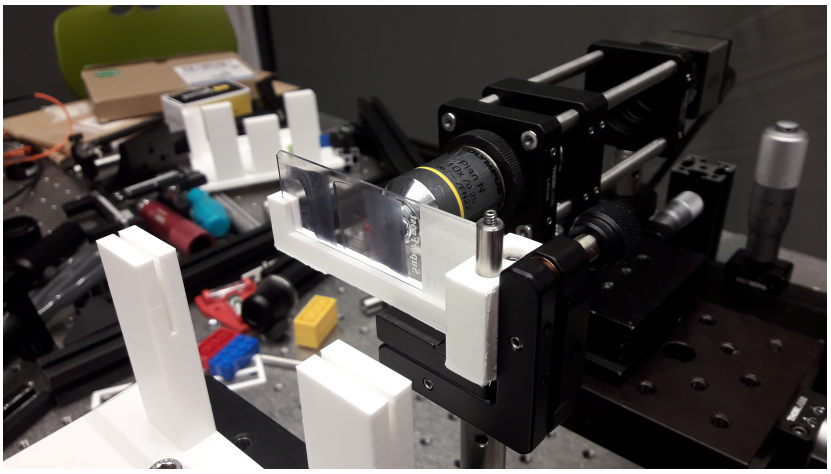

Figure 5-5: 3D printed sample holder attached to a kinematic frame

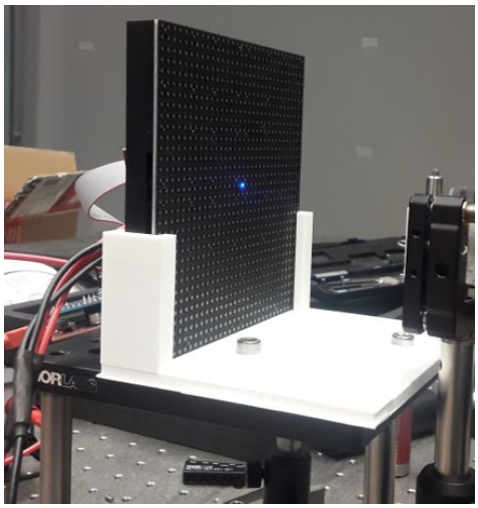

Figure 5-4: 3D printed LED holder

Alignment

To align the system, the spectrum of an image under normal illumination was used. When it is misaligned, the spectrum of the image will show 2 circles with the displacement depending on the degree of misalignment fig. 5-6a. By adjusting the LED array alignment, these circles will merge into one single circle at the center of the spectrum fig. 5-6b.

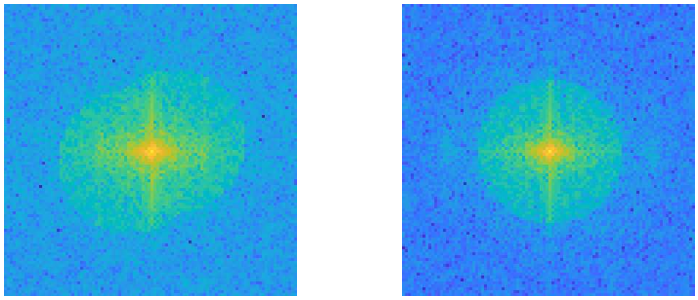

(a) **(b)**

Figure 5-6: (a) Spectrum of image under normal illumination when misaligned; (b) Spectrum of image under normal illumination when aligned

The alignment was then verified by looking at LEDs close to the NA of the objective as the images of these LEDs are surrounded show a dark edge corresponding to the light source being partially blocked by the aperture of the microscope section 5-1-1. Categorization of one of these images as a full dark- or bright field image, indicated that system was off and further adjustments were made to balance dark and bright fields in all images.

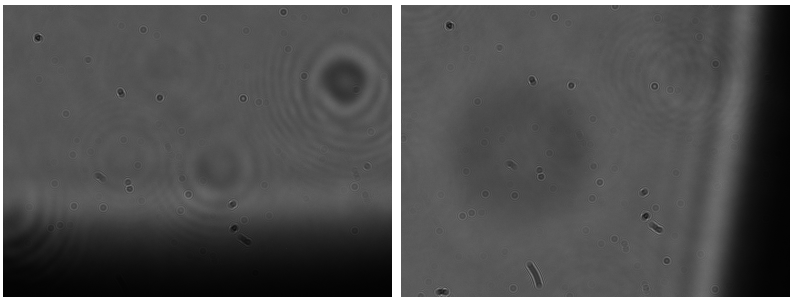

(a) (b)

Figure 5-7: Images of the light source partially blocked by the objectives aperture. This was used to check the first alignment procedure.

5-1-2 Image Acquisition

The sampling sequence used is the same described in chapter 4, starting at the center LED and spiraling outward. An exposure time of 1000ms was chosen to ensure the dark-field images would be contain enough spatial information. To improve the signal to noise ratio (SNR) of the images, the image was averaged 100 times resulting in an SNR decrease by a factor of 10.

5-1-3 Image Preprocessing

Before images were fed to the Fourier Ptychographic algorithm, several preprocessing steps were conducted to improve the quality of the data. This was especially required for the darkfield images as these contained low signal to noise ratio [57].

Darkfield Subtraction

To remove the dark current noise, a dark image I_D taken without LED illumination was subtracted from the darkfield image. First, the weighting α is determined by choosing multiple sections S_p:

$$\alpha_i = \frac{\left\langle \sum_{x,y \in S_p} I_i I_D \right\rangle}{\left\langle \sum_{x,y \in S_p} I_D^2 \right\rangle} \tag{5-1}$$

Then the i-th darkfield image is update according to:

$$I_i^u = I_i - \alpha I_D \tag{5-2}$$

Thresholding

After the darkfield subtraction, thresholding is applied to the darkfield images. The average value of the sections S_p determines the threshold value T_i. All values in the image under this threshold value are then set to 0.

Image Segmentation

As discussed in section 4-4, choosing an appropriate reconstruction size is required to minimize the effects of partially coherent illumination. Therefore, the image was divided in smaller segments of 50×50 pixels fig. 5-8b, which could then independently be reconstructed.

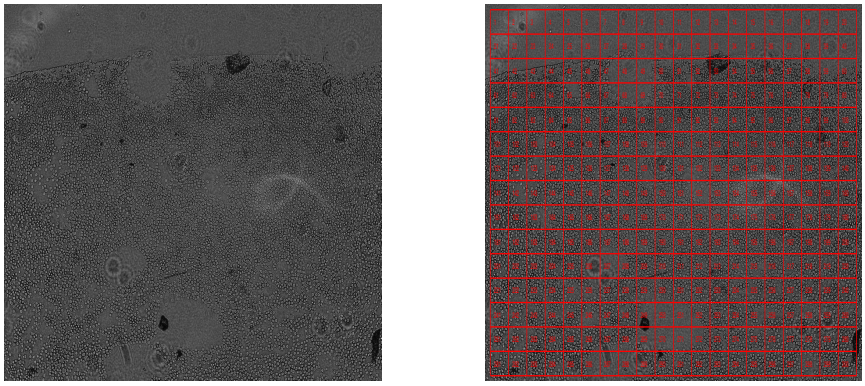

(a) **(b)**

Figure 5-8: (a)Full field of view image obtained by the microscope; (b) Possible segmentes for reconstruction

5-1-4 Reconstruction Algorithm

The reconstruction algorithm used the embedded pupil recovery algorithm as discussed in section 3-4. This increases robustness by retrieving the complex field and the pupil aberrations at the same time.

5-2 Debugging process

Before the system described above, there were several prior iterations of the Fourier Ptychographic setup. The first setup fig. 5-9, based on a design described in an introductory paper on Fourier Ptychography [7], consisted of a single rod holding the optical system attached to a pillar with 3 translating stages. This gave the optical system 3 degrees of freedom for focusing and alignment. The sample was clamped in a mount, allowing the sample to be translated in 2 directions. The LED array was set on a stage built of LEGO. With this setup the most notable issue was constant misalignment due to the inability to tightly fix the LED array.

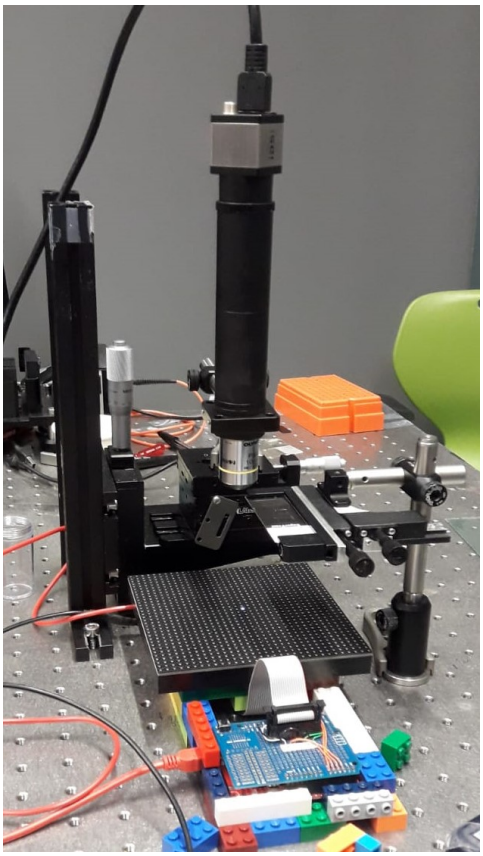

Figure 5-9: First iteration of the Fourier Ptychographic setup, with LEGO stage (sub optimally) holding the LED array

The second iteration fig. 5-10 solved this problem by clamping the LED array and flipping the system on its side. However, this system iteration suffered from the sample mount slowly drifting due to gravity. In addition the optical system required an extra support at the camera. This caused issues with alignment as every time the system had to be aligned the camera support also had to be realigned.

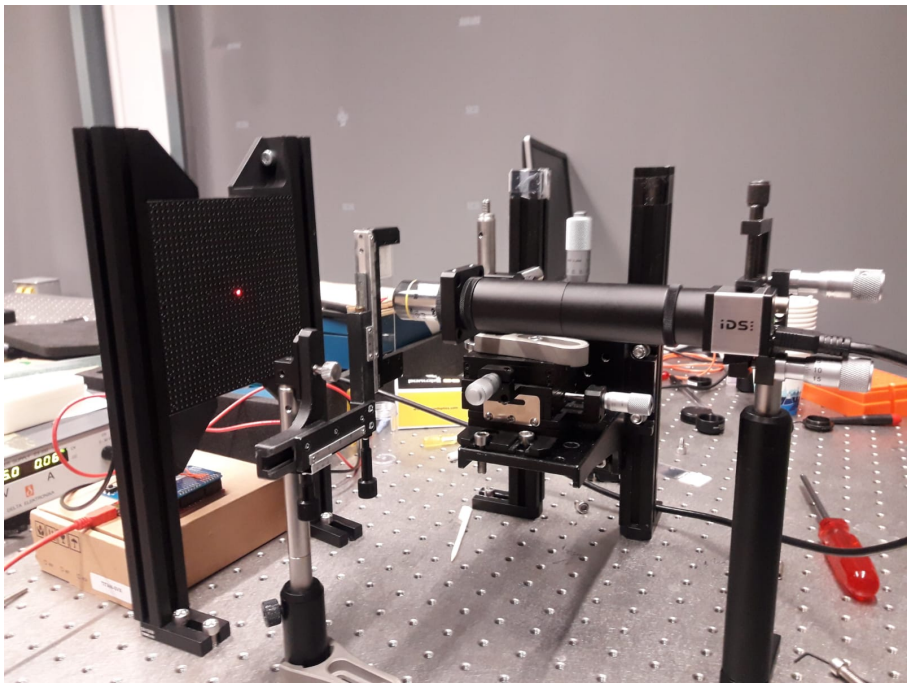

Figure 5-10: Second iteration of the Fourier Ptychographic setup. Clamped in camera caused issues with alignment and focusing

To solve these issues, the architecture of the first system was reused but the LED array was screwed onto rods and translation and rotation was prevented by fixating it using two post holders. Limiting issues in this setup were rotation of the optical system around the axis of the rod, which caused misalignment. In addition, the sample clamp had a lot of mechanical play making it challenging to have the whole sample in focus due to tip and tilt.

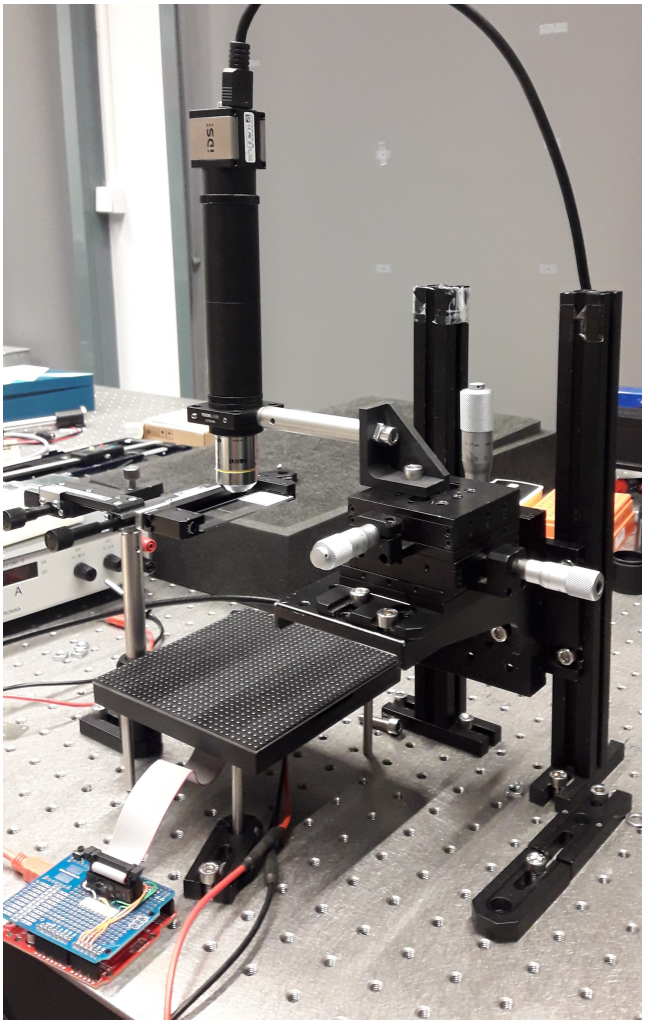

Figure 5-11: Third iteration of the Fourier Ptychographic setup. The rod holding the optical system allowed for rotation around its axis, causing a tip aberration in the image, together with the sample clamp having too much mechanical play to allow full field focus

The issue of rotation around the rod was solved by employing a cage for the optical components, the size of the optical system was reduced and allowed it to be mounted directly onto the translating stages, removing issues caused by the rod fig. 5-12. The play in the sample clamp was removed by designing and 3D printed and attached to a kinematic mount, removing the mechanical play and giving control over the tip and tilt of the sample fig. 5-5.

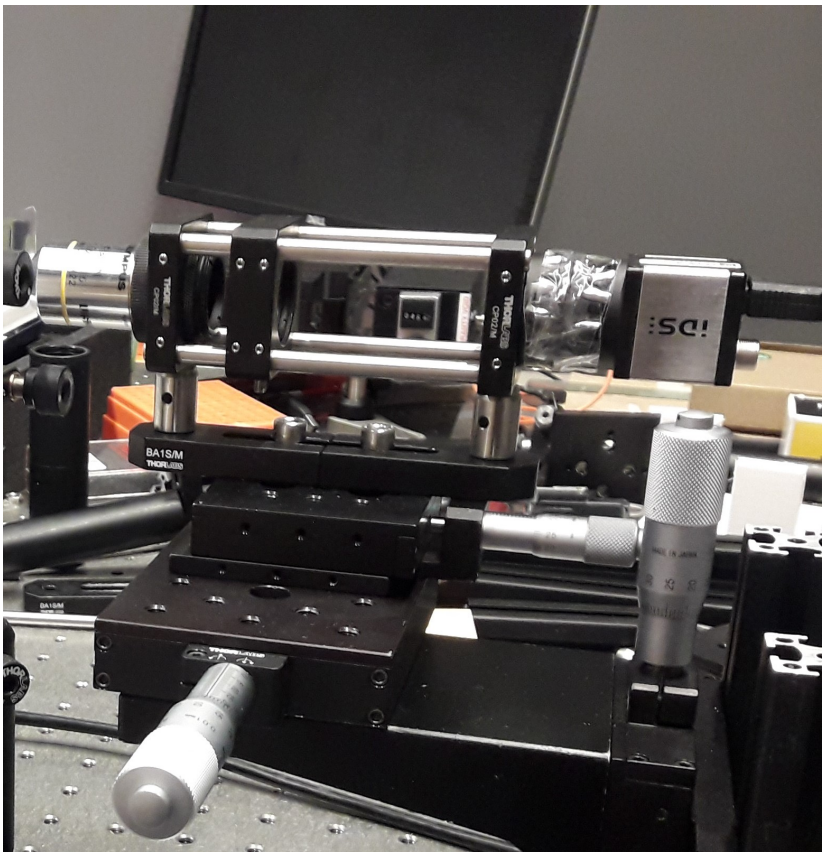

Figure 5-12: Cage system mounted directly onto translating stages

Chapter 6

Results

fig. 6-1, shows a segment that is reconstructed with the Fourier Ptychographic algorithm. In fig. 6-2 the reconstruction of a Giemsa stained red blood smear is shown. The reconstructed amplitude for 49 images shows clear improvement of the morphology of the red blood cells. The phase clearly shows the edges between the blood cells and the background and bumps correspond to the indents in the blood cells.
However, when more images are added to the reconstructions details in both the amplitude and phase are blurred out figs. 6-2e and 6-2f.

Figure 6-1: Low resolution image segment under normal illumination and $\gamma = 2.2$

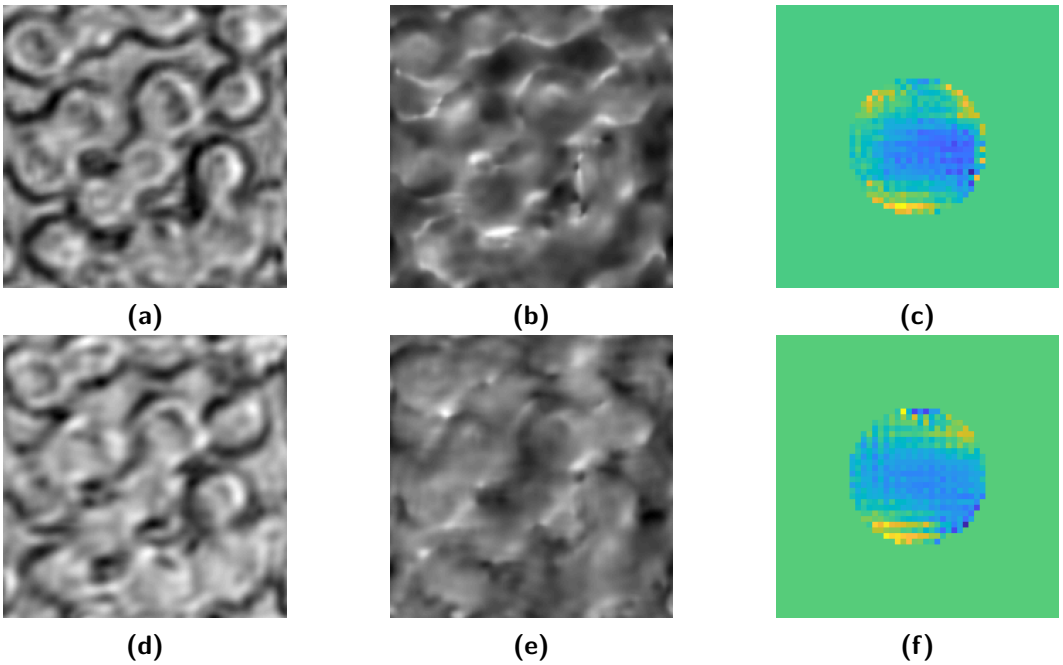

Figure 6-2: Reconstructions for $\gamma = 2.2$:(a) Amplitude reconstruction for 49 images; (b) Phase reconstruction for 49 images; (c) Reconstructed pupil aberration for 49 images;(d) Amplitude reconstruction for 71 images; (e) Phase reconstruction for 71 images; (f) Reconstructed pupil aberration for 71 images

However, the camera control through MATLAB had a predefined (fixed) gamma setting of $\gamma = 2.2$. To check whether the deteriorating effects were influenced by the gamma setting, images were collected manually through the uEye cockpit. All the settings discussed in section 5-1 where copied and the gamma characteristic was set to 1. The manual collection of images did have as consequence that the averaging step in the image preprocessing could not be applied. The segment which was reconstructed is shown in fig. 6-3.

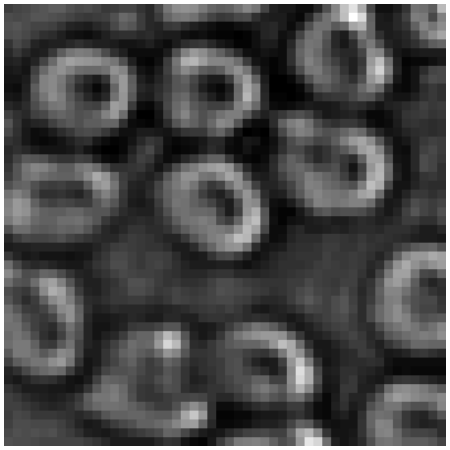

Figure 6-3: Original low resolution image segment under normal illumination and $\gamma = 1$

The results of the reconstruction using 49 images is shown in fig. 6-4. The amplitude recon-

struction fig. 6-4a again shows a noticeable increase in distinction of characteristic traits of the blood cells. The phase fig. 6-4b, clearly shows the borders of the red blood cells and the indent of the blood cell is much more distinct than in fig. 6-2b. However, when more images are added the reconstruction quality reduces again, with the features blurring out figs. 6-4d and 6-4e.

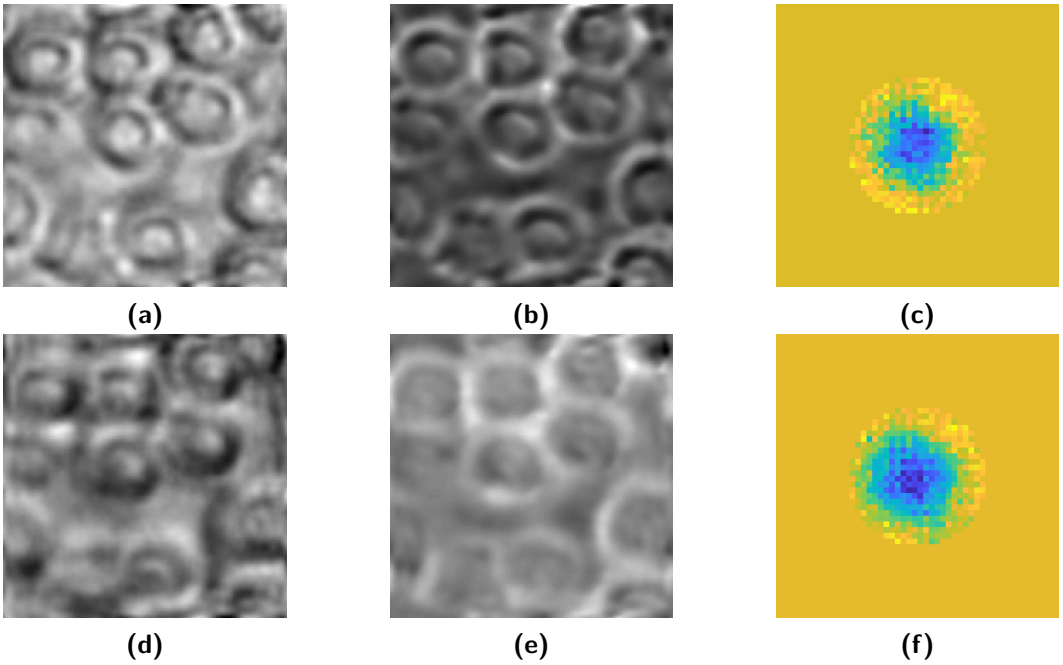

Figure 6-4: Reconstructions for $\gamma = 1$:(a) Amplitude reconstruction for 49 images; (b) Phase reconstruction for 49 images; (c) Reconstructed pupil aberration for 49 images;(d) Amplitude reconstruction for 71 images; (e) Phase reconstruction for 71 images; (f) Reconstructed pupil aberration for 71 images

Chapter 7

Discussion

Our Fourier Ptychographic microscope can effectively increase the resolution of the optical system and acquire the phase information in the reconstruction process. However, our experimental setup revealed that reconstruction quality decreased with an increasing number of bright field images and that quality further suffered from addition of dark field images. No immediately apparent causality between the observed behavior and one of more of the specific system aspects which determine reconstruction quality could be identified.

Before the system can be further developed for malaria diagnosis, the cause of this erratic behavior needs to be identified and corrected. A series of simulation studies were defined, developed and implemented to help ruling-in or ruling-out potential sources of error. These studies revealed that:

1. For reconstruction using only bright field images, a bit-depth of 10 is required to achieve a stable reconstruction error. This indicated that the camera bit-depth used in our system should be sufficient for bright field image reconstruction;
2. Effects of intensity drop-off were negligible for bright-field images, indicating that effects of intensity-fall are not the main cause of the deterioration in the physical setup;
3. By constraining reconstruction patches to the coherent patch size and excluding LEDs with illumination angles close to the objectives NA, partial coherence was also exempted;
4. A non-linear camera response was excluded to be the root-cause, as manually collecting images with gamma set to 1 resulted in similar behavior to images with a gamma of 2.2;

Remaining potential error sources are LED-array misalignment, degree of aberration and defocus and sensor signal to noise ratio. These factors have not yet been thoroughly investigated, however the current alignment method still allows for large errors and the calibration

algorithm [43], while working in simulations, it does not perform well with our experimental data. A more in-depth analysis of these factors is needed to rule them in- or out as root-cause for the deteriorating reconstruction quality in the current system.

The university of Glasgow are the leading research institute in the development of low-cost Fourier Ptychographic devices. They have recently reported the development of a low-cost Fourier Ptychographic microscope with the ability to image at a resolution of 0.55 NA [58]. Access to their system would accelerate the development of a working setup, and allow more valuable time and effort to be invested in development of the application for stainless malaria detection based on reconstructed phase information, and in field testing. Therefore, for continuation of this project, a close collaboration with this group is recommended.

Chapter 8

Conclusions

Despite significant progress made through the realization of a test setup and the development of accompanying algorithms, the development of a low-cost Fourier Ptychographic device for detection of malaria has not yet been completed.

It was demonstrated that the system can successfully increase the resolution and reconstruct the phase information of the sample under observation. However, in its current state, an unidentified source of error limits the performance of the system as deteriorating effects take place as the number of images increases.

Sensitivity analyses of bit-depth, intensity fall- off and partial coherence allowed these factors to be excluded as the root-cause for reconstruction degradation. Similar studies are required to analyze sensitivity to LED array misalignment and various potential sources of sensor noise.

A collaboration with the university of Glasgow is recommended to speed up development of properly working test setups and the design of a low-cost device. This would allow emphasis on development of a specific system for malaria detection using reconstructed phase information, user inspired design and in-field testing.

Appendix A

Supplementary information

A-1 Image formation Fourier Ptychography

Assume an object in the sample plane with transmission function $O(x, y)$ with $\mathcal{O}(k_x, k_y) = \mathcal{F}(O(x, y))$ its Fourier transform, $\mathcal{F}$ the Fourier transform operator and $\mathcal{F}^{-1}$ its inverse. An LED-array consisting of $N \times N$ LED's, is placed with its center LED on the optical axis of the microscope. The coordinate of the i-th LED in the array is donated by $(x_{LED,i}, y_{LED,i}) \in \{-N/2, \ldots, N/2\} \times \{-N/2, \ldots, N/2\}$ and its spatial position $(X_{LED,i}, Y_{LED,i}) = (x_{LED,i}, y_{LED,i})\Delta_{LED}$, with Δ_{LED} the pitch of the LEDs on the array.

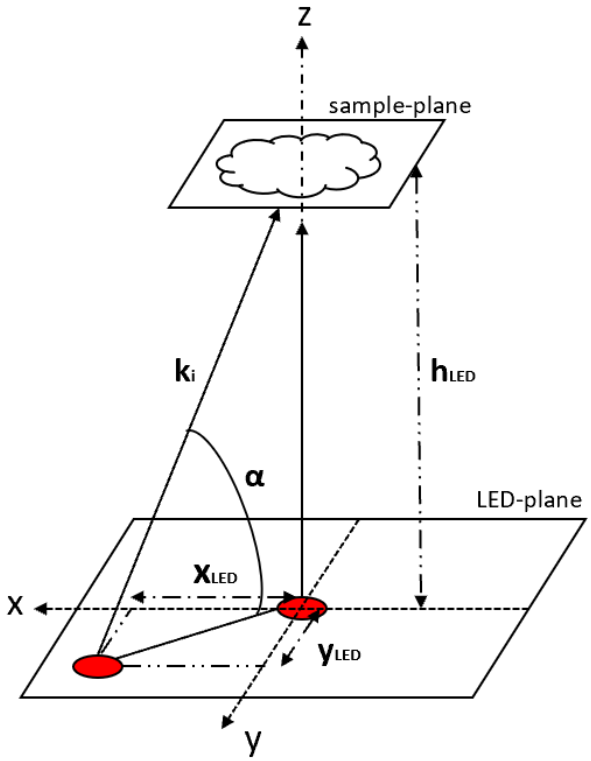

Figure A-1: Geometry of the LED array

When placing the sample in the far field of the LED-array [1], the incident wave can be assumed to be a plane wave, with direction $\hat{\mathbf{k}}_\mathbf{i}$:

$$\hat{\mathbf{k}}_\mathbf{i} = \frac{(X_{LED,i}, Y_{LED,i}, h_{LED})}{\sqrt{X_{LED,i}^2 + Y_{LED,i}^2 + h_{LED}^2}} \tag{A-1}$$

For an LED illumination with wavelength λ, the wave vector of the incident wave $\mathbf{k_i} = \hat{\mathbf{k}}_\mathbf{i} 2\pi/\lambda = \hat{\mathbf{k}}_\mathbf{i} k$. The field scattered by the sample $G(x, y, z)$ is a superposition of its transmis-

[1] One can approximate the distance required for the far field by requiring the distance to be larger than the Frauhnhofer distance: $d_f = 2\frac{D_{LED}}{\lambda}$ with D_{LED} the diameter of the active area of the LED and additional constraints that $d_f >> D_{LED}$ and $d_f >> \lambda$

sion function and the incident wave:

$$G_i(x,y,z) = O(x,y)e^{j(\mathbf{k_i}\cdot\mathbf{r})} \tag{A-2}$$

This expression can be simplified by assuming $z = 0$ in the sample plane, eq. (A-2) then becomes:

$$G_i(x,y,0) = O(x,y)e^{j(k_{x,i}x+k_{y,i}y)} \tag{A-3}$$

If the sample is placed in the focal plane of the objective lens, the field behind the lens can be assumed to be the Fourier Transform of the field in the focal plane. By applying the Fourier shift theorem and limiting the field by the pupil of the objective $\mathcal{P}(k_x,k_y)$, the field in the microscope $\mathcal{M}$ is:

$$\mathcal{M}_i(k_x,k_y,z) = \mathcal{F}(O(x,y)e^{k_{x,i}x+k_{y,i}y})\mathcal{P}(k_x,k_y) = \mathcal{O}(k_x-k_{x,i},k_y-k_{y,i})\mathcal{P}(k_x,k_y) \tag{A-4}$$

$$\mathcal{P}(k_x,k_y) = \begin{cases} 1, & \text{if } k_x^2+k_y^2 \leq kNA_{obj} \\ 0, & \text{if } k_x^2+k_y^2 > kNA_{obj} \end{cases} \tag{A-5}$$

This field is focused on the focal plane of the ocular lens, where the image sensor is placed. As image sensors are only able to gather intensity information, the image corresponding to the i-th LED is:

$$I_i(x,y) = |\mathcal{F}^{-1}(\mathcal{O}(k_x-k_{x,i},k_y-k_{y,i})\mathcal{P}(k_x,k_y))|^2 \tag{A-6}$$

A-2 Vectorization of Phase Retrieval problem

The image formation operator introduced in section 3-2-2 is a sequence of other operators. The first is a down-sampling operator $\mathbf{D} \in \mathbb{R}^{m^2\times n^2}$ to resize the high resolution spectrum into the size of the lower dimensional image. The second is the pupil operator $\mathbf{P} \in \mathbb{R}^{m^2\times m^2}$ which applies a low pass filter on the down-sampled spectrum. Finally, the Fourier transform and its inverse are defined $\mathbf{F}, \mathbf{F^{-1}} \in \mathbb{C}^{m^2\times m^2}$. Image formation of $\mathbf{A}$ is then formulated as:

$$\mathbf{A} = \mathbf{F^{-1}PDF} \tag{A-7}$$

A-3 Gradient Phase Retrieval problem

The objective which is minimized during phase retrieval $E(\mathbf{x})$, with:

$$E(\mathbf{x}) = |||\mathbf{Ax}|^2 - \mathbf{b}||_F^2 = ||(\mathbf{Ax})^* \circ \mathbf{Ax} - \mathbf{b}||_F^2 \tag{A-8}$$

is a non-holomorphic function (real valued function with complex variables), and as a result its derivative with respect to the complex variables is not defined. This can be circumvented by using Writinger derivatives [35] to define the gradient of $E(\mathbf{x})$. In this case, $E(\mathbf{x})$ is defined as the gradient with respect to the complex conjugate of the complex variable $\nabla E(\mathbf{x}) = 2\nabla_{x^*}E(\mathbf{x})$ [36]:

$$\nabla_{\mathbf{x}^*}E(\mathbf{x}) = \mathbf{A}^H((|\mathbf{Ax}|^{\circ 2} - \mathbf{b}) \cdot \mathbf{Ax}) \tag{A-9}$$

$$= -\mathbf{A}^H(\mathbf{b} \circ \frac{\mathbf{Ax}}{|\mathbf{Ax}|} - \mathbf{Ax}) \tag{A-10}$$

With $(\cdot)^{\circ(\cdot)}$ the Hadaman power and $(\cdot) \circ (\cdot)$ Hadaman multiplication.
Notice that $\mathbf{b} \circ \frac{\mathbf{Ax}}{|\mathbf{Ax}|}$ of eq. (A-9) is the same as eq. (3-6) in the Gerchberg-Saxton algorithm, and $\mathbf{Ax}$ corresponds to the pupil projection step eq. (3-5). By rewriting eq. (A-10) one can show that for a unit step size $\alpha = 1$, **??** is the same as the Alternating projections update step, which demonstrates that the two algorithms are basically the same [9].

A-4 Derivatives LED array displacements

To determine robust boundary conditions for LED exclusion, the uncertainty of the positioning of the LED array should be taken into account as this has effect on the positions of the sampling point in the spectrum of the object. The possible displacements are defined as:

- X-translation (δ_x) and Y- translation (δ_y);
- Array, sample distance error (δ_z);
- Rotation around optical axis (θ_z);
- Tip (θ_x) and Tilt (θ_y) of array;

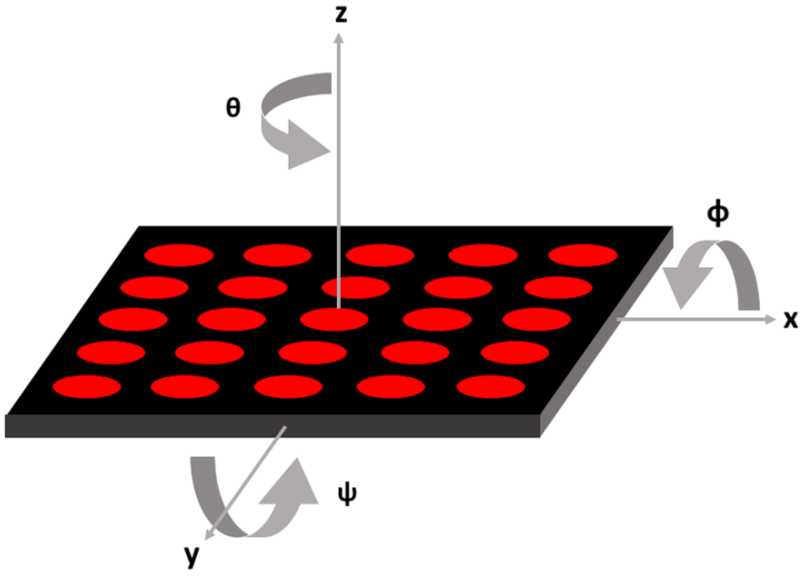

Figure A-2: All possible rotations and translation of the LED array

Every position of the LED-array can then be described using the 3-rotations $(\theta_x, \theta_y, \theta_z)$ and a translation $(\delta_x, \delta_y, \delta_z)$ described by:

$$\tilde{\mathbf{r}}_i = \mathcal{R}_x(\theta_x)\mathcal{R}_y(\theta_y)\mathcal{R}_z(\theta_z)\mathbf{r}_i + \mathcal{T}(\delta_x, \delta_y, \delta_z) \tag{A-11}$$

With:

$$\mathcal{R}_x(\theta_x) = \begin{bmatrix} 1 & 0 & 0 \\ 0 & \cos(\theta_x) & -\sin(\theta_x) \\ 0 & \sin(\theta_x) & \cos(\theta_x) \end{bmatrix}, \mathcal{R}_y(\theta_y) = \begin{bmatrix} \cos(\theta_y) & 0 & \sin(\theta_y) \\ 0 & 1 & 0 \\ -\sin(\theta_y) & 0 & \cos(\theta_y) \end{bmatrix}$$

$$\mathcal{R}_z(\theta_z) = \begin{bmatrix} \cos(\theta_z) & -\sin(\theta_z) & 0 \\ \sin(\theta_z) & \cos(\theta_z) & 0 \\ 0 & 0 & 1 \end{bmatrix}, \mathcal{T}_z(\delta_x, \delta_y, \delta_z) = \begin{bmatrix} \delta_x \\ \delta_y \\ \delta_z \end{bmatrix}$$

Donate the perturbed incident wave vector as $\tilde{\mathbf{k}}_i$, with:

$$\tilde{\mathbf{k}}_i = \begin{bmatrix} \tilde{k}_i^x & \tilde{k}_i^y & \tilde{k}_i^z \end{bmatrix}^T = k_0 \frac{\tilde{\mathbf{r}}_i}{||\tilde{\mathbf{r}}_i||_2} \tag{A-12}$$

However, since the $z = 0$ is defined in the sample plane, only the behavior of the x- and y-component are of interest in analysis of the movement of the sample points. Therefor, the z-component will be excluded from all derivations.

Translation

The x- and y- components of perturbed wave vector for a translation along the x-axis are described as followed:

$$\tilde{k}_i^x = k_0 \frac{x_i}{\sqrt{x_i^2 + y_i^2 + h^2}} \tag{A-13}$$

$$\tilde{k}_i^y = k_0 \frac{y_i}{\sqrt{x_i^2 + y_i^2 + h^2}} \tag{A-14}$$

The gradient of these points with respect to x_i is then:

$$\nabla_x = \begin{bmatrix} \frac{\partial \tilde{k}_i^x}{\partial x_i} & \frac{\partial \tilde{k}_i^y}{\partial x_i} \end{bmatrix}^T = \frac{-k_0}{(x_i^2 + y_i^2 + h_L^2)^{3/2}} \begin{bmatrix} y_i^2 + h_L^2 \\ -x_i y_i \end{bmatrix} \tag{A-15}$$

Similarly for a translation along the y-axis:

$$\nabla_y = \begin{bmatrix} \frac{\partial \tilde{k}_i^x}{\partial y_i} & \frac{\partial \tilde{k}_i^y}{\partial y_i} \end{bmatrix}^T = \frac{-k_0}{(x_i^2 + y_i^2 + h_L^2)^{3/2}} \begin{bmatrix} -x_i y_i \\ x_i^2 + h_L^2 \end{bmatrix} \tag{A-16}$$

Height

The x- and y-components of the wave vector perturbed in the-direction is denoted by:

$$\tilde{k}_i^x = k_0 \frac{x_i}{\sqrt(x_i^2 + y_i^2 + h^2} \tag{A-17}$$

$$\tilde{k}_i^y = k_0 \frac{y_i}{\sqrt(x_i^2 + y_i^2 + h^2} \tag{A-18}$$

The gradient with respect to height misalignment then becomes:

$$\begin{aligned}\nabla_z &= \begin{bmatrix}\frac{\partial \tilde{k}_i^x}{\partial h} & \frac{\partial \tilde{k}_i^y}{\partial h}\end{bmatrix}^T \\ &= \frac{k_0}{(x_i^2+y_i^2+h^2)^{3/2}}\begin{bmatrix}x_i h \\ y_i h\end{bmatrix}\end{aligned} \tag{A-19}$$

Rotation around Optical axis

$$\nabla_\theta = \begin{bmatrix}\frac{\partial \tilde{k}_i^x}{\partial \theta} & \frac{\partial \tilde{k}_i^y}{\partial \theta}\end{bmatrix}^T = \frac{k_0}{\sqrt{x_i^2+y_i^2+h_L^2}}\begin{bmatrix}y_i \\ x_i\end{bmatrix} \tag{A-20}$$

Tip and Tilt

To described the effect of tip or tilt of the array on the sampling locations in the samples spectral domain, the taylor approximation can be taken with respect to ϕ or ψ.

$$\tilde{k}_i^x = k_0 \frac{x_i}{\sqrt{x_i^2+y_i^2+h^2}} \tag{A-21}$$

$$\tilde{k}_i^y = k_0 \frac{y_i \cos(\theta_x) + h\sin(\theta_x)}{\sqrt{x_i^2+y_i^2+h^2}} \tag{A-22}$$

With ∇_ϕ:

$$\nabla_\psi = \begin{bmatrix}\frac{\partial \tilde{k}_i^x}{\partial \psi} & \frac{\partial \tilde{k}_i^y}{\partial \psi}\end{bmatrix}^T = \frac{k_0}{\sqrt{1+\frac{x_i^2+y_i^2}{h_L^2}}}\begin{bmatrix}1 \\ 0\end{bmatrix} \tag{A-23}$$

$$\nabla_\phi = \begin{bmatrix}\frac{\partial \tilde{k}_i^x}{\partial \phi} & \frac{\partial \tilde{k}_i^y}{\partial \phi}\end{bmatrix}^T = \frac{k_0}{\sqrt{1+\frac{x_i^2+y_i^2}{h_L^2}}}\begin{bmatrix}0 \\ 1\end{bmatrix} \tag{A-24}$$

A-5 Reconstruction Speed

Depending on the segment size chosen, reconstruction of the full field of view can be very time consuming. Results of a brief analysis of the time needed to complete a reconstruction using 441 images and various segment sizes are shown in fig. A-3a. This is done on 2 computers each with different processing power.[2] For computer 1, the reconstruction time scales quadratically

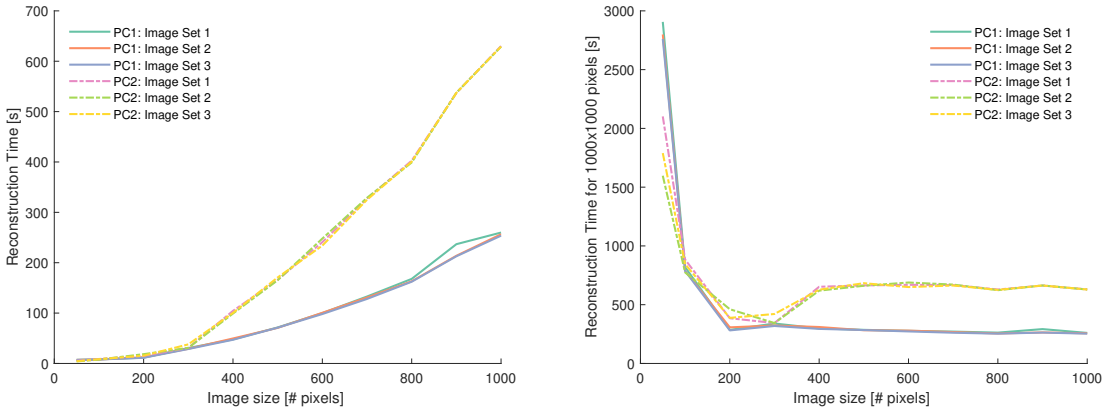

Figure A-3: (a) Reconstruction times for various image size;(b) Time to reconstruct a patch of 1000 × 1000 pixels based on chosen image size

with the reconstruction size fig. A-3a. Both computers perform the reconstructions equally fast up to a size of 300 × 300 pixels, beyond which the reconstruction time separate. To determine how long it would take the reconstruct the entire image, a supposed size of 1000 × 1000 was chosen. The total computation time is obtained by multiplying the single segment computation time with the number of segments comprising the full image. The number of patches (N_p)of size $m \times m$ that have to be reconstructed, for a square sensor of size $n \times n$ is described by:

$$N_p = \left(\frac{n}{m}\right)^2 \tag{A-25}$$

The total reconstruction time for both computers graphed in fig. A-3b. The optimal reconstruction size is found to be around 200 × 200 pixels appears to be independent of the computational efficiency of the processor.

This program used sequential programming. Increased speeds can be obtained by using parallel processing, which is supported by many computers allowing multiple patches to be processed simultaneously.

[2]Computer 1 processor: Intel(R) Core(TM) i7-5600CPU, 2Core(s), 4 logical processors
Computer 2 processor: 6 × Intel(R) Xeon(R) Gold 6148 CPU, 1Core(s), 1 logical processor

Appendix B

Submissions Photonics West

250 word Abstract for Photonics West

Fourier Ptychography is a computational imaging technique able to decouple high resolution from wide field of view, bypassing the diffraction limit of the microscope. Its capability to extract quantitative phase information from a sample makes it potentially applicable for label free imaging of malaria parasites. Since it does not rely on high precision mechanics or fluorescent imaging it is of practical interest for implementation in low scale devices. Despite its gains, realizing a functional low-cost set-up use-able at the theoretical limits is challenging due to many factors causing discrepancies between theory and practice. LED-array misalignment, optical system aberrations and use of partial coherent sources are common issues which have been addressed with calibration algorithms. Physical interpretation of how these factors influence the algorithm and cause mismatches between theory and practice has had little attention so far. This work provides an in-depth discussion based on simulation results on quantization noise of the camera, influence of intensity drop-off due to angled illumination and effect of the partial coherence of the source. From obtained results, we prescribe optimal design configuration based on the correlation between the NA of the objectives and the illumination pattern of the LED array. This will mitigate the effect of partial coherence and improve the convergence of the reconstruction algorithms. These insights will enable the development of a more efficient reconstruction algorithms and the realization of a potentially low-cost robust system design.

100 word abstract

Fourier Ptychography is a computational imaging technique able to decouple high resolution from wide field of view, bypassing the diffraction limit of the microscope. LED-array misalignment, optical system aberrations and partial coherent sources are common issues which have been addressed with calibration algorithms. Physical interpretation of how these factors influence the algorithm and cause mismatches between theory and practice has had little attention. We prescribe optimal design configuration based on the correlation between the NA of the objectives and the illumination pattern of the LED array, mitigating the effect of partial coherence and improving the convergence of the reconstruction algorithms.

Appendix C

Conference paper: Photonics West

Note: The paper added is an early draft of the conference paper for Photonics West, the final version will be subjected to changes.

Towards a robust, low cost Fourier Ptychographic device

Alexander Heemels[a], Temitope Agbana[a], Sylvania Pereira[a], Jan Carel Diehl[a], Michel Verhaegen[a], and Gleb Vdovin[a]

[a]Technical University Delft, Delft, Netherlands

ABSTRACT

Fourier Ptychography is a computational imaging technique able to decouple high resolution from wide field of view, bypassing the diffraction limit of the microscope. Its capability to extract quantitative phase information from a sample makes it potentially applicable for label free imaging of malaria parasites. Since it does not rely on high precision mechanics or fluorescent imaging it is of practical interest for implementation in low scale devices. Despite its gains, realizing a functional low-cost set-up use-able at the theoretical limits is challenging due to many factors causing discrepancies between theory and practice. LED-array misalignment, optical system aberrations and use of partial coherent sources are common issues which have been addressed with calibration algorithms. Physical interpretation of how these factors influence the algorithm and cause mismatches between theory and practice has had little attention so far. This work provides an in-depth discussion based on simulation results on quantization noise of the camera, influence of intensity drop-off due to angled illumination and effect of the partial coherence of the source. From obtained results, we prescribe optimal design configuration based on the correlation between the NA of the objectives and the illumination pattern of the LED array. This will mitigate the effect of partial coherence and improve the convergence of the reconstruction algorithms. These insights will enable the development of a more efficient reconstruction algorithms and the realization of a potentially low-cost robust system design.

Keywords: Fourier Ptychography, Partial Coherence, Coherence, Robustness

1. INTRODUCTION

Fourier Ptychography[1] is based on developments in synthetic aperture techniques[2] and phase retrieval algorithms[3,4] and enables increasing the microscopes SBP by combining incident illumination variation and computational techniques. It is based on the assumption of coherent imaging, which allows images to be expressed as a convolution operation of the object with the impulse response function of the optical system.[5] This assumption does not fully apply when imaging with a Light Emitting Diode (LED). LEDs are quasi-monochromatic light sources and their wide application in fourier ptychography implies that image formation is better described using complex partial coherent model. Based on the assumption that incoherent sources gain coherence through propagation[6] and applying Van Cittert Zernike Theorem,[7] a domain at any distance from the source can be determined. Given the radius of the extended light source ρ_s, it's mean wavelength $\bar{\lambda}$ and the sample to source distance h_s, the radius of the coherent patch R_{coh} can be expressed using Van Cittert theorem as:

$$R_{coh} = \frac{0.16\bar{\lambda}h_s}{\rho_s} \tag{1}$$

Increase in source-to-sample distance produces a corresponding increase in the coherent patch size. A fully coherent image reconstruction can therefore be achieved if reconstructed image size is constrained within the coherent patch. Fourier Ptychography is mostly used for low NA optical system with low magnifications and imaging sensor which consist of millions of pixels in a two dimensional grid. Reconstructing a full field of view therefore implies the reconstruction of several hundreds of patches making it computationally time inefficient. In this work, we analyse the impact of partial coherence and the extent to which reconstruction with image sizes

Further author information: (Send correspondence to)
Alexander Heemels.: E-mail: A.N.M.Heemels@tudelft.nl, Telephone: +31 152785305
Temitope E. Agbana.: E-mail: t.e.agbana@tudelft.nl, Telephone: +31 152785305

exceeding the coherent patch size can be done without any significant degradation in reconstruction quality. To realize our goal, we adapt the image formation model to allow generation of partially coherent images. Furthermore, we investigated the effects of extended source and emitting bandwidths and profer solutions for mitigating the negative influence of partial coherence in the reconstruction images.

2. MODEL MODIFICATIONS

Under partial coherent assumptions, the mutual intensity function in the sample plane $J_0(\mathbf{x}_0, \mathbf{x}_0')$ and the system transmission function $K(\mathbf{x}_0, \mathbf{x}_1)$ are used to determine the field J_1 in the imaging plane.

$$J_1(\mathbf{x}_1, \mathbf{x}_1) = I(\mathbf{x}_1) = \iint_{-\infty}^{+\infty} J_0(\mathbf{x}_0, \mathbf{x}_0') K(\mathbf{x}_0, \mathbf{x}_1) K^*(\mathbf{x}_0', \mathbf{x}_1') d\mathbf{x}_0 d\mathbf{x}_0' \tag{2}$$

The mutual intensity function describes the correlation between two points in a field. These points can be described as $U(\mathbf{x}_0)$ and $U(\mathbf{x}_0')$ in the sample plane with:

$$U(\mathbf{x}) = o(\mathbf{x}) e^{j(\mathbf{k}_i \cdot \mathbf{x})} \tag{3}$$

Allowing the mutual intensity in the sample plane to be written as:

$$J(\mathbf{x}_0, \mathbf{x}_0') = \langle U(\mathbf{x}_0) U^*(\mathbf{x}_0') \rangle = \langle o(\mathbf{x}_0) e^{j(\mathbf{k}_i \cdot \mathbf{x}_0)} o^*(\mathbf{x}_0') e^{-j(\mathbf{k}_i \cdot \mathbf{x}_0')} \rangle \tag{4}$$

This expression can be simplified by decomposing the partially coherent field into mutual coherent modes.[8,9] The mutual intensity can therefore be adapted to:

$$J(\mathbf{x}_0, \mathbf{x}_0') = \sum_{m,l} o(\mathbf{x}_0) e^{j(\mathbf{k}_{i,m,l} \cdot \mathbf{x}_0)} (o(\mathbf{x}_0') e^{j(\mathbf{k}_{i,m,l} \cdot \mathbf{x}_0')})^* \tag{5}$$

Two types of modes into which the source can be decomposed are the spatial and spectral modes. The source is decomposed into spatial modes by dividing the partial coherent source into a collection of coherent point sources Fig. 1a. We realized spectral modes in this simulation by visualizing the source as a collection of point sources emitting at different wavelengths within the bandwidth of the quasi-monochromatic source Fig. 1b.

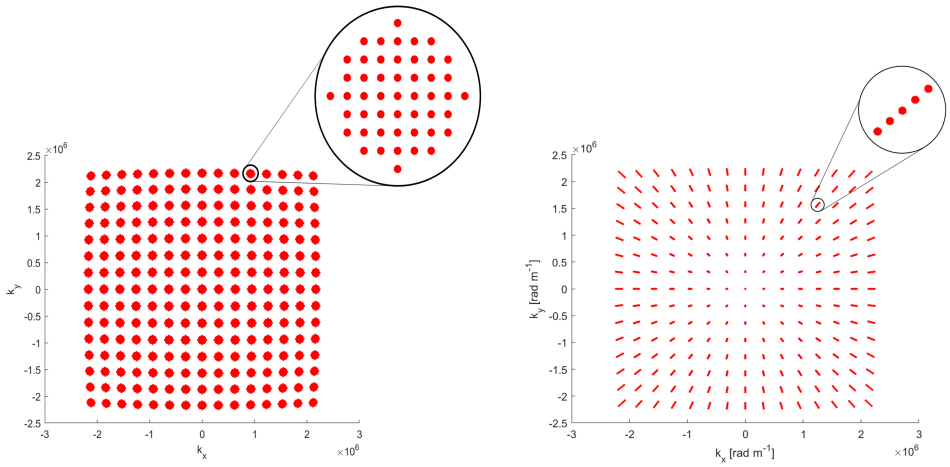

(a) (b)

Figure 1

A combination of the spatial and spectral modes provides all modes related to the quasi-monochromatic source. For future analysis, we denote m and l as the modes corresponding to the extended source and the different wavelengths in the bandwidth respectively.

Under the assumption that the imaging is restricted to the isoplanatic region of the system we can rewrite the systems transmission function as

$$K(\mathbf{x}_0, \mathbf{x}_1) = K(\mathbf{x}_0 - \mathbf{x}_1) \tag{6}$$

By substituting equation (6) back into equation (2) we get:

$$\begin{aligned} I_i(\mathbf{x}_1) &= \iint_{-\infty}^{+\infty} \sum_{m,l} o(\mathbf{x}_0) e^{j(\mathbf{k}_{i,m,l}\cdot\mathbf{x}_0)} (o(\mathbf{x}_0') e^{j(\mathbf{k}_{i,m,l}\cdot\mathbf{x}_0')})^* K(\mathbf{x}_0 - \mathbf{x}_1) K^*(\mathbf{x}_0' - \mathbf{x}_1) d\mathbf{x}_0 d\mathbf{x}_0' \\ &= \sum_{m,l} \iint_{-\infty}^{+\infty} o(\mathbf{x}_0) e^{j(\mathbf{k}_{i,m,l}\cdot\mathbf{x}_0)} K(\mathbf{x}_0 - \mathbf{x}_1) d\mathbf{x}_0 \iint_{-\infty}^{+\infty} \left(o(\mathbf{x}_0') e^{j(\mathbf{k}_{i,m,l}\cdot\mathbf{x}_0')} K(\mathbf{x}_0' - \mathbf{x}_1)\right)^* d\mathbf{x}_0' \end{aligned} \tag{7}$$

Equation (7) corresponds to a multiplication of two convolutions, with each one corresponding to a coherent system response. This can then finally be written as summation of coherent modes:

$$I_i = \sum_{l}^{L} \sum_{m}^{M} |I_{i,m,l}(\mathbf{r})|^2 \tag{8}$$

According to equation (8), partial coherent imaging can be modelled as an incoherent summation of the images produced by the coherent modes making up the partial coherent source. To implement this in simulations, each LED is divided into M coherent sources which are bound to the light emitting surface of the array. The band of emitted wavelengths of the LED $[\bar{\lambda} - \Delta\lambda, \bar{\lambda} + \Delta\lambda]$ is divided into L coherent monochromatic point sources. The partial coherent image is then obtained by making coherent images for all $M \times L$ modes, which are then added together to give the partial coherent image.

3. SIMULATIONS AND RESULTS

Simulations make use of 3 image sets making up the amplitude and phase of the simulated object. This is done to be able to compare global trends in convergence behavior and exclude image dependent behavior and will allow comparison of the different image sets [*].
An offset invariant metric is used to track the spectral error $\mathcal{E}_k$ between reconstruction $\tilde{X}_k$ at iteration k with the original object X.[10]

$$\mathcal{E}_k = \frac{||\mathcal{F}(X) - \alpha\mathcal{F}(\tilde{X}_k)||_2^2}{||\mathcal{F}(X)||_2^2} \tag{9}$$

$$\alpha = \frac{\mathcal{F}(X)\mathcal{F}(\tilde{X}_k)^*}{|\mathcal{F}(\tilde{X}_k)|^2} \tag{10}$$

To investigate the affect of both spatial and spectral modes, the two cases are analyzed separately. By varying the the size of the source form 0-500μm, the area which can be assumed cohrerent in the sample plane decreases. Once the source size exceeds 330μm the reconstruction can no longer be assumed coherent according to Eq. 1. This is confirmed by the simulation results as once the threshold of 330μm is passed an increase in RMSE is observed Fig. 2a. For increasing bandwidths $\Delta\lambda$ =0-100nm, no major increases in RMSE are observed Fig. 2b.

Including darkfield images causes massive jumps in the spectral error even at small bandwidths as shown in

[*]All images were obtained from http://imagecompression.info/test_images/

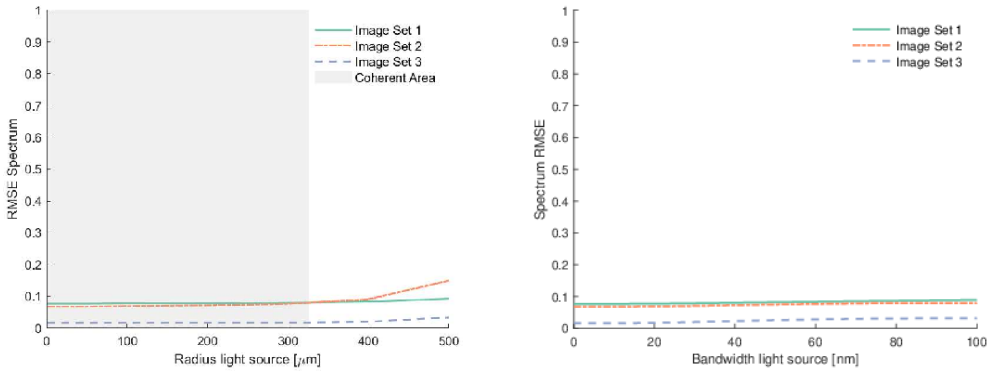

(a) (b)

Figure 2: (a) Final convergence errors for 81 images and all 3 image sets with the radii of the source varying form 0-500μm: Final spectrum convergence values; (b)Final convergence errors for 441 images and all 3 image sets with the radii of the source bandwidth varying form 0-100nm: Final spectrum convergence values;

fig.6b.

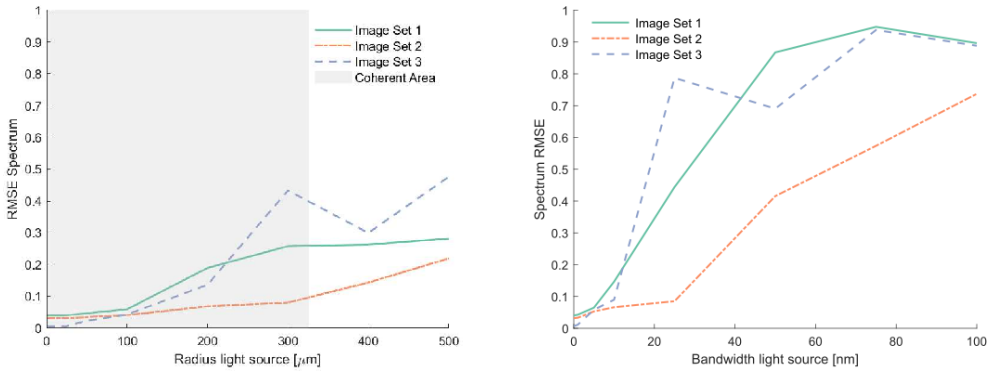

(a) (b)

Figure 3: (a) Final convergence errors for 81 images and all 3 image sets with the radii of the source bandwidth varying form 0-100nm: Final spectrum convergence values; (b)Final convergence errors for 441 images and all 3 image sets with the radii of the source varying form 0-500μm: Final spectrum convergence values

The cause of these errors are identified by tracking the error at the end of each image update step in the Fourier Ptychographic algorithm and looking at which images have a negative contribution to the image reconstruction. All sampling locations of LEDs with images having a negative contribution to the reconstruction are shown in Fig. 4. Notice that the LEDs with a negative impact on the reconstruction are located on the boundary of the objectives numerical aperture, suggesting that LEDs in this location are most sensitive to the effects of the spatial modes.

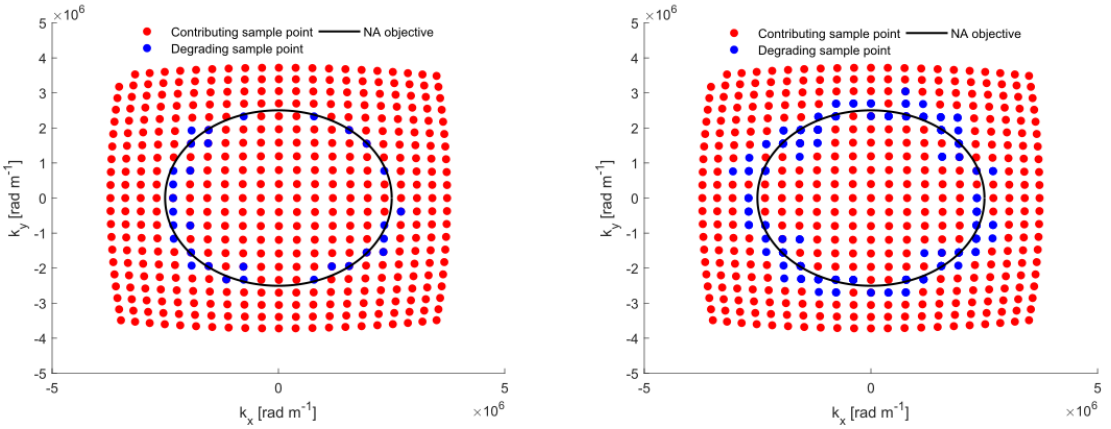

(a) (b)

Figure 4: (a)Visualization of all sampling points which negatively impact the reconstruction for spatial modes, source size 500μm;(b) All LEDs with deteriorating contribution for spectral modes $\Delta\lambda = 100$nm

This increase in RMSE is caused by spatial or spectral modes of the LEDs close to the NA boundary to fall both in- and outside the boundary, causing the corresponding images to be a summation of both bright- and dark field images. As the size or bandwidth of the source increases, so does the spread of the modes in the objects spectral domain therefore changing the ratio of modes which are located in and outside the NA boundary. Because the two types of images have different energy contents, this causes a decrease/increase in the total energy of the composite image.
Removing these LEDs such as in Fig. 5, decreases the reconstruction errors drastically Fig. 6. 5.

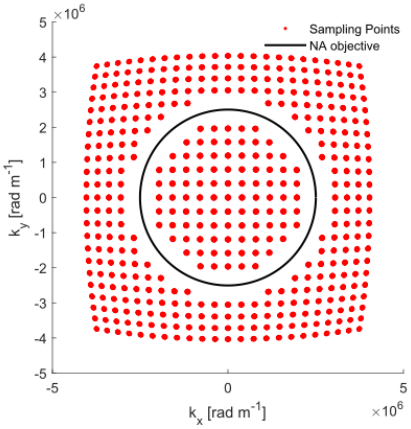

Figure 5: Sampling scenario with spatial modes, with LEDs close to the NA circle left out, avoiding spatial modes falling both in and outside of the NA circle

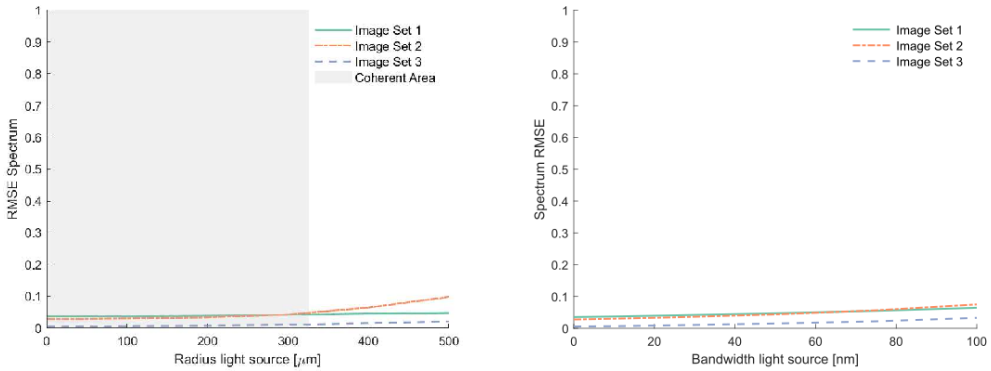

(a) (b)

Figure 6: (a) Final convergence errors for 441 images and all 3 image sets with the radii of the source varying form 0-500μm: Final spectrum convergence values; (b)Final convergence errors for 441 images and all 3 image sets with the radii of the source bandwidth varying form 0-100nm: Final spectrum convergence value

Visual inspection of the reconstruction results for bandwidths of 10, 50 and 100nm, show the degrading effects when the boundary LEDs are included into the reconstruction Fig. 7. When these LEDs are excluded, the reconstruction improves greatly, with deterioration only attributed to the increase in bandwidth Fig.8.

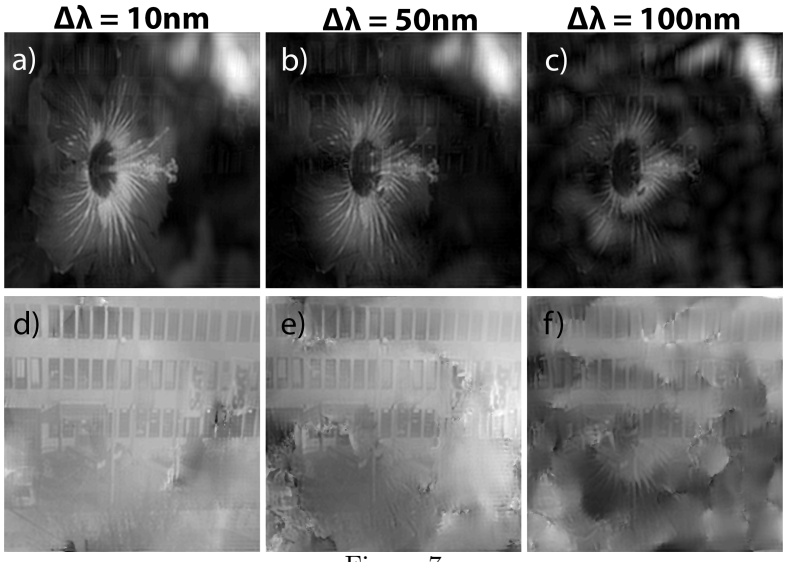

Figure 7

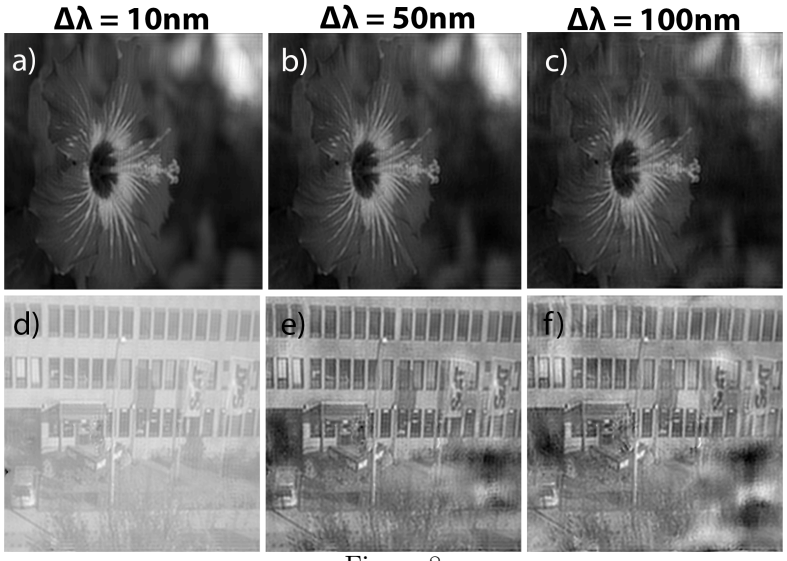

Figure 8

With the above simulation it was demonstrated that when partial coherence is considered, the algorithm becomes very sensitive to the inclusion of LEDs with illumination angles close to the numerical aperture of the objective lens and when these corresponding images of these LEDs are excluded from the reconstruction, the performance is greatly improved.
Therefore, if all LEDs with partial-coherent modes at the boundary of the numerical aperture are excluded, the method's robustness can be greatly improved. It is possible to formulate a closed form expression of an exclusion band $\mathcal{B}$, depending on the spread of the spatial coherent r_ρ modes:

$$r_\rho = k_0 \frac{\rho_s}{\sqrt{\rho_s^2 + h_{LED}^2}} \tag{11}$$

And the spread of the spectral coherent modes r_λ

$$r_\lambda = \Delta_\lambda \nabla_\lambda \tag{12}$$

With $\nabla_{\lambda,i}$ being the gradient of sampling point in the objects spectrum of th i-th LED, which is donated by:

$$\nabla_{\lambda,i} = \frac{\partial \mathbf{k}_i}{\partial \lambda} = -\frac{k}{2\pi}\mathbf{k}_i$$

The size of the final bound is then:

$$\mathcal{B} = k_0 \mathrm{NA}_{obj} \pm \max(r_\lambda \nabla_\lambda + r_\rho) \tag{13}$$

4. CONCLUSIONS

Using simulation studies, it has been shown that the LEDs close to the numerical aperture of the objective lens are very sensitive to the effects of partial coherence. This sensitivity is caused by the spatial and spectral modes of the light source falling both in- and outside the NA of the objective, causing energy mismatches in the composite image compared to the expected coherent case.
However, these degrading effects can be mitigated by removing LEDs with such modes using an exclusion boundary depending on properties of the source.

Bibliography

[1] WHO, "Basic Malaria Microscopy," tech. rep., 2010.

[2] WHO, *World malaria report 2018*. 2018 ed., 2018.

[3] WHO, "Guidelines for the treatment of malaria," no. 3, 2015.

[4] M. L. Wilson, "Malaria rapid diagnostic tests," *Clinical Infectious Diseases*, vol. 54, no. 11, pp. 1637–1641, 2012.

[5] N. Tangpukdee, C. Duangdee, P. Wilairatana, and S. Krudsood, "Malaria diagnosis: A brief review," *Korean Journal of Parasitology*, vol. 47, no. 2, pp. 93–102, 2009.

[6] A. W. Lohmann, R. G. Dorsch, D. Mendlovic, C. Ferreira, and Z. Zalevsky, "Space–bandwidth product of optical signals and systems," *Journal of the Optical Society of America A*, vol. 13, no. 3, p. 470, 1996.

[7] G. Zheng, R. Horstmeyer, and C. Yang, "Wide-field, high-resolution Fourier ptychographic microscopy," *Nature Photonics*, vol. 7, no. 9, pp. 739–745, 2013.

[8] T. M. Turpin, L. H. Gesell, J. Lapides, and C. H. Price, "Theory of the synthetic aperture microscope," no. August 1995, pp. 230–240, 1995.

[9] J. R. Fienup, "Phase retrieval algorithms: a comparison," *Applied Optics*, vol. 21, no. 15, p. 2758, 1982.

[10] Y. Shechtman, Y. C. Eldar, O. Cohen, H. N. Chapman, J. Miao, and M. Segev, "Phase Retrieval with Application to Optical Imaging: A contemporary overview," *IEEE Signal Processing Magazine*, vol. 32, no. 3, pp. 87–109, 2015.

[11] T. E. Agbana, J. C. Diehl, F. Van Pul, S. M. Khan, V. Patlan, M. Verhaegen, and G. Vdovin, "Imaging & identification of malaria parasites using cellphone microscope with a ball lens," *PLoS ONE*, vol. 13, no. 10, pp. 1–13, 2018.

[12] J. Stoevelaar, "A Roadmap For Development of a smart Malaria diagnostic device," 2017.

[13] A. F. Cowman, J. Healer, D. Marapana, and K. Marsh, "Malaria : Biology and Disease," *Cell*, vol. 167, no. 3, pp. 610–624, 2016.

[14] R. Lucius, L.-F. Brigitte, R. P. Lane, P. Robert, C. W. Roberts, and R. k. Grencis, *The Biology of parasites*, vol. 39. 2017.

[15] B. K. Wilson, M. R. Behrend, M. P. Horning, and M. C. Hegg, "Detection of malarial byproduct hemozoin utilizing its unique scattering properties," *Optics Express*, vol. 19, no. 13, p. 12190, 2011.

[16] A. Osei-Bimpong and J. Burthem, *Supplementary Techniques Including Blood Parasite Diagnosis*. Elsevier Ltd., twelfth ed ed., 2016.

[17] K. S. Lee, J. Cox-Singh, and B. Singh, "Morphological features and differential counts of Plasmodium knowlesi parasites in naturally acquired human infections," *Malaria Journal*, vol. 8, no. 1, pp. 1–10, 2009.

[18] B. Singh and C. Daneshvar, "Human infections and detection of plasmodium knowlesi," *Clinical Microbiology Reviews*, vol. 26, no. 2, pp. 165–184, 2013.

[19] WHO, "False-negative RDT results and implications of new reports of P . falciparum histidine-rich protein 2 / 3 gene deletions," *Global Malaria Programme*, pp. 1–11, 2017.

[20] W. H. Organization, "Malaria Microscopy, Quality Assurance Manual,"

[21] S. Cho, S. Kim, Y. Kim, and Y. K. Park, "Optical imaging techniques for the study of malaria," *Trends in Biotechnology*, vol. 30, no. 2, pp. 71–79, 2012.

[22] C. Lawrence and J. A. Olson, "Birefringent hemozoin identifies malaria," *American Journal of Clinical Pathology*, vol. 86, no. 3, pp. 360–363, 1986.

[23] C. W. Pirnstill and G. L. Coté, "Malaria Diagnosis Using a Mobile Phone Polarized Microscope," *Scientific Reports*, vol. 5, pp. 1–13, 2015.

[24] G. A. Jamjoom, "Dark-field microscopy for detection of malaria in unstained blood films," *Journal of Clinical Microbiology*, vol. 17, no. 5, pp. 717–721, 1983.

[25] Y. K. Park, C. Depeursinge, and G. Popescu, "Quantitative phase imaging in biomedicine," *Nature Photonics*, vol. 12, no. 10, pp. 578–589, 2018.

[26] H. Majeed, S. Sridharan, M. Mir, L. Ma, E. Min, W. Jung, and G. Popescu, "Quantitative phase imaging for medical diagnosis," *Journal of Biophotonics*, vol. 10, no. 2, pp. 177–205, 2017.

[27] A. W. Lohmann, R. G. Dorsch, D. Mendlovic, C. Ferreira, and Z. Zalevsky, "Space–bandwidth product of optical signals and systems," *Journal of the Optical Society of America A*, vol. 13, no. 3, p. 470, 1996.

[28] S. Hell, "Far-Field Optical Nanoscopy," *Science*, vol. 316, no. May, pp. 1153–1159, 2007.

[29] A. Ozcan and E. McLeod, "Lensless Imaging and Sensing," *Annual Review of Biomedical Engineering*, vol. 18, no. 1, pp. 77–102, 2016.

[30] W. Luo, A. Greenbaum, Y. Zhang, and A. Ozcan, "Synthetic aperture-based on-chip microscopy," *Light: Science and Applications*, vol. 4, no. 3, 2015.

[31] R. Horstmeyer and C. Yang, "A phase space model of Fourier ptychographic microscopy," *Optics Express*, vol. 22, no. 1, p. 338, 2014.

[32] J. S. L. Alan v.Oppenheim, "Importance of Phase in Signals," vol. 69, no. 5, 1981.

[33] B. R. W. Gerchberg and W. O. Saxton, "A Practical Algorithm for the Determination of Phase from Image and Diffraction Plane Pictures," *Optik (Stuttgart)*, vol. 35, no. 2, pp. 237–250, 1972.

[34] S. Marchesini, "A unified evaluation of iterative projection algorithms for phase retrieval," *Review of Scientific Instruments*, vol. 78, no. 1, 2007.

[35] K. Kreutz-Delgado, "The Complex Gradient Operator and the CR-Calculus," 2009.

[36] E. Osherovich, "Numerical methods for phase retrieval," 2012.

[37] L.-H. Yeh, J. Dong, J. Zhong, L. Tian, M. Chen, G. Tang, M. Soltanolkotabi, and L. Waller, "Experimental robustness of Fourier Ptychography phase retrieval algorithms," *PloS one*, vol. 23, p. 33214, dec 2015.

[38] J. Frédéric Bonnans, J. Charles Gilbert, C. Lemaréchal, and C. A. Sagastizábal, "Numerical optimization: Theoretical and practical aspects," *Numerical Optimization: Theoretical and Practical Aspects*, pp. 1–494, 2006.

[39] X. Ou, G. Zheng, and C. Yang, "Embedded pupil function recovery for Fourier ptychographic microscopy: erratum," *Optics Express*, vol. 23, no. 26, p. 33027, 2015.

[40] L. Tian, X. Li, K. Ramchandran, and L. Waller, "Multiplexed coded illumination for Fourier Ptychography with an LED array microscope," *Biomedical Optics Express*, vol. 5, no. 7, p. 2376, 2014.

[41] S. Dong, Z. Bian, R. Shiradkar, and G. Zheng, "Sparsely sampled Fourier ptychography," *Optics Express*, vol. 22, no. 5, p. 5455, 2014.

[42] J. Sun, Q. Chen, Y. Zhang, and C. Zuo, "Efficient positional misalignment correction method for Fourier ptychographic microscopy," *Biomedical Optics Express*, vol. 7, no. 4, p. 1336, 2016.

[43] R. Eckert, Z. F. Phillips, and L. Waller, "Efficient illumination angle self-calibration in Fourier ptychography," apr 2018.

[44] A. Pan, Y. Zhang, T. Zhao, Z. Wang, D. Dan, M. Lei, and B. Yao, "System calibration method for Fourier ptychographic microscopy," *Journal of Biomedical Optics*, vol. 22, p. 1, sep 2017.

[45] P. Song, S. Jiang, H. Zhang, X. Huang, Y. Zhang, and G. Zheng, "Full-field Fourier ptychography (FFP): Spatially varying pupil modeling and its application for rapid field-dependent aberration metrology," *APL Photonics*, vol. 4, no. 5, 2019.

[46] S. Dong, R. Shiradkar, P. Nanda, and G. Zheng, "Spectral multiplexing and coherent-state decomposition in Fourier ptychographic imaging," *Biomedical Optics Express*, vol. 5, no. 6, p. 1757, 2014.

[47] X. Chen, Y. Zhu, M. Sun, D. Li, Q. Mu, and L. Xuan, "Apodized coherent transfer function constraint for partially coherent Fourier ptychographic microscopy," *Optics Express*, vol. 27, no. 10, p. 14099, 2019.

[48] J. R. Fienup, "Invariant error metrics for image reconstruction," *Applied Optics*, vol. 36, no. 32, p. 8352, 1997.

[49] P. E. Debevec and J. Malik, "Recovering high dynamic range radiance maps from photographs," in *Proceedings of the 24th annual conference on Computer graphics and interactive techniques - SIGGRAPH '97*, pp. 369–378, 1997.

[50] S. Yang and H. Takajo, "Quantization error reduction in the measurement of fourier intensity for phase retrieval," *Japanese Journal of Applied Physics, Part 1: Regular Papers and Short Notes and Review Papers*, vol. 43, no. 8 B, pp. 5747–5751, 2004.

[51] Z. F. Phillips, M. V. D'Ambrosio, L. Tian, J. J. Rulison, H. S. Patel, N. Sadras, A. V. Gande, N. A. Switz, D. A. Fletcher, and L. Waller, "Multi-contrast imaging and digital refocusing on a mobile microscope with a domed LED array," *PLoS ONE*, vol. 10, no. 5, pp. 1–13, 2015.

[52] J. W. Goodman, "Introduction to Fourier Optics McGraw-Hill Series in Electrical and Computer Engineering," *Quantum and Semiclassical Optics Journal of the European Optical Society Part B*, vol. 8, no. 5, p. 491, 1996.

[53] D. J. Brady, *Optical Imaging and Spectroscopy*. Hoboken, NJ, USA: John Wiley & Sons, Inc., mar 2008.

[54] M. Born, E. Wolf, A. B. Bhatia, P. C. Clemmow, D. Gabor, A. R. Stokes, A. M. Taylor, P. A. Wayman, and W. L. Wilcock, *Principles of Optics*. 1999.

[55] E. Wolf, "New theory of partial coherence in the space-frequency domain Part I: Steady-state fields and higher-order correlations," *Journal of the Optical Society of America A*, vol. 3, no. 1, p. 76, 1986.

[56] P. Thibault and M. Guizar-Sicairos, "Maximum-likelihood refinement for coherent diffractive imaging," *New Journal of Physics*, vol. 14, 2012.

[57] Y. Zhang, A. A. Pan, M. Lei, and B. Yao, "Data preprocessing methods for robust Fourier ptychographic microscopy," *Optical Engineering*, vol. 56, pp. 2–8, dec 2017.

[58] T. Aidukas, R. Eckert, A. R. Harvey, L. Waller, and P. C. Konda, "Low-cost, sub-micron resolution, wide-field computational microscopy using opensource hardware," *Scientific Reports*, vol. 9, no. 1, pp. 1–12, 2019.